

# Passive and Deterministic Droplet Microfluidics for Single Object Encapsulation and Pairing

Présentée le 1<sup>er</sup> février 2023

Faculté des sciences et techniques de l'ingénieur  
Laboratoire de microsystemes 4  
Programme doctoral en microsystemes et microélectronique

pour l'obtention du grade de Docteur ès Sciences

par

## Jiande ZHOU

Acceptée sur proposition du jury

Prof. M. Gijs, président du jury  
Prof. Ph. Renaud, Dr A. Bertsch, directeurs de thèse  
Prof. A. deMello, rapporteur  
Prof. C. Baroud, rapporteur  
Prof. B. Deplancke, rapporteur



# Acknowledgements

Along this amazing PhD journey, there are many people I would like to thank, without whom this journey would not be possible.

I first would like to thank my supervisor Prof. Philippe Renaud. When I had a passion for droplet microfluidics but had no experience, he trusted me and gave me the opportunity to pursue this topic. The freedom as well as the timely and insightful advice he later gave me has fueled the project as well as my personal development, not to mention his passion for creativity and scientific understanding have influenced me a lot that is a life-long asset. I would also like to give a big thanks to Dr. Arnaud Bertsch, my second supervisor, who is always there for giving me advice on different aspects of the work, including experiments, analysis, writing, and for many plans and decisions. Like Philippe, he is knowledgeable and is always willing to help. From both of them, I have learned how to write good scientific documents, starting by making figures that tell the story. Arnaud has also done incredible reviewing work on this thesis and other papers. I would also like to express my gratitude to my jury members Prof. Bart Deplancke, Prof. Andrew deMello, and Prof. Charles Baroud, for their time visiting EPFL, and the very fruitful discussion we had. I enjoyed very much the interactions and am very grateful for this opportunity. I also thank president Prof. Martinus Gijs for his effort in the administration part and the organization and chairing of the thesis defense. I would also like to thank the secretary of EDMI doctorate program, Lucie Auberson, and the secretary of our lab (LMIS4) Christine Vuichoud, who are always there guiding me through the Ph.D. journey for every administration step, from candidacy exams, annual reports, to summer school organization and the final thesis defense; I particularly enjoyed the mindful discussions with Christine regarding different things in life.

Next, I would like to thank Prof. François Gallaire and other collaborators including Yves-Marie Ducimetière, Ludovic Keiser, and Daniel Migliozi. I have learned so much from them who come from physical and theoretical backgrounds and gave me a different view on our projects and helped me develop a more solid understanding of the phenomenon we are using. I'd like to thank Yueyun Zhang, a PhD student from Prof. Brisken Group with whom we collaborated on a drug discovery project, where I have mostly acquired biological understanding. It was also a pleasure to work with the people from the startup company Parithera, with the CEO Antoine Herzog, CTO Weida Chen, and the intern Vivien. We had spent a good amount of joyful time (Chinese restaurants, mountaineering etc.) together, and their discussion and

## Acknowledgements

---

views on entrepreneurship have opened a new window for me. I will never be able to thank enough the center of Microtechnology (CMi), they introduced me to the cleanroom working environment and microfabrication practices and nothing in this thesis would have been possible without the amazing cleanroom facilities and staffs from CMi at EPFL. I thank all the staff and in particular Cyrille Hibert, Joffrey Pernollet, Julien Dorsaz, Gatera Kumuntu, and Patrick Madliger. I would like to thank the opportunity of working with the technology transfer office of EPFL (TTO), in particular with Alberto Di Consiglio, and with the Patent Attorney/European representative Dr. Klaus-Dieter Banse, from whom I have learnt a lot about patent drafting, intellectual property, and technical writing, which I really enjoyed. I am also grateful for being able to work with Till Ryser, Julie Probst (ETH) and Julia Nette (ETH) for organizing the EPFL-ETH summer school together, I have learnt a lot from them for the organizational skills.

I would like to thank all the LMIS4 team members. A big thanks to Margaux Duchamp who was a senior Ph.D. student in the lab when I started my thesis and who gave me a handful of useful advice for starting the projects. I am also very grateful for the help that the Ph.D. students from the same period as me, Nicolas Maïno, Joan Teixidor, and Clémentine Lipp, and visiting Ph.D. student Mohammadmatin Behzadi for their help, friendship, accompanies, and support along the Ph.D. journey. Although we have very different projects, Nicolas, Joan, Matin, and Clémentine were always ready to help and contributed to my project in their own way; I also learned a lot from them. I am very happy to have shared the office with first Fatemeh Navaee, then Daniel Migliozzi and Evgenii Glushkov, for the very nice discussions throughout the day. I also want to thank the postdoc (also the artist) in the lab, Nadya Ostromohov (and her husband Baruch) for the support in work as well as life; And former postdoc Miguel Solsona and former lab member Sebastian Jiguët, for enjoying different sports together. I would also like to thank the colleagues from the neighboring labs LMIS1 and LIMS2, with whom we had shared interesting discussions in the corridor, nice outings, teaching duties, etc. I have also benefited/learned from people that stayed in the lab during the first period of my thesis, including former scientist Harald van Lintel with whom I had a lot of fruitful discussions, former Postdoc Jonathan Cottet, Clarisse Vaillier, and former Ph.D. students Benoit Desbiolles, Ludovic Serex; And people from the startups coming out from LMIS4, including the Artiria team, Guillaume Petit-pierre, Marc Boers, and Colin Darbellay, and the Dispencell team, George Muller, David Bonzon, and Luc Aberli.

I would like to give here particular thanks to the students that I have supervised along the thesis journey. Oriane Delafontaine was my first master thesis student who worked on an exploratory project where I acquired some supervision skills; Amaury Wei did two semester projects and one summer internship (two weeks) with me, where we discovered a new phenomenon that later developed into a new technology; A big thanks to his great work and the wonderful moments we spent together for the science and for the sports. Hugo Fluhr did his semester project on the droplet sorting part; Torne Tänzer with his semester project on the physical characterization of the droplet phenomenon; Stefan Ivanovic and Nikhil

Mahtan on the development and characterization of the second T-splitting method; Louis Piotet and Tanguy Roche worked on the In-flow project where they have made systematic characterization and optimization of the system I first developed; Julien Aubert through his master thesis explored different fabrication techniques for the K blocking project where he finally found a nice fabrication strategy to realize a sufficient structure for the technique; Yassir Belguerch and Julie Morel did some nice exploration work for the new ideas that we had for potential new technologies. I am very grateful for having been working with these bright and passionate students, without whom this thesis would not be as comprehensive as it is now.

Finally, I would like to thank the people in my life. My parents who have been always trusting me and supporting me, my younger brother Dezhou Zhou who has been cheering me up in the hard moments, their unconditional love have given me the courage to continue and help me relax from the works. Zhengchao Wang, my ex-boyfriend, who had given me great support and enormous patience and endeavor during the first period of my thesis, I wish you all the best and thank you for your supports; Chuyu Zhou, an old friend since 10 years and a real mathematician, has influenced me with his poet's sentiment and shown me the power of dedication and scientific attitudes; My true friend Achille Jouberton, we have many interests in common (hiking, cycling, swimming, etc.) and we were going through the same life period (PhD in pursuit); our relationship starts as the language learning tandem and lasts for all the supports and too many incredible moments/events we shared/experienced in life, I thank you forever for being there when I was experiencing my down moments in life; Chuen-ru Li and Maxime Holdener, my dearest badminton buddies, have shown me the fighting spirit and an attitude looking for progress in all time! Max is a life role model, who has demonstrated the possibility of excelling in sports (former Olympics cycling candidate), studies (PhD in ETHZ), leadership, and being an open-minded, empathetic human, inspiring me to pursue a better self. Paolo Bergamaschi, a great friend that supports me through the most difficult year (last year) of my PhD, when I was deeply stressed and was suffering from the ski accident that has broken my cross ligament imposing an operation and need for rehabilitation. I also thank my flatmates that have been so nice and considerate along the years, and all the people from Luc Badminton club (especially Luc 6 in the year 2019, Luc 5 in the year 2021), Malley weekend badminton friends, all the Chinese friends, Xiaotong Du, Tao Lin, Xingyu Wu, Shengzhao Lei, Yanfei Zhao, Yihui Zuo, Sailan Shui, etc., with whom I have shared many joyful moments and support with each other. I thank all those people for your help and presence in my life during this PhD period.

*Lausanne, December 31, 2022*

Jiande Zhou



# Abstract

The single-cell study, which dissects cell-cell heterogeneity from bulk populations, is of growing attention and importance in biological studies and clinical practices. At the core of the single-cell analysis is the efficient cell isolation and construction of single-cell assays. Among different platforms, droplet-based microfluidics arises as one of the most popular ones. However, like all other tools, the isolation of single cells into each compartment (i.e., droplet) is confronted with randomness, where the cell occupancy in each compartment is non-deterministic but follows Poisson statistics (Poisson limit). The Poisson limit is currently an inevitable obstacle in droplet microfluidics, hindering a large number of droplet-based single-cell assays.

Attempts have been made to overcome the Poisson limit during single-cell encapsulation into droplets. Active approaches requiring droplet detection, actuation, and synchronization, is complex, expensive, and limited by throughput (label-free). On the other hand, the passive strategy is automatic and simpler, but the current methods lack control and robustness on the single-cell encapsulation outcomes. A passive yet deterministic, simple, and robust approach for single-cell encapsulation is missing. Active or passive, there is no droplet microfluidics platform for label-free and ultra-high throughput single-cell encapsulation, nor for distinguishing droplets containing one cell from droplets with multiple cells. This thesis targets on these issues.

In this thesis, we first looked into details of a new type of droplet instability and studied the corresponding new breakup mechanism analytically, experimentally, and numerically. This part is presented in **Chapter 2**. Chapters 3, 4, and 5 each present a strategy toward passive single-cell deterministic encapsulation. In **Chapter 3**, we used a post-encapsulation secondary breakup-mediated droplet sorting strategy, based on the phenomenon of cell-triggered (droplet) splitting (CTS). The droplet instability from Chapter 2 is the cause of the CTS, which is unique and scalable with a simple geometrical rule. In **Chapter 4**, we developed a post-encapsulation direct droplet sorting strategy, based on the single-cell differentiated droplet trajectory (SCDT). We demonstrated a novel passive mechanism to induce a change of droplet trajectory based on the number of single cells it contains. Empty droplets, single-cell droplets, and multi-cell droplets can be equally separated. In **Chapter 5**, towards the deterministic rigid particle encapsulation, we developed a particle-triggered droplet generation technology (K-blocking), enabled by a novel fabrication strategy. This is a passive on-demand

## Abstract

---

droplet generator. Finally, in **Chapter 6**, we developed a waiting-concept-aided deterministic droplet pairing and merging device (In-flow merging). We demonstrated 100% one-to-one merging for one droplet type using this mechanism, particularly suited for low-input droplet sample requiring high accuracy. **Chapter 7** is dedicated to a summary and discussion of the above technologies towards different application scenarios.

In summary, this thesis contributes to the development of droplet microfluidics in three aspects: 1. we discovered and studied a new droplet breakup instability that is fundamental and might inspire new droplet microfluidics applications; 2. we provided new solutions and strategies for single-cell or particle encapsulation overcoming the Poisson limit, which are useful tools to develop new microfluidics workflows; 3. and finally, we developed a deterministic droplet merger which could improve the construction of multi-cell (bead) droplet assays. We believe that these theoretical and technological achievements will largely facilitate the advancement of droplet microfluidics and in particular its application in single-cell study.

## Keywords

Single cell, Droplet-based microfluidics, Encapsulation, Deterministic, Electrocoalescence, Droplet breakup, Instability

# Résumé

L'étude unicellulaire, qui dissèque l'hétérogénéité des cellules à partir de populations massives, est d'une importance croissante dans les études biologiques et les pratiques cliniques. Au cœur de l'analyse unicellulaire se trouve l'isolement efficace des cellules et la construction d'essais unicellulaires. Parmi les différentes plateformes, la microfluidique en gouttelettes est l'une des plus populaires, en raison de sa sensibilité, de son faible coût, de son débit élevé et de son contrôle flexible des micro-compartiments miniaturisés contenant des cellules uniques. Cependant, comme tous les autres outils, l'isolement de cellules uniques dans chaque compartiment (c'est-à-dire dans une gouttelette) est confronté au caractère aléatoire, l'occupation des cellules dans chaque compartiment n'étant pas déterministe mais suivant une statistique de Poisson. Selon cette dernière, seule une petite partie de la population de gouttelettes présente une charge unicellulaire, et de grandes quantités de gouttelettes vides sont inévitables pour diminuer le pourcentage de charge multicellulaire. Cela pose un problème pour de nombreuses applications, en particulier pour l'étude multimodale des cellules uniques où, dans de nombreux scénarios, deux ou plusieurs cellules/particules distinctes sont nécessaires dans chaque compartiment. Ce problème est bien connu sous le nom de limite de Poisson. Ceci est actuellement d'un obstacle inévitable de la microfluidique en gouttelettes, qui entrave l'acquisition et l'application contrôlées de divers essais sur des cellules uniques.

Des tentatives ont été faites pour surmonter la limite de Poisson lors de l'encapsulation de cellules uniques dans des gouttelettes. D'une part, les approches actives, qui nécessitent la détection, l'activation et la synchronisation des gouttelettes, sont complexes, coûteuses et limitées par le débit (sans marqueur). D'autre part, la stratégie passive est automatique et plus simple, mais les méthodes actuelles manquent de contrôle et de robustesse sur les résultats de l'encapsulation unicellulaire. Il manque donc une approche passive, déterministe, simple et robuste pour l'encapsulation des cellules individuelles. Qu'elle soit active ou passive, il n'existe pas de plateforme microfluidique en gouttelettes pour l'encapsulation unicellulaire sans marquage et à très haut débit, ni pour distinguer les gouttelettes contenant une seule cellule de celles contenant plusieurs cellules. Cette thèse vise à répondre à ces questions.

Dans cette thèse, nous avons d'abord examiné les détails d'un nouveau type d'instabilité des gouttelettes provenant d'une structure communément utilisée et étudié le nouveau mécanisme de rupture correspondant, des points de vue analytiques, expérimentaux et numériques. Cette partie est présentée au chapitre 2, qui sert de base théorique aux technologies que nous

avons développées au chapitre 3. Quant aux chapitres 3 à 5, ils présentent chacun une stratégie (différente) d'encapsulation déterministe passive et robuste d'une seule cellule. Dans le chapitre 3, nous avons utilisé une stratégie de tri des gouttelettes après encapsulation, basée sur le phénomène de séparation (des gouttelettes) déclenché par les cellules (CTS). La nouvelle instabilité des gouttelettes du chapitre 2 est à l'origine du CTS, qui est unique et adaptable suivant une seule règle géométrique. En jouant sur la physique, nous avons présenté deux géométries pour le CTS, adaptées respectivement à la création de petites gouttelettes à ultra-haut débit (sans marqueur) et à la création de grosses gouttelettes. Dans le chapitre 4, nous avons développé une stratégie de tri direct des gouttelettes après encapsulation, basée sur la trajectoire des gouttelettes différenciées par cellule unique (SCDT). Nous avons démontré un mécanisme passif et novateur pour induire un changement de trajectoire des gouttelettes en fonction du nombre de cellules uniques qu'elles contiennent. Les gouttelettes vides, les gouttelettes monocellulaires et les gouttelettes multicellulaires peuvent être séparées de manière égale. Il s'agit de la première méthode de tri des gouttelettes basée sur le contenu avec une résolution unicellulaire, mais des développements supplémentaires sont nécessaires. Alors que le CTS et le SCDT des chapitres 3 et 4 s'appliquent aux cellules uniques et aux particules déformables, nous avons développé une technologie de génération de gouttelettes déclenchée par des particules (blocage K) dans le chapitre 5, en vue de l'encapsulation déterministe de particules rigides (moins déformables). Deux modes de fonctionnement ont été présentés, rendus possibles par une nouvelle technique de fabrication. Il s'agit d'un générateur de gouttelettes à la demande qui fonctionne d'une manière passive simple, évitant l'encapsulation aléatoire. Enfin, pour la fusion contrôlable des gouttelettes avec un contenu déterministe obtenu à partir des techniques ci-dessus, nous avons développé une technologie d'appariement et de fusion déterministe des gouttelettes au chapitre 6, assistée par un concept d'attente (In-flow merging). Nous avons démontré une fusion une-à-une de 100 % pour un type de gouttelettes en utilisant ce mécanisme. Il permet la construction précise d'essais monocellulaires multi-objets, particulièrement adaptés à la manipulation d'échantillons de gouttelettes rares. Le chapitre 7 propose un résumé et une discussion des technologies ci-dessus en vue de différents scénarios d'application.

En résumé, cette thèse contribue au développement des technologies microfluidiques en gouttelettes sous trois aspects : nous avons découvert et étudié une nouvelle instabilité de rupture des gouttelettes qui est fondamentale et qui pourrait inspirer le développement d'autres technologies microfluidiques de gouttelettes; nous avons fourni de nouvelles solutions et de nouvelles stratégies pour l'encapsulation de cellules ou de particules uniques en surmontant la limite de Poisson, qui sont des outils utiles pour développer de nouveaux flux de travail microfluidiques; et enfin nous avons développé une fusion déterministe de gouttelettes qui pourrait améliorer la construction d'essais de gouttelettes multi-cellules (billes). Nous pensons que ce développement technologique facilitera également de manière significative l'avancement de l'étude des cellules uniques.

**Mots-clés**

Cellule unique, microfluidique à base de gouttelettes, encapsulation, déterministe, électrocoalescence, rupture de gouttelettes, instabilité.



# Contents

<b>Acknowledgements</b>	<b>i</b>
<b>Abstract (English/Français)</b>	<b>v</b>
<b>1 Introduction</b>	<b>1</b>
1.1 Background	1
1.1.1 Single cell study	1
1.1.2 Microfluidics Single Cell Isolation and pairing	3
1.1.3 Droplet microfluidics for single-cell study	6
1.1.4 The Poisson limit	8
1.1.5 State of the art to overcome the Poisson limit	10
1.2 Research strategy	12
1.2.1 Scope of the thesis	12
1.2.2 Structure of the thesis	14
<b>2 Mechanism of a new droplet breakup regime in T-junctions</b>	<b>15</b>
2.1 Introduction	15
2.2 Results	16
2.2.1 Discovery of the novel breakup phenomenon	16
2.2.2 Geometric conditions required for the lateral breakup	17
2.2.3 Modeling of the dynamics of the lateral breakup for lower Ca	19
2.2.4 A central breakup recovered at higher Ca	23
2.3 Methods	26
2.3.1 Device fabrication	26
2.3.2 Experiments	27
2.4 Discussion	28
2.4.1 Limitations of the current numerical model	28
2.4.2 Deep channel effect	28
2.4.3 The real cause for the transition	29
2.5 Conclusion and outlook	31
<b>3 Deterministic single cell encapsulation based on Cell Triggered Splitting (CTS)</b>	<b>33</b>
3.1 Introduction	33
3.2 The general strategy	33

## Contents

---

3.3	Methods . . . . .	35
3.3.1	Chip fabrication . . . . .	35
3.3.2	Chip design and scaling (CTS-1) . . . . .	35
3.3.3	Single cell encapsulation . . . . .	36
3.3.4	Single bead encapsulation . . . . .	36
3.3.5	Cell viability test . . . . .	36
3.4	Lateral breakup/Central breakup competition . . . . .	36
3.4.1	Design and working principle . . . . .	37
3.4.2	Results . . . . .	37
3.4.3	Discussion . . . . .	44
3.5	Step breakup/Central breakup competition . . . . .	44
3.5.1	Design and working principle . . . . .	44
3.5.2	Results . . . . .	46
3.5.3	Discussion . . . . .	51
3.6	Discussion . . . . .	51
3.6.1	Other object-triggered effect . . . . .	52
3.6.2	Cell triggered splitting without T junction . . . . .	52
3.6.3	CTS as a real solution to Poisson Limit . . . . .	53
3.7	Conclusion and outlook . . . . .	54
<b>4</b>	<b>Single cell encapsulation based on Single Cell Differentiated Trajectory (SCDT)</b>	<b>55</b>
4.1	Introduction . . . . .	55
4.2	Working Principle . . . . .	56
4.3	Results . . . . .	57
4.3.1	Distinguishing singlets, doublets, and multiplets . . . . .	57
4.3.2	Influence of droplet size . . . . .	58
4.3.3	Proof of concept . . . . .	60
4.3.4	A generalized geometry . . . . .	61
4.4	Discussion . . . . .	64
4.4.1	The narrow section and the single cell sorting resolution . . . . .	64
4.4.2	Other potential mechanisms . . . . .	65
4.4.3	A versatile droplet/particle sorter based on the asymmetric wall effect . . . . .	65
4.5	Conclusion and outlook . . . . .	67
<b>5</b>	<b>Single object encapsulation based on passive blocking</b>	<b>69</b>
5.1	Introduction . . . . .	69
5.2	Working Principle . . . . .	69
5.3	Fabrication development . . . . .	70
5.4	Result . . . . .	73
5.4.1	Unsuccessful events with 2D and 2.5D devices . . . . .	73
5.4.2	Proof of concept with “full-blocking” mode . . . . .	74
5.4.3	An interesting working condition with “partial-blocking” mode . . . . .	75
5.5	Discussion . . . . .	77

5.5.1 Design rule for the full-blocking mode . . . . .	77
5.5.2 Potentially more suited for rigid bead encapsulation . . . . .	80
5.6 Conclusion and Outlook . . . . .	81
<b>6 Deterministic droplet pairing and merging</b>	<b>83</b>
6.1 Introduction . . . . .	83
6.2 Working principle . . . . .	84
6.3 Result and Discussion . . . . .	85
6.3.1 Fluid elements . . . . .	86
6.3.2 The electrocoalescence theory . . . . .	87
6.3.3 The merging performance . . . . .	88
6.4 Fabrication and Experimental . . . . .	91
6.4.1 PDMS chip fabrication . . . . .	91
6.4.2 Electrode fabrication . . . . .	91
6.4.3 Experimental control . . . . .	92
6.5 Discussion . . . . .	92
6.5.1 The optimal performance and current limitation . . . . .	92
6.5.2 Comparison with other merging techniques . . . . .	93
6.6 Conclusion and outlook . . . . .	94
<b>7 Summary and Conclusion</b>	<b>95</b>
7.1 Summary . . . . .	95
7.1.1 Summary of results . . . . .	95
7.1.2 Deterministic single object encapsulation . . . . .	96
7.2 Conclusion and Outlook . . . . .	98
<b>A Appendix</b>	<b>101</b>
A.1 Mathematical modeling of the inflation of the lateral pockets at low Ca . . . . .	101
A.1.1 Numerical simulations . . . . .	104
A.1.2 A scaling argument for onset of central breakup . . . . .	105
A.2 Nanoscribe 2.5D device Process flow . . . . .	106
A.3 Theoretical development of the bead releasing condition . . . . .	106
A.4 Design optimization for In-flow . . . . .	112
A.4.1 Optimization of the fluidic elements . . . . .	112
A.4.2 Optimization of electrocoalescence configuration . . . . .	113
<b>Bibliography</b>	<b>117</b>



# 1 Introduction

## 1.1 Background

### 1.1.1 Single cell study

As the basic structural and functional unit of all life forms, the cell has been a major research object for scientists. Indeed, the studies of cells and how they function, communicate, evolve, etc., not only answer the fundamental questions in life science but also provide new insights/means for fighting diseases, curing injuries, prognostics, etc. Historically, due to the technological limit, the studies of cells have been conducted with bulk samples. The obtained readout is an averaged result over the total population, therefore concealing the heterogeneity that exists in individual cells.

Recently, with the development of micro-technologies that function at a scale comparable to single-cell size, the study of individual cells becomes possible. Over the years, many studies have demonstrated the benefits of dissecting cell-cell variations. For example, scientists have used it to: identify sub-populations of cells, discover novel cell types, understand the role/functionalities of each cell (type), construct cell lineage, predict the cell fates[1], detect individual cellular response to external stimulus, etc. In fact, the study of single cells can be conducted at all levels of the central dogma of molecular biology (Fig.1.1) [2, 3]. This translates to a broad range of cellular parameters spanning from *inside the cells* (e.g., chromatin accessibility, transcriptomics, genomics, intracellular proteins), *on the cell membrane* (e.g., surface proteins, T cell receptors), to *outside the cells* (e.g., change of the microenvironment, cytokines, antibody, other secretions). From a pseudo-temporal point of view, the different cellular information can be used to determine the cell lineage (past), the current states (now), and the pseudotemporal trajectory (future)[3]. From the readout point of view, fluorescence signal from biological assays has been the major readout, but with technological advancement, other readouts are more and more available, including imaging data (phenotype), mechanical properties data, chemical spectrum data, different sequencing data, etc. A typical example is the single-cell RNA sequencing technique (ScRNA seq), which detects, quantifies, and sequences the messenger RNA molecules within individual cells. Currently, it is widely adopted in all research areas

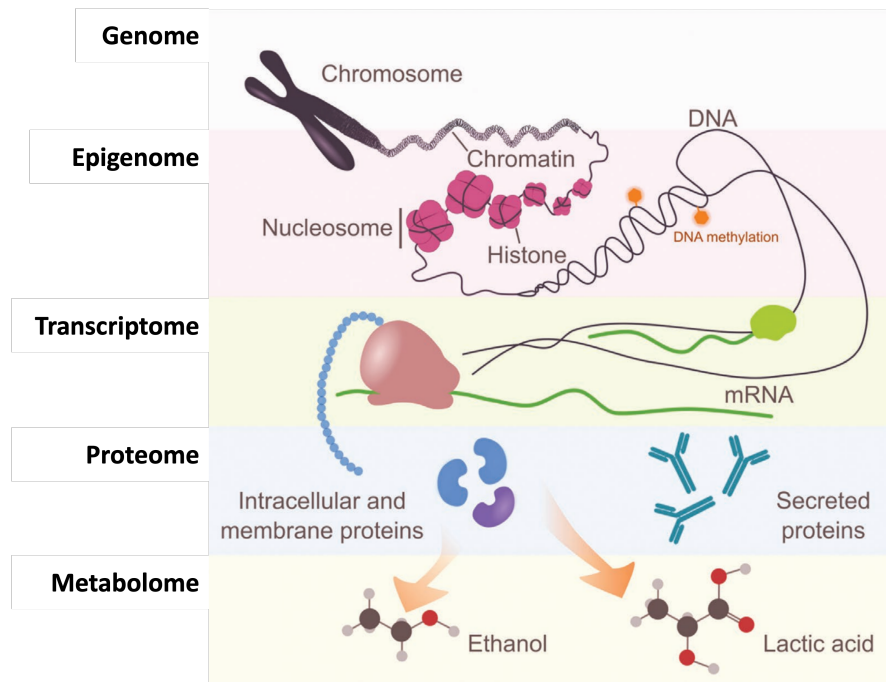


Figure 1.1 – Single cell study can be performed at all levels of the central dogma of molecular biology. Adapted from [2]

with different technological variations[4, 5], contributing greatly to understanding cellular functions and activities.

In addition to unimodal single-cell profiling where each cell is profiled with a single cellular parameter, it is increasingly popular to perform multimodal single-cell profiling to obtain more information for each cell[6, 3]. For example, time information + spatial information + transcriptomics are acquired at the same time via a recently developed non-destructive *in situ* live cell RNA sequencing technique[7]. Surface proteins, transcriptomes, clonotypes, and CRISPR perturbations are detected multiplexedly, revealing a high resolution of information for individual cells in one shot[8]. To realize multimodal single-cell profiling (and for some unimodal profiling), it is generally required to have novel biological assays with more complexity. Often, in addition, to have the single cells and the corresponding reagents in each assay, there is the need to add one or more functional particle(s) paired with each cell of interest for specific processes, like barcoding, antibody binding etc. Such biological assays are currently of growing interest with the emphasis being given to mapping thoroughly each cell status for better information and understanding. There is also the need to compartment one single cell type with exactly one other single cell type in a common space, to study the properties, process, and secretions during specific or non-specific cell-cell interactions.

Currently, given its versatility and importance, single-cell study has been applied to many fields of study, including immunology[9], cancer biology, microbiology, plant biology, embryogenesis, neuroscience, etc. This thesis will contribute to the technological development of

single-cell study.

### 1.1.2 Microfluidics Single Cell Isolation and pairing

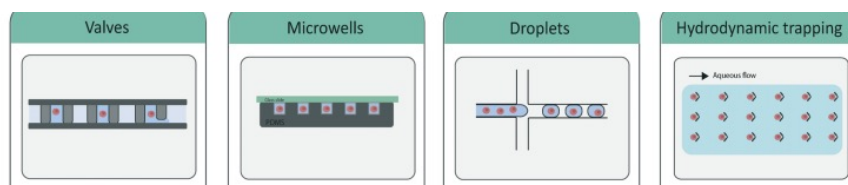
Essential to the single-cell study are the micro-technologies that are capable of single-cell isolation and/or pairing with other particles or cells. It is the prerequisite to perform any single-cell assays and subsequent data analysis. Compared to traditional plate-based biological assays, microfluidics which manipulates fluids at the submillimeter scale, enables the miniaturization of reactions. Thus, through microfluidics single-cell compartmentalization, not only can individual cells be accessed for analysis, but the detection sensitivity, efficiency, and throughput are also significantly improved. The reduced reagent and improved throughput further allow the significant cost reduction per cell analyzed. In this section, we mainly summarize the microfluidics-based single-cell techniques.

Currently, there are four main microfluidics techniques for performing single-cell assays: valves, microwells, droplets, and hydrodynamic trapping[10, 11, 6]. All of them can be used to isolate single cells as well as to pair each cell with another cell of a different type or another single particle. The summary of these techniques can be found in Fig. 1.2.

First introduced by Quake et al. in 2000[12, 13], the valve-based systems use pneumatic multilayer valves to control the fluid flow and to turn micro-channels into micro-chambers as needed for isolating single-cell or single cell pairs. Each valve requires a pressure control layer and a fluid channel layer. Due to the active control over the mechanical valves, the liquid exchange is made straightforward. Through careful design, the chambers (channels) can be multiplexed with computer-aided control to execute complex and fully integrated workflow (no off-chip intermediate steps)[14]. This could benefit applications that require multiple reagent addition and/or washing (e.g., whole genome sequencing[15, 16], gene expression profiling[17, 18]). However, as each valve needs to be controlled and there are many to boost the throughput, the individual manipulation of the numerous chambers requires complex pressure control lines with cascade operation steps. Therefore, the system's design, fabrication, and operation are complex, resulting in relatively low throughput and a high cost. In addition, due to the fairly large control volume, despite the accurate manipulation of the fluid flow, the loading of single cells into each chamber isolated by the valves is still random, ranging from zero to a few cells[19, 13]. In terms of single cell-to-cell or cell-to-bead pairing, without active detection, the process is done randomly[18, 15]. Alternatively, one can use the valve operation to stop both particles in the same chamber with active detection [20].

Microwells confine single cells by flowing the cell suspension over well arrays and letting the cells sediment naturally into each well by gravity. The number of cells loaded in each well generally follows the Poisson statistics. The open structure allows the rapid exchange of reagents, which, however, also causes easy contamination and material loss [21]. Due to the laminar flow profile and the surface tension, the wells can be sealed by flowing an immiscible phase, for example, with perfluorinated oil to seal cell suspension within their wells[22, 21].

## Chapter 1. Introduction



Unit Sample Volume	1.7 -700 nL / chamber	20 pL - 1.0 nL / well	1 fL - 10 nL / droplet	NA
Compartmentalization	Yes	Yes	Yes	No
Multiplexing Capability	High	Medium	Medium	Low
Cell Loading Scheme	Random	Random	Random / Super Poissonian (Bead)	Random / Super Poissonian
Selective Cell Retrieval	Easy	Medium (in open channel)	Easy	Difficult
Throughput	10- 300 chamber /run (Low)	10 <sup>4</sup> -10 <sup>5</sup> wells / run (Medium)	> 10 <sup>3</sup> droplets/ second (High)	10 <sup>2</sup> -10 <sup>3</sup> traps / run (Medium)
Scale-up Capacity	Low	Medium-High	High	Medium
Easy-of-Operation	Difficult	Easy	Medium	Medium
Integration Potential	High	Low	High	Medium
Advantages	Easy fluid exchange (washing); Precise liquid control	Easy to use; Compatible with long term cell culture; Easy fluid exchange (washing)	Rapid mixing; High throughput; Easy sample sorting and retrieval; Little cross contamination	Compatible with long term cell culture; Easy fluid exchange (washing);
Limits	Low throughput, Complex design, fabrication and operation	Sample retrieval difficulty; Does not support integrated workflow	Droplet fragility, not easy fluid exchange (washing)	No compartmentalization; Often requires complex fluid profile for operation; Sample retrieval difficulty;
Commercial platforms	Fluidigm C1, Fluidigm Polaris	BD Rhapsody, Celselect, ICell8, SEED Biosciences	10xGenomics, in-Drop, Nadia, Tapestri	Acroscreen

Figure 1.2 – **Summary of different microfluidic single-cell isolation methods.** Adapted from [2]

Alternatively, the reagent can be added by pre-treating a membrane or glass slide, which is then aligned and bonded with the wells (reversibly or irreversibly). As the laminar flow profile also causes insufficient mixing of reagents inside the microwells, the sealing of the microwell is sometimes mandatory to enhance the mixing with sonication, flipping the chip, etc. [21]. In the case of non-sealing or reversible sealing, the retrieval of sample content is feasible- for example, single cells of interest can be manually withdrawn with a micrometer scale capillary [21]. However, sample retrieval is not straightforward and requires skillful operators with careful manual work. Overall, the microwell method is attractive because of its simplicity, which has enabled high throughput (up to  $8 * 10^5$  wells/ run) and low cost. It is, however, not compatible with complex integrated workflow. Here, the pairing of one cell with another single cell or bead is done by flowing two types of suspension and subsequent random co-sedimentation [23].

The third approach uses aqueous droplets suspended in an immiscible oil phase as micro-reaction chambers to analyze every single cell. These micro-reactors ranging from  $1 fL$  to  $10 nL$  can be generated at high throughput, low cost, reproducible size, and intrinsically rapid internal mixing under relatively simple operation. The properties of the oil, i.e., the low solubility of organic molecules [24] and high solubility of oxygen [25] permits good confinement of the biological components (minimizing the cross-contamination and sample loss) while allowing for cell incubation. Such good compartmentalization can raise difficulties for liquid exchange and long-term single-cell incubation under a relatively small volume. Nonetheless, droplet-based microfluidics have a high degree of operational flexibility, enabling re-loading, merging, splitting, detection, sensing, trapping, and sorting operations [2, 26]. Therefore, after droplet microchambers are formed, there are means to increase the volume further/change the droplet content, which can be integrated into a more complex and automated workflow. This benefit also allows efficient retrieval of samples of interest. Due to the simplicity of droplet generation and the small volume of each droplet, it has the highest throughput compared to other methods. In the case of cell-cell or cell-bead droplet assays, the internal mixing of droplet microfluidics is a natural advance to enhance the mechanical contact between the cells and facilitate the capture of cell components on the functional beads. Like the previous methods, loading single objects or single object pairs into each droplet is a random process without active control.

While the above approaches introduce a physical barrier to confine single cells, the last method of microfluidics cell trapping does not establish compartmentalization for each cell but rather separates single cells via mechanical microfluidics trap arrays in a common bulk solution [19]. Hydrodynamic trapping of single cells is mainly used when two distinct types of single cells must be paired one-to-one to study cell-cell interaction. With careful trap geometry design (with the trap size difference, step difference, etc.) and sequential operations, the cell-cell capture efficiency can be highly improved compared to the random methods [27, 28, 29]. While the loading of cell pairs is less random, more sophisticated chip design and flow profiles are required. Changing the reagents/microenvironments for these immobilized cell pairs is

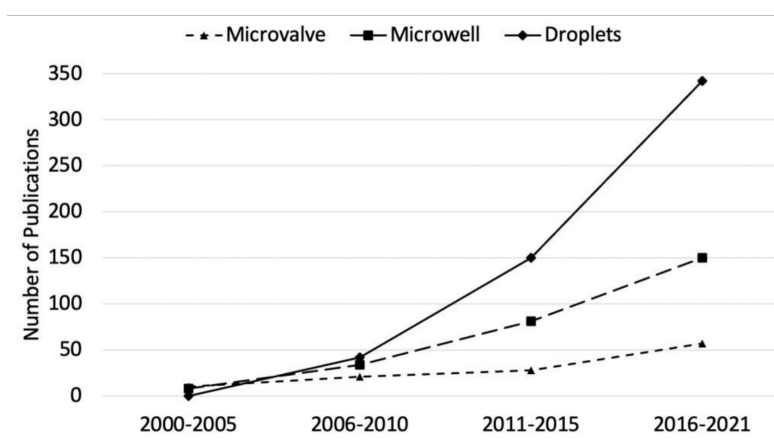


Figure 1.3 – The number of publications in different years for single-cell studies using the valve, microwell, and droplet studies[2].

convenient. On the other hand, there is no compartment for each cell pair, limiting the ranges of feasible analysis and sample retrieval. Currently, there are also other trapping methods using no physical contact, like optical methods, dielectrophoresis (DEP)[30], acoustic waves [31], etc. These methods usually have lower throughput compared to hydrodynamic trapping [6], but will have larger flexibility and higher precision for individual cell manipulations.

In some cases, two or more approaches can be combined. For example, droplet can be combined with valves[20], microwell, or hydrodynamic trapping[32, 33, 34], to take advantages of both approaches. If we compare the technologies we have introduced, the major drawback of the valve-based technique is its complexity requiring skillful operators and the associated low throughput. The microwell approach has simplicity and relatively high throughput but is vulnerable to sample cross-contamination and loss and is limited in incorporating more advanced workflow. The trapping-based approach's main disadvantage is the lack of proper confinement for a single cell and its components, which limits the more in-depth analysis beyond the microscope interrogation and the sample retrieval. Droplet-based microfluidics probably gives the best compromise between complexity, functionality, throughput, and integration potential. As a result, it has gained the most rapid growth in recent years[11] among the single-cell isolation techniques enabling proper compartmentalization (Fig.1.3). The current thesis work is focused on droplet-based microfluidics as a tool for single-cell analysis.

### 1.1.3 Droplet microfluidics for single-cell study

In this section, we look into droplet-based microfluidics. Due to its advantages, droplet-based microfluidics has been widely used beyond the field of single-cell study, for example, in other biochemical research (without cells) and in materials fabrication used as micro-reactors [35, 36], material templates [37, 38, 39], , digital counters [40, 41, 42], etc. We decided that this is beyond the scope of discussion here. The fundamental aspects of droplet-based microfluidics,

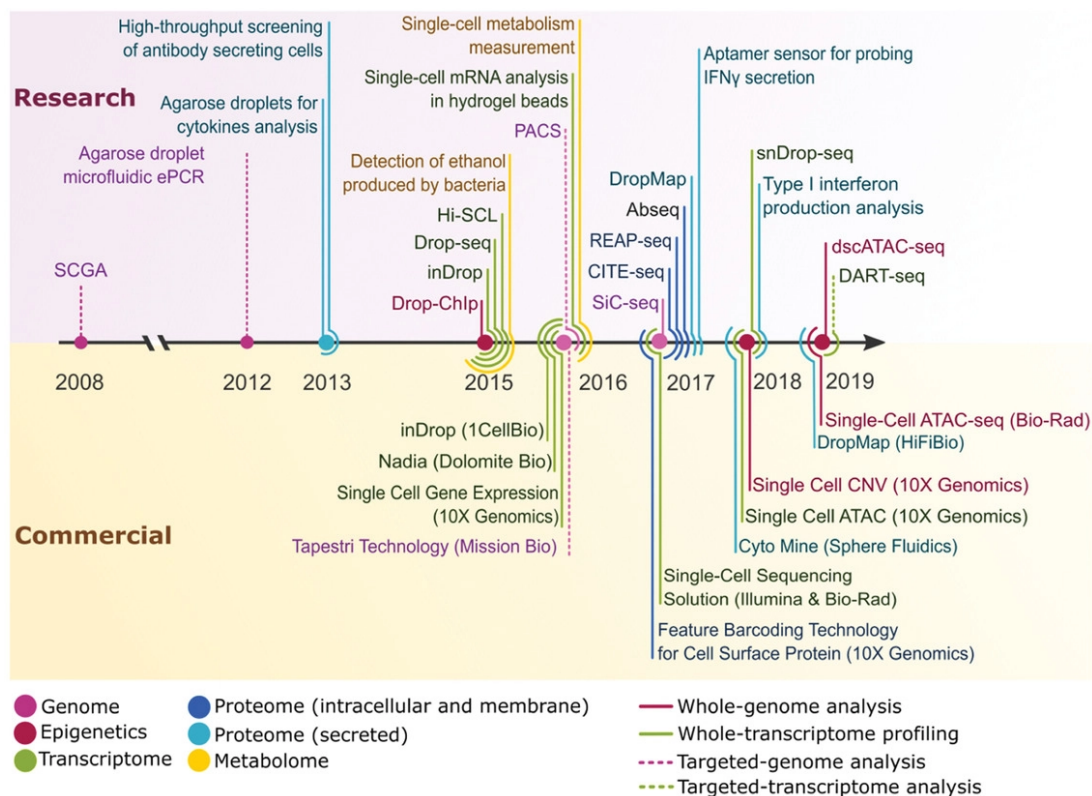


Figure 1.4 – **Different single cell droplet-based techniques developed in chronological order.** Adapted from [2]

including chip fabrication, droplet generations, droplet operations, and different applications within or outside the single-cell study domain, have been thoroughly summarized in the review paper of Shang et.al. [26], and will not be further introduced here.

As of today, droplet-based microfluidics has been used to develop many single-cell-related biotechnologies. As a versatile single-cell platform, research around the central dogma of molecular biology can be all covered in droplet-based techniques. A summary of the recent year's development of these techniques is shown in Fig.1.4, which includes single-cell profiling from all levels.

### Droplet Sorting

Compared to the valves, microwells, and trapping techniques, a major advantage of droplet microfluidics as a single-cell platform is its sorting capacity, enabled by the well-compartmentalized and free-flowing droplets. A droplet will only be collected if itself or its encapsulated cells fulfill certain requirements. It opens the door for high throughput screening, sample enrichment, etc. Both active and passive droplet sorting methods can be used. Active sorting uses real-time detection for decision-making, synchronized with prompt actuation for sorting,

i.e., deviating the droplet trajectory from the default trajectory so that they end up in a different collection outlet. The sorting triggering criterion can be based on image processing, fluorescence intensity, different spectrum information, etc., where the application usually defines the event of interest and the detection methods. The actuation method, on the other hand, can be more flexible and interchangeable. Different mechanisms exist to achieve a fast and reliable actuation response for active sorting, on which Xi. et. al. has given a thorough summary in their review paper[43]. The most common one is with dielectrophoresis (DEP), where a nonuniform alternating current (AC) electric field polarizes the droplets and exerts a displacement force to deviate the droplet trajectory[44]. Other actuation mechanisms include 1. Acoustophoresis, where the droplet motion is changed with the change of sound pressure [45], the advantage here is the biosecurity; 2. Magnetic sorting, where droplets are deviated by an electromagnet or permanent magnet, the disadvantages are the need for a ferrofluid as the dispersed or continuous phase, and the low response speed with a typical switching frequency at the scale of a few Hz[46]; 3. Pneumatic control, where the deformation of the channel modifies the hydrodynamic pressure and changes the droplet motion. To perform an active sorting, a fully integrated system including detection, analysis, actuation, and synchronization is required. It is more expensive and more demanding than a passive method, and its use is usually related to more complex applications.

In passive droplet sorting, there is no need for detection or decision-making, the actuation is based on the differentiation of one or multiple natural properties of the droplets, which automatically triggers a trajectory difference based on different working principles, resulting in the sorting. Passive methods are, therefore, simpler and more cost-effective. Currently, the most studied property for droplet sorting is droplet size. Based on the size difference of the droplets, there are several mechanisms to separate the droplet trajectories effectively, including Deterministic Lateral Displacement (DLD)[47], shear migration[48], microfiltration, pinched flow fractionation (PFF)[49]. In addition, there are also passive sorting methods developed based on the difference in properties like viscosity/rigidity[50, 51, 52], surface tension [53], density difference[54].

Sorting is an important topic in this thesis. On the one hand, we need to use some of the passive sorting approaches to complete our strategies (Chapter 3,6). On the other hand, we also developed our own sorting technique (Chapter 4). They will be further discussed in the corresponding chapters.

### 1.1.4 The Poisson limit

As discussed previously, the loading of single cells or single cell pairs into each compartment is random in the already mentioned techniques. The statistic that describes the probability of different numbers of objects being loaded in each compartment is the Poisson distribution. It tells that a large number of the compartments will have unwanted cell occupancy (i.e., empty, or more than one cell), commonly referred to as the Poisson limit. For all single-cell isolation

techniques, the Poisson limit is a common issue.

In terms of droplet-based microfluidics, the Poisson limit comes from the mismatch of random cell distribution in the medium versus the regular droplet generation frequency. According to the Poisson distribution, provided that the single cells are distributed independently of each other (i.e., homogeneous distribution), the probability ( $P(X = x)$ ) of having  $x$  cells in each droplet is given by  $P(X = x) = e^{-\lambda} [\lambda^x / x!]$ , where  $\lambda$  is the calculated average number of cells per droplet volume, which is dependent on the droplet volume and the initial cell concentration in the bulk aqueous solution. As a request for unambiguous single-cell analysis, multiple-cell loading (multiplets) needs to be avoided. It is common to apply highly diluted cell suspension to lower the ratios of multiplets in the assays, which however inevitably creates a lot of empty droplets, wasting the reagent and undermining the throughput.

As the single-cell study is shifting towards multimodal studies, the need to construct multi-cellular and multi-cell/bead assays is becoming increasingly important. This requires each droplet to contain a defined number and type of objects, for example, exactly one cell and exactly one functionalized particle, or one type A cell and one type B cell. In these cases, the Poisson limit is more acute. For example, from the single Poisson distribution, we can derive eq.1.1 which gives the probability of having  $k_1$  cells of type A and  $k_2$  cells of type B in one droplet, with  $\lambda_1$  and  $\lambda_2$  being the average number of cells of type A and B per original droplet. Thus, the probability of having exactly one A cell and one B cell in one droplet is given by eq.1.2, and the ratio of cells that are wasted (i.e., not in the correct droplets,  $WC_{ratio}$ ) can be formulated as eq.1.3. Fig.1.5 shows these two ratios under random encapsulation by varying  $\lambda$  for each type of cell. Not surprisingly, even under the best droplet ratio scenario, there is less than 14 percent of droplets with the right combination of cells, at the price of sacrificing 86 % of the total cells that are introduced into the system. This is not acceptable in many real-world scenarios, for example, when valuable clinical samples are utilized and small tolerance on false pairing is allowed. For three or more distinct objects to be paired in one droplet, the statistic is significantly worsened. Overcoming the Poisson limit is urgent for current and future single-cell studies and applications.

$$P(X_1 = k_1, X_2 = k_2) = \frac{e^{-\lambda_1} \lambda_1^{k_1}}{k_1!} \cdot \frac{e^{-\lambda_2} \lambda_2^{k_2}}{k_2!} \quad (1.1)$$

$$P(X_1 = 1, X_2 = 1) = e^{-\lambda_1} \lambda_1 \times e^{-\lambda_2} \lambda_2 \quad (1.2)$$

$$WC_{ratio} = 1 - \frac{2P(X_1 = 1, X_2 = 1)}{\lambda_1 + \lambda_2} \quad (1.3)$$

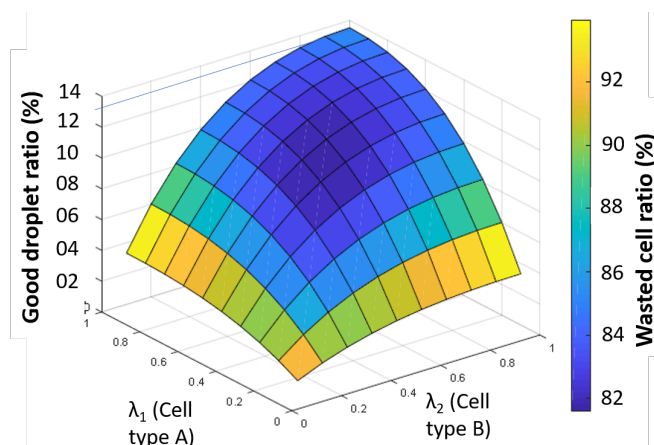


Figure 1.5 – Good droplets ratio and wasted cell ratio under random co-encapsulation of single cell/particle, with different cell concentrations.

### 1.1.5 State of the art to overcome the Poisson limit

Currently, there are both *active* and *passive* approaches to overcome the Poisson limit during single-cell encapsulation into droplets. The active method means that external control is needed to initiate certain actions to complete one event upon detection of another event. On the contrary, the passive method requires no active components and performs the tasks automatically without any detection, decision-making, or actuation; therefore represents the simplest and most cost-effective way of operation. Unfortunately, for single cells, due to their fragility, small dimension, and adherent property, the Poisson limit cannot be overcome easily with a passive method. It is generally considered difficult, if not impossible, to have a robust passive solution for deterministic single-cell encapsulation.

In the following, we summarize the current attempts to overcome the Poisson limit, i.e., to obtain only the single-cell droplets. We categorized these technologies into four main strategies, including “Post encapsulation droplet sorting”, “Cell ordering”, “Droplet on-demand generation”, and “Trap-assisted encapsulation”[55]. The different approaches can be further divided into *active* and *passive* approaches, for both *single cell assays* as well as *multi-object single-cell assays* (Fig.1.6).

First, single-cell droplets can be collected after random cell encapsulation from droplet sorting. This can be achieved with either an active or a passive approach. The droplets resulting from the random encapsulation can be empty (in most cases), with one cell, or with more than one cell. During the active sorting, cell-loaded droplets are sorted based on their fluorescence intensity from the fluorescence-labeled cells. Once the fluorescence signal is detected with an optical sensor, a sorting unit will be actuated accordingly to guide the positive droplets to the collection channel. During this process, the laser, sensor, and actuator are all synchronized to perform this task. Single fluorescence-activated and dual fluorescence-based sorting have been demonstrated for single-cell and dual-cell assays. The limitation is the requirement for

cell labeling, which is not always desirable or even feasible. The hardware and software complexity also increases the cost and difficulty in use. One passive method has been developed that follows the post-sorting strategy. Here, droplets smaller than the cell itself are created via the jetting regime (one droplet generation regime that occurs at higher flowrates), where the encapsulation of a cell immediately enlarges the droplet, making it bigger than the rest of the empty droplets to be sorted downstream. However, the drawback of this method is obvious: the size difference between the positive and the negative droplets is not significant and not robust, which brings difficulties for downstream sorting. Particularly, the jetting regime that can produce a droplet diameter smaller than that of a cell is unstable and subject to ambient vibrations that could easily change the default droplet size; in addition, the arrival of a cell disturbs the thin jetting thread and results in increased droplet size for adjacent droplets, both contribute to the unrobust size difference [47]. Due to the mechanism, the obtained single-cell droplet has a small aqueous volume in addition to the cell body and is thus not convenient for downstream manipulations or applications.

The second strategy is to order and equally space the cells such that the cell injection rate can be matched with the droplet generation frequency via flow rate tuning. Within this strategy, there are no active methods. In the passive method, the cell is ordered by the use of Dean flow, where high flow rates and high cell density are required [56, 57]. Currently, when it comes to the passive methods for single-cell encapsulation, this cell ordering method is the most used. It has been demonstrated with single-cell, single bead, single cell-bead, and single cell-cell encapsulations. For the multi-object single-cell assays, the frequencies of both objects, as well as that of droplet generation, all need to be synchronized. With this cell ordering method, it only increases the cell or cell-pair loading ratio instead of giving a deterministic result (demonstrated cell loading efficiency up to 77% [57]). The real-time flow rate tuning for synchronization is conducted at high flow rates, and its success is not guaranteed, making it not readily compatible with standard microfluidic workflow, and subject to lower cell-capture efficiency. For deformable particles, there is another passive particle ordering approach, which is by densely packing them in a narrow channel followed by releasing them at a constant rate that matches with droplet generation frequency [58]. It also requires synchronizing the flow condition to the particle concentration. Due to the adherent property of the cells, it is known that this method does not apply to cells and is not summarized in Fig.1.6.

Another strategy is droplet on demand generation, the name of which already implies that it can only be achieved with active methods. The idea is to detect or directly put a cell at the prepared droplet generation interface followed by applying external force to execute the droplet generation which includes the cell. For multi-object single-cell assays, Bues et. al. [20] detect and stop a single cell and a single particle in a valve structure before performing the droplet generation aided by the valve control, thus co-encapsulating both objects. This strategy has a relatively low throughput. And like all other active methods, the system is more complex and expensive than passive methods.

The last strategy uses hydrodynamic traps for single-cell immobilization, then flows an immis-

cible phase (e.g., oil) to generate droplets around the traps. Here, the throughput is limited by the low aqueous flow rate ( $10\mu\text{L}/h$ ) [33], sequential operation, and the trap numbers per chip. The trap number is further limited by the relatively large single-unit size and the space limit from channel constraints. Essential to this method is the single-cell trapping efficiency, which is limited to below 65 % [59] with nonnegligible empty and multi-cell droplets. To create multi-object single-cell assays, two paths that are close to each other trap different cell types and form the corresponding droplets separately, which are then connected via a valve[60]. In this case, the path that communicates the two original droplets is very small, which, when combined with the laminar low mixing feature and the immobilization of the two cells, does not help the cell-cell communication nor the bead capture of the cell content. The throughput is further limited compared to single-cell assays.

In summary, attempts have been made to overcome the Poisson limit for single-cell encapsulation into droplets. While active methods have the potential to achieve better control, they are more expensive with the complexity and throughput limit and are not versatile to all applications nor readily compatible with simple workflow in microfluidics laboratories. On the other hand, passive strategies are simpler, but the current methods lack control and robustness on the single-cell encapsulation outcomes. A passive yet deterministic, simple, and robust approach for single-cell encapsulation is missing. It hinders many users, including researchers, clinicians, and microfluidics engineers, from accessing easy, cheap, and label-free single-cell droplets for their studies and applications. Active or not, to the best of the author's knowledge, there is no existing droplet microfluidics platform for label-free single-cell encapsulation with ultra-high throughput and high efficiency. This thesis aims to contribute to the droplet microfluidics for single-cell study by developing passive, deterministic, and label-free encapsulation techniques that are ready for use, to improve the single-cell droplet assays and multi-cell (bead) droplet assays.

## 1.2 Research strategy

### 1.2.1 Scope of the thesis

Single-cell study that dissects the cell-cell heterogeneity from bulk populations is of growing attention and importance in biological studies and clinical practices. Among different single-cell isolation tools and platforms, droplet-based microfluidics arises as one of the most popular ones, owing to its accuracy, low cost, high throughput, and flexible control over miniaturized micro-compartments. However, like all other tools, droplet microfluidics has been confronted with the random single-cell encapsulation problem, known as the Poisson limit. It hinders the accurate acquisition and application of various single-cell assays, especially for multi-object single-cell assays that are increasingly popular due to the arising multimodal study of single cells. While many attempts have been set out to overcome the Poisson limit, currently, there is still not any simple and versatile solution.

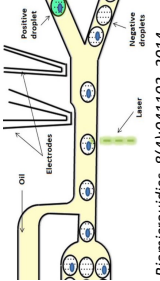
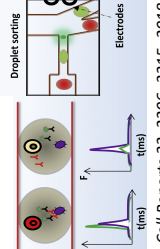
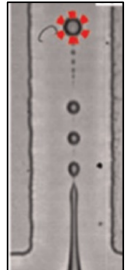
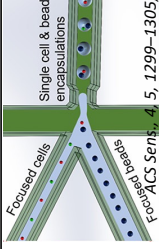
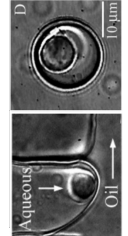
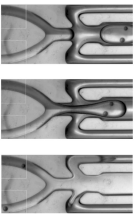
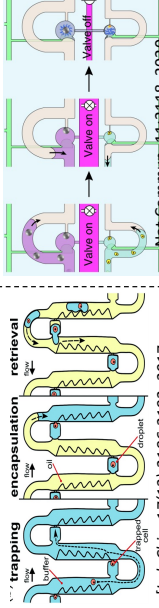
		<b>Active</b>		<b>Passive</b>	
		single cell assay	Multiple cell/bead assay	single cell assay	Multiple cell/bead assay
<b>Post encapsulation droplet sorting</b>	 <p><i>Biomicrofluidics</i>, 8(4):041102, 2014</p>	 <p><i>Cell Reports</i> 22, 2206–2215, 2018</p>	 <p><i>Biosens Bioelectron.</i>, 66:19–23, 2015</p>	 <p><i>ACS Sens.</i>, 4, 1299–1305, 2019</p> <p style="text-align: center;"><b>Not found</b></p>	
<b>Cell ordering</b>	X	X	X	X	X
<b>Droplet on-demand generation</b>	 <p><i>Anal. Chem.</i>, 77(6):1539–1544, 2005</p>	 <p><i>Nat. Methods</i> 19, 323–330, 2022</p>	X	X	X
<b>Trap-assisted encapsulation</b>	X	X	X	 <p><i>Lab Chip</i>, 17(13):2186–2192, 2017</p> <p><i>Nat. Commun.</i>, 11:21118, 2020</p>	X

Figure 1.6 – Summary of current strategies for overcoming Poisson limit. Red crosses present that this category does not exist.

## Chapter 1. Introduction

---

This thesis targets this issue by developing a full set of passive and deterministic single-cell encapsulation techniques, as well as a controlled droplet pairing and merging technique, all are novel in the field. During technological development, we also focused on the physical understanding of a novel type of droplet instability. In the end, we demonstrated that the Poisson limit could be overcome with simple solutions for single-cell assays and multi-object single-cell assays.

### 1.2.2 Structure of the thesis

The thesis can be mainly divided into three parts: a physical study of a droplet breakup phenomenon (Chapter 2), technological development of several single-cell encapsulation tools (Chapters 3-5), and technological development of a droplet pairing and merging tool (Chapter 6). In the end, Chapter 7 is for the summary and conclusion. More specifically:

In **Chapter 2**, we investigate a new type of droplet instability and study the corresponding new breakup regimes from the analytical, experimental, and numerical points of view. This chapter serves as the theoretical foundation for the technologies we developed in Chapter 3.

In **Chapter 3**, towards the deterministic single-cell encapsulation, we developed a post-encapsulation secondary breakup-mediated droplet sorting strategy (CTS). The new droplet instability from Chapter 2 has enabled cell-triggered droplet splitting (CTS), which is the key to this strategy. Several working modes for realizing CTS strategy have been separately demonstrated and characterized, suitable for different application scenarios.

In **Chapter 4**, towards the deterministic single-cell encapsulation, we developed a post-encapsulation direct droplet sorting technology (SCDT). Droplets containing different numbers of single cells have distinguished trajectories and thus can be sorted into different outlets passively. It is the first content-based droplet sorting method with single-cell resolution, with the potential to distinguish the singlets, doublets, and multiplets using simple passive operation.

In **Chapter 5**, towards the deterministic single cell/particle encapsulation, we developed a particle-triggered droplet generation technology (K blocking). Two working modes have been presented. It is the first on-demand droplet generator that operates simply passively, avoiding completely random encapsulation.

In **Chapter 6**, towards the deterministic merging of pre-generated single-cell loaded droplets, we developed a waiting-concept-aided droplet pairing and merging technology (In-flow). It is particularly suited for rare droplet sample handling, where we demonstrated 100 % one-to-one merging for one droplet type.

The **Chapter 7** is dedicated to a summary and discussion of the above technologies towards different application scenarios and a general conclusion of the thesis.

## 2 Mechanism of a new droplet breakup regime in T-junctions

In this chapter, we begin with an in-depth study of a novel droplet breakup phenomenon. It is the physical background of the technologies we will introduce in Chapter 3. The content of the current chapter is based on the preprint on arXiv.org at <https://doi.org/10.48550/arXiv.2207.00077>, which is currently under review at journal *Physical Review Fluids*. The following authors have contributed to the work of this manuscript in its order: Jiande Zhou (corresponding author), Yves-Marie Ducimetière, Daniel Migliozi, Ludovic Keiser, Arnaud Bertsch, François Gallaire, and Philippe Renaud (corresponding author).

### 2.1 Introduction

Droplet formation is a ubiquitous process in both nature and industry. In the context of microfluidics, the controllable generation of micro-droplets has enabled a wide range of applications, opening a new era for biological and chemical analysis and synthesis [26, 61, 62]. To date, droplet formation mechanisms in rectangular microchannels have been widely studied, which can be classified into two main categories [63, 64, 65, 66, 67, 68]: the mechanisms driven by hydrodynamic forces and those driven by surface tension. In the former category, the carrier flow is brought into contact with the dispersed phase, which generates viscous and/or inertial forces that destabilize the two-phase interface and eventually create the droplets. Here, the surface tension act as a stabilizing force that resists the deformation from the hydrodynamic forces. In the latter category, the interface breakup is driven by the surface tension and induced purely by the geometrical setting. A drastic change in the degree of channel confinement causes an imbalance in capillary pressure that leads to the necking and finally breaking of the interface[69]. The first type of mechanism can be realized with three main geometries, including “flow focusing”, “co-flowing”, and “T-junction”. Here the droplet production process is advantageous for high throughput [66, 70, 71]. On the other hand, the surface tension-driven mechanism, although limited by the flow rate, is advantageous for monodisperse droplet production and parallelization [72, 73, 74]. In this chapter, we focus mainly on droplet breakup, a droplet formation process from an existing droplet. One of the most studied geometries for droplet breakup is T-junction. Since the seminal work from Link.

*et al.* in the year 2004[75], various studies have investigated the droplet breakup phenomenon in T-junction, but only the hydrodynamics force-driven mechanism has been reported, where the carrier flow pinches droplet interface at the bifurcate junction and causes the droplet to breakup into two parts. In this chapter, we report a new droplet break-up regime in T-junctions that is surface-tension-driven. Unlike the conventional regime, the droplet interface here ruptures symmetrically in the two arm channels, which gives birth to three daughter droplets instead of two. We investigated the origin of this new regime and, based on that, proposed an analytical design rule to enable this new phenomenon in T-junctions of different dimensions deterministically. With collaborators, we also developed a numerical description of this surface tension-driven breakup process. Finally, we showed experimentally that the hydrodynamic force-driven regime also exists in the same geometry, and by tuning the flow rates both regimes are interchangeable.

## 2.2 Results

### 2.2.1 Discovery of the novel breakup phenomenon

Historically, droplet breakup was conducted in T-junctions where the inlet and outlet channels have the same width and where the channel height is equal to or smaller than the width [75, 76, 77]. In this study, we use a non-conventional T-junction (**Figure 2.1a**) with the inlet and outlet width ( $w_i$  and  $w_o$  respectively) and the height of the channel ( $h$ ) fulfilling  $h > w_i > w_o$ . Consequently, both the aspect ratio ( $h/w_o$ ) and the width ratio ( $w_i/w_o$ ) are larger than unity. Upstream of the T-junction, water-in-oil droplets are generated using a flow-focusing device with two inlets, one introducing deionized water (dispersed phase) and the other fluorinated oil (continuous phase). A third inlet introduces additional oil downstream of the flow-focusing unit in order to separate the droplets and further control their speed. When a droplet passes through the T-junction and fully enters the lateral channels, its rear interface remains pinned at the junction with a constant and convex curvature, whereas the front interfaces advance further downstream. This is in contrast with the central breakup mechanism which features a progressive concave curving of the rear interface during breakup process[75]. Eventually, it is the interfaces inside the lateral channels that collapse and create two new interfaces at a symmetric distance from the junction. This type of breakup creates three daughter droplets rather than two (which is observed during the classical breakup at T-junction). This new breakup is referred to as *lateral breakup*, in comparison to the classical *central breakup* described in the literature. Two examples of droplets undergoing a lateral breakup are presented in **Figure 2.1b**. The collapse is very rapid but can be captured by a high speed camera (inset). The interface appears to break very suddenly during the time the rear cap remains pinned at the junction. It suggests that the necking process, which is usually more gradual, is likely acting off-plane before the final pinch-off happens.

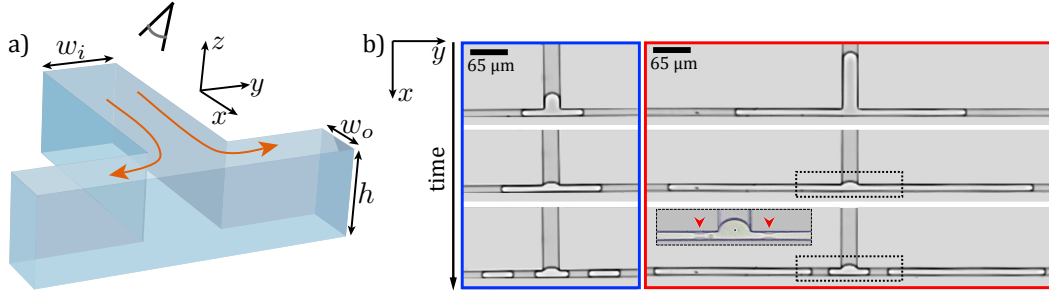


Figure 2.1 – (a) Geometry of the T-junctions used throughout our study: both aspect ratio  $h/w_o$  and width ratio  $w_i/w_o$  are larger than unity. The eye shows the observation perspective during experiment. (b) Time sequence of a lateral breakup process for a short (blue) and a long (red) droplet. Inset shows the interface at the moment of rupture (red arrow), captured at a frame rate of 50,000 fps.

### 2.2.2 Geometric conditions required for the lateral breakup

Next, we investigate why this kind of T-junction geometry enables the lateral breakup that is however non-observable in the conventional T-junctions. Using a quasi-static assumption, we consider that the Young-Laplace equation controls the pressure drop across the interface of the droplet:  $p_d - p = \gamma\kappa$ , where  $p_d$  is the pressure in the drop,  $p$  is the pressure in the surrounding fluid at the interface (**Figure 2.2a**),  $\gamma$  is the interfacial tension, and  $\kappa$  is the local mean curvature of the interface. When the droplet passes through a T-junction whose outlet channels have smaller dimension than the inlet channel ( $w_o < w_i$ ), the curvature at the front of the droplet  $\kappa_o$  increases compared to the curvature at the rear  $\kappa_i$ , thereby creating a pressure gradient along the droplet interface. We assume that the dominant pressure variations occur in the gutters present in the corners of the cross-section, and consider that the pressure in the droplet  $p_d$  can be roughly considered as constant in space and time [77, 78]. It implies that in the fluid surrounding the droplet, the pressure gradually decreases from the rear cap in the inlet channel ( $p_i = p_d - \gamma\kappa_i$ ) to the front cap in the outlet channels ( $p_o = p_d - \gamma\kappa_o$ ), by continuity. This pressure gradient is accompanied by an adaptation of the radius of the gutter  $R_g$ , such that  $p = p_d - \gamma/R_g$ . Along the droplet,  $R_g$  thus varies from  $1/\kappa_i$  in the rear of the droplet to  $1/\kappa_o$  in the front. In the quasi-static condition, the value of  $\kappa_i$  and  $\kappa_o$  is constant and only dependent on the channel geometry[79]:

$$\kappa_{i,o} = \frac{1 + \frac{w_{i,o}}{h} + \sqrt{\left[1 - \frac{w_{i,o}}{h}\right]^2 + \pi \frac{w_{i,o}}{h}}}{w_{i,o}}. \quad (2.1)$$

where  $i$  and  $o$  respectively account for the inlet and outlet. However, due to the confinement and the non-wetting condition  $R_g$  cannot exceed a threshold value given by half of the smallest dimension of the cross-section [72]. In our case  $w_o < h$  which gives a critical value  $R_g^*$  in the outlet channel as  $R_g^* = w_o/2$ . Consequently, if the relatively large pressure imposed in the

## Chapter 2. Mechanism of a new droplet breakup regime in T-junctions

gutter by the proximity of the rear cap imposes a radius of curvature  $R_g$  larger than  $R_g^*$  in the outlet channels, an instability is triggered (**Figure 2.2b**). To fulfill the continuity of pressure along the channel, the interface has to curve concavely in the  $y$  direction, which marks the initiation of a necking process. A “pocket” thus gradually inflates at the upper and bottom part of the channel between the droplet and the  $(x,y)$ -walls, where the continuous phase accumulates. The droplet thereby thins down (necking process) until reaching a quasi-cylindrical shape, when surface tension induces a final and sudden breakup. Such a necking process is off-plane until the last moment of rupture, which is in consistence with the experimental observation. The lateral breakup most often occurs simultaneously in both outlet channels.

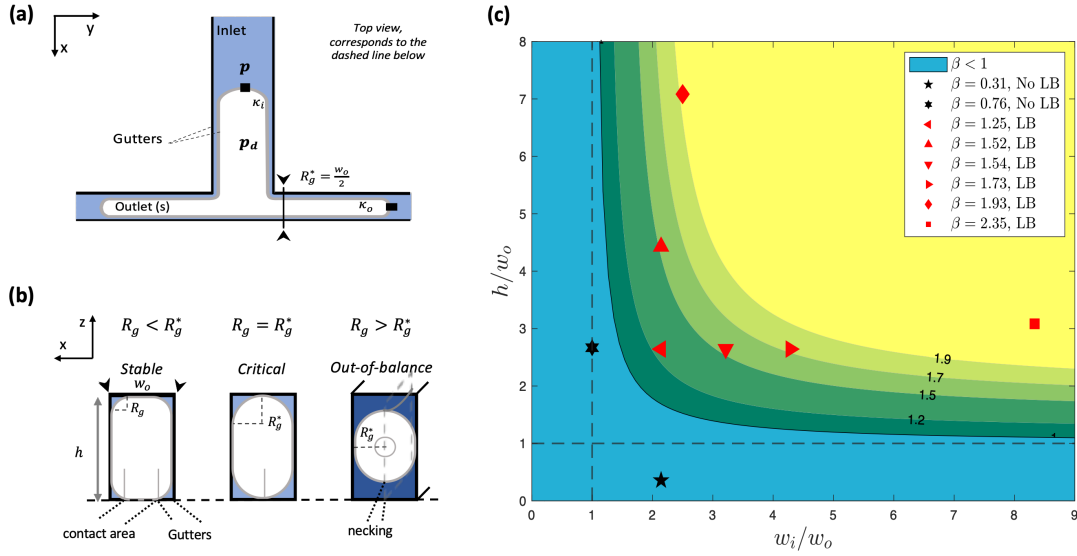


Figure 2.2 – Capillary instability responsible for lateral breakup (a) Presentation of key droplet parameters with a top view of a T-junction through which a droplet splits. (b) Cross sectional view in the outlet channel (indicated by black arrowheads in (a)) showing three different gutter radius. These three conditions can hold for the same droplet passing the junction at different times. When  $R_g > R_g^*$ , the necking starts. (c) Colormap representing  $\beta$  in a diagram representing the aspect ratio  $h/w_o$  as a function of the width ratio  $w_i/w_o$ . Blue region corresponds to  $\beta < 1$ , i.e. geometries that does *not* allow the occurrence of lateral breakup; Green regions correspond to  $\beta > 1$ , i.e. geometries prone to exhibit lateral breakup. Each marker corresponds to one of the geometries experimentally tested (see Table.2.1). A black symbol corresponds to an absence of lateral breakup observed, and a red marker corresponds to a presence of a lateral breakup.

In order to make a passing droplet meet the necking condition of  $R_g > R_g^*$ , the geometric criterion for the T-junction can be expressed as  $1/\kappa_i > R_g^*$ . Defining the confinement parameter  $\beta$  as  $\beta = 2/(\kappa_i w_o)$ , the lateral breakup will thus be prone to happen when  $\beta > 1$ , i.e. when:

$$\beta = 2 \frac{w_i/w_o}{1 + \frac{w_i}{h} + \sqrt{[(1 - \frac{w_i}{h})^2 + \pi \frac{w_i}{h}]} > 1. \quad (2.2)$$

This is an analytical design rule for designing a T junction geometry that allows the lateral breakup to happen, according to our hypothesis. To test this criterion, we selected eight T-junction geometries with different combinations of  $h/w_o$  and  $w_i/w_o$  on which droplet breakup experiments are conducted with varying  $Ca$  (Table.2.1). The outcomes of those experiments are represented in **Figure 2.2c**). No lateral breakup was observed for the two geometries with  $\beta < 1$ , while geometries that have  $\beta > 1$  always showed lateral breakup for a given range of  $Ca$  and  $L$ . In addition, with extreme  $\beta$  values the lateral breakup phenomenon is significantly enhanced Both observations confirm  $\beta$  as a good proxy to evaluate the likelihood of a lateral breakup to happen. We rearrange equation (2.2) and map in fig.2.2c.(ii) the  $\beta$  value of a geometry as a function of its width ratio  $w_i/w_o$  and aspect ratio  $h/w_o$ , where the green to yellow region represents the geometrical conditions of  $\beta > 1$ , which should allow the lateral breakup to occur. Note that a higher  $\beta$  value is always associated with a larger aspect ratio and/or a larger width ratio, shown in the contour map as markers that are further away from the diagonal. It suggests that the capillary instability responsible for the lateral breakup is driven by both of the two ratios. Indeed, the high aspect ratio ( $h > w_o, h > w_i$ ) ensures that the confinement level on a droplet is dictated by the channel width (the smaller dimension). On top of it, the large width ratio ( $w_i > w_o$ ) then imposes the difference of confinement on the same droplet crossing the junction. Both conditions together create the necessary capillary pressure imbalance that eventually drives the lateral breakup.

Table 2.1 – Tested geometries and the corresponding breakup outcome.

Geometry	$w_i$ [ $\mu m$ ]	$w_o$ [ $\mu m$ ]	$h$ [ $\mu m$ ]	$h/w_o$	$w_i/w_o$	$k_i$	$\beta$	Ca range	Lateral breakup
A	30	14	62	4.2	2.1	0.09	1.5	0.005-0.30	Yes
B	30	14	37	2.6	2.1	0.11	1.2	0.006-0.077	Yes
C	30	14	5	0.4	2.1	0.45	0.3	0.006-0.107	No
D	60	14	37	2.6	4.3	0.08	1.7	0.004-0.183	Yes
E	45	14	37	2.6	3.2	0.09	1.5	0.014-0.138	Yes
F	30	30	80	2.8	1	0.09	0.8	0.006-0.160	No
G	100	12	37	3.1	8.3	0.07	2.4	0.035-0.73	Yes
H	30	12	85	7.1	2.5	0.09	1.9	0.02-0.04	Yes

### 2.2.3 Modeling of the dynamics of the lateral breakup for lower Ca

In this section, we illustrate the derivation of a theoretical model with the help of collaborators from the Laboratory of Fluid Mechanics and Instabilities (LFMI), EPFL. This numerical model describes the dynamics of the lateral breakup, occurring in two steps: 1. The droplet progresses through the channel until the necking criterion is met- this is the onset of the necking; and 2. The necking-induced pocket of the continuous phase, fed via the gutters, inflates and thins down the droplet until the final pinch-off. The first step is to find the condition where a minimal value of  $1/R_g^* = 2/w_o$  is met within the outlet channel. At an initial configuration, a droplet of speed  $Ca$  and an initial length  $L(0)$  (not shown) passes the junction, creating gutters of length  $L_i$  and  $L_o$  in the inlet and outlet channel. We assume a homogeneous pressure  $p_d$

## Chapter 2. Mechanism of a new droplet breakup regime in T-junctions

---

inside the droplet and obtain a hydraulic resistance per unit length:

$$r_h(s, t) = \frac{C\mu}{(1 - \pi/4)R_g(s, t)^4}, \quad (2.3)$$

where  $\mu$  is the viscosity of the fluid,  $C$  is a geometric constant with  $C = 93.93$  [80], and  $R_g(s, t)$  is the radius of the gutter along the droplet internal coordinate  $s$ . Note that  $s$  is oriented along  $x$  in the inlet channel and along  $y$  in the right outlet channel. At the rear and front caps we have  $R_g(0, t) = F_i$  and  $R_g(L(t), t) = F_o$ , where  $F_{i,o} = \kappa_{i,o}^{-1}$  is the inverse of the total curvatures of the caps defined in eq. (2.1). The difference between the two induces a flow rate  $q(t)$  of the continuous phase, allocated in 4 gutters in the inlet channel and in  $2 \times 2$  gutters in the outlet channels. Experimentally, we observed a reduction of droplet rear cap speed after the front cap enters the outlet channel (**Figure 2.3b**), which confirms the presence of this total bypass flux  $q(t)$ . Combining the Young-Laplace equation for the pressure balance at the interface  $p(s, t) = p_d - \gamma/R_g(s, t)$  and the Poiseuille equation expressing the pressure gradient within the continuous phase  $\partial p/\partial s = -r_h q/4$ , one obtains an equation controlling the shape of the gutters:

$$\frac{\partial R_g}{\partial s}(s, t) = -\frac{q(t)}{4\gamma} \frac{C\mu}{(1 - \pi/4)} \frac{1}{R_g(s, t)^2}, \quad (2.4)$$

with a continuous change of gutter radius  $R_g(s, t)$  along the droplet from  $F_i$  to  $F_o$ . The quantity  $L(t) = L_i(t) + L_o(t)$  designates the total length of the droplet (excluding caps) along  $s$  the internal abscissa, and is determined by volume conservation from known initial droplet length  $L(0)$  and  $L_i(t)$  (see Appendix). Solving equation (2.4) provides both  $q(t)$  -constant in space due to flow rate conservation- and the gutter radius  $R_g(s, t)$  at any location ( $s$ ) along the droplet:

$$q(t) = \frac{(F_i^3 - F_o^3)}{AL(t)}, \quad \text{and} \quad (2.5)$$

$$R_g^3(s, t) = F_i^3 - q(t)As \quad \text{for} \quad 0 \leq s \leq L(t), \quad (2.6)$$

where  $A = 3C\mu/(4\gamma(1 - \pi/4))$ . By progressively decreasing  $L_i$  from  $L(0)$  (the droplet turns the junction at  $t=0$ ), we find the critical  $L_{ic}$  such that  $R_g = R_g^* = w_o/2$ . Further advancing the droplet,  $R_g > w_o/2$  cannot be met, and the necking has to start. The corresponding critical time  $t_c$  can be obtained from  $L_{ic} = L(0) - Ca t_c$ . **Figure 2.3c** plots  $R_g^3$ , changing linearly from  $F_i^3$  to  $F_o^3$  along the droplet, for three time-stamps and corresponding droplet locations during the advancing of the droplet. It illustrates the following scenario for the onset of the necking: with the droplet advancing in the channel, the rear cap approaches the junction and increases more and more the gutter radius in the outlet channel, which eventually goes beyond the maximum possible value fixed by the outlet channel geometry, thus falling out of balance. Such a process is strongly influenced by the flow rate and droplet size, which change the slope and length of the  $R_g^3$  curve. As the maximum gutter radius along the outlet channel is always attained at the junction location ( $s_j$ ), it is always at the junction that the necking requirement

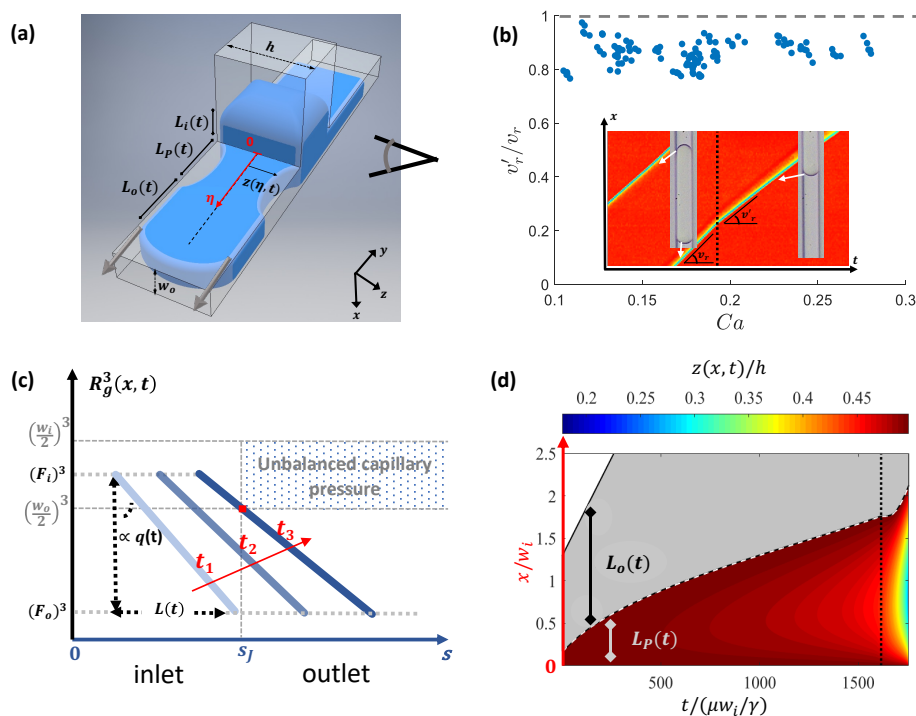


Figure 2.3 – **(a)** Modeling of the pocket development for one arm of the T junction, with the eye showing the observation perspective during the experiment. During the inflation of the lateral pocket, the droplet can be divided into three regions with a length of  $L_i(t)$ ,  $L_p(t)$  and  $L_o(t)$ . The coordinate  $\eta$  starts from the junction and is parallel to the outlet channel. In the parts of length  $L_i(t)$  and  $L_o(t)$ , gutters are maintained, and the gutter flows are represented by grey arrows. **(b)** Relative rear cap velocity  $v_r'/v_r$  (see definition in the inset) once the droplet has entered the junction versus the droplet capillary number  $Ca$  before having penetrated the junction. Inset shows the kymograph from which droplet cap trajectory is measured (yellow line), whose slope before and after the vertical dotted line gives  $v_r$  and  $v_r'$  respectively. **(c)** Result of step 1: schematic plot of equation (2.6) using junction coordinate  $S$ . Each blue curve represents the cubic power of the gutter radius along the droplet, from  $F_i$  at the rear interface in the inlet to  $F_o$  at the front interface in the outlet. Three such gutter radius profiles are shown corresponding to three-time points, i.e., three droplet locations, as the droplet is advancing inside the channel. At  $t_1$ : the droplet is about to enter the junction;  $t_2$ : part of the droplet passes the junction, but the gutter radius inside the outlet channel is below  $R_g^* = w_o/2$ ;  $t_3$ : the droplet further advances and  $R_g = R_g^*$  is met at the red square; from this stage on, further advancing will cause  $R_g > R_g^*$  inside the outlet channel, the onset of necking, a pocket forms and inflates. **(d)** Result of step 2: temporal evolution of the pocket predicted by the model (for geometry  $w_o/h = 14/62$ ,  $w_i/h = 30/62$ , with initial droplet length of  $L/w_o = 8$  and capillary number of  $Ca = 0.005$ ). The vertical axis corresponds to the  $\eta$  coordinate (non-dimensionalized with  $w_i$ ), and the length of  $L_p(t)$  and  $L_o(t)$  are drawn in color and grey respectively as a function of non-dimensional time (horizontal axis); The colormap represents the normalized local pocket depth  $z(s, t)/h$  with the simulation stopped when  $z(s, t)/h$  goes below  $(w_o/h)/2 \approx 0.11$ .

is first met. Thus, the pocket of the continuous phase is expected to start forming from the junction, confirmed by the experiment (shown below).

Now, the droplet enters a second phase consisting of the development of the pocket. To model the evolution of such process, we divide the droplet into three consecutive parts (**Figure 2.3a**): the part in the inlet channel of length  $L_i(t)$  with gutters; The part on the spatial interval of  $0 \leq \eta \leq L_p$ , where  $L_p(t)$  is the length of the pocket, from the junction ( $\eta = 0$ ) to where the droplet curvature in the direction of the flow vanishes ( $\eta = L_p(t)$ ). The third part corresponds to the remaining part of the droplet in the outlet channels where the gutter is resumed, of length  $L_o(t)$ . In the pocket region, we parametrize the droplet surface by its curvature in the flow direction (i.e, the curvature in the  $y-z$  plane in **Figure 2.3a**), defined as

$$k(\eta, t) = -\frac{\partial}{\partial \eta} \left[ \frac{\partial z(\eta, t) / \partial \eta}{\sqrt{1 + (\partial z(\eta, t) / \partial \eta)^2}} \right]. \quad (2.7)$$

Where  $z \in [w_o/2; h/2]$  designates the interfacial position:  $z$  equals  $h/2$  when no pocket is formed and gutters are maintained, and  $z = w_o/2$  corresponds to a cylindrical droplet cross-section that represents the endpoint of the pocket development. The curvature in the direction perpendicular to the flow, i.e, the curvature in the  $x-z$  plane in **Figure 2.3a**, is assumed constant and equals to  $2/w_o$ , such that the total curvature of the droplet in the pocket region writes  $k(\eta, t) + 2/w_o$ . We then define the continuity equation for the continuous phase as  $\partial S / \partial t = (\partial q / \partial x) / 2$ , where  $S[z(\eta, t)] = (\pi - 4)w_o^2/4 + 2z(\eta, t)w_o$  is the cross-sectional area of the discrete phase in one outlet channel, which is fed by two quarter-sections at the top wall with a flow rate of  $q(\eta, t)/4$  in each. We apply the derivative to the equation of the pressure balance at the interface to obtain the flow rate

$$q(\eta, t) = \frac{\gamma}{r_{h,S}[z(\eta, t)]} \frac{\partial k(\eta, t)}{\partial \eta}, \quad (2.8)$$

where  $r_{h,S}[z(\eta, t)]$  designates the hydrodynamic resistance per unit length of a quarter-section, which reduces to equation (2.3) for  $z = h/2$ . Injecting both the expression for  $S[z(\eta, t)]$  and equation (2.8) in the continuity equation leads to

$$\frac{\partial z(\eta, t)}{\partial t} = \frac{4\gamma}{w_o} \frac{\partial}{\partial \eta} \left( \frac{1}{r_{h,S}[z(\eta, t)]} \frac{\partial k(\eta, t)}{\partial \eta} \right), \quad (2.9)$$

such that equation (2.7) and equation (2.9) constitute a system of two coupled equations for the two unknowns  $z(\eta, t)$  and  $k(\eta, t)$ . It is subject to two boundary conditions for  $z$ :  $z(0, t) = z(L_p(t), t) = h/2$ , as well as two for  $k$ :  $k(0, t) = \kappa_J - 2/w_o$ , and  $k(L_p(t), t) = 0$ , where  $\kappa_J$  is the curvature of the inlet gutter at the junction, found by matching with the inlet gutter regime (see Appendix). As mentioned, the necking condition has already been met, thus  $k(0, t) \leq 0$ , resulting in the opening of the pocket; however,  $k(\eta, t)$  must increase with  $\eta$  until recovering  $k(L_p(t), t) = 0$ , as the hydrodynamic resistance induces a pressure drop of the continuous phase (see equation (2.8)). We used a finite element method to calculate the

dynamics of the necking process numerically, i.e.  $z(\eta, t)$  and  $k(\eta, t)$ . The boundary conditions, numerical discretization, and nondimensionalization used for this purpose are detailed in the appendix A.1 and numerical methods section. The result of the simulation resolves the pocket evolution process, which can be represented by the change of pocket length  $L_p(t)$  and depth  $z(\eta, t)$  (**Figure 2.3d**). These two quantities increase over time, with a monotonic downstream extension of the pocket boundary. As  $z(\eta, t) = w_o/2$ , a locally cylindrical cross-section is reached during the pocket evolution, which triggers a fast breakup controlled by surface tension.

This model is restricted to low  $Ca$  for two main reasons. First, large values of  $Ca$  may lead to a cross-section occupancy of both liquids, which is not accounted for in our gutter model, as evidenced by Lozar *et al.* [81]. Second, the internal viscous dissipation has an increasing contribution at higher  $Ca$ , and was not included in the model. Experimentally, we observed the evolution of lateral breakup behavior from low to high  $Ca$  condition. For lower  $Ca$ , a pocket-forming process starts and stops before the rear interface reaches the junction. The corresponding breakup distance from the junction decreases with increasing  $Ca$  (**Figure 2.4**). For higher  $Ca$ , the breakup location is stabilized, and an decreasing rear cap curvature is observed as  $Ca$  increases (**Figure 2.4**). We next discuss the latter case concerning higher  $Ca$ .

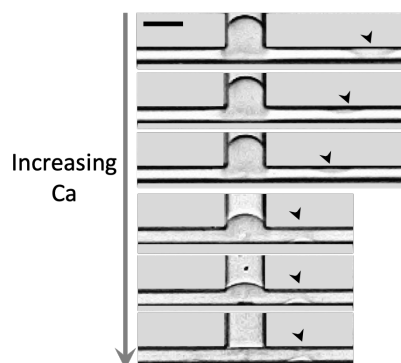


Figure 2.4 – Breakup moment of six breakup events with increasing  $Ca$ . The  $Ca$  value from top to bottom is 0.016, 0.025, 0.056, 0.088, 0.129 and 0.177. The breakup location in the right outlet channel is shown with black arrowheads. The scale bar represents  $30 \mu\text{m}$ .

#### 2.2.4 A central breakup recovered at higher $Ca$

At higher  $Ca$ , when a critical  $Ca^*$  is exceeded, the conventional central breakup regime can be recovered, even for geometries enabling lateral breakup. **Figure 2.5a** shows three breakup events with the same droplet size. Central breakup is observed at higher values of  $Ca$ , while lateral and central breakups can occur simultaneously near the critical value  $Ca^*$ . In **Figure 2.5b** we show light intensity kymographs of two breakup events with the same droplet size but different breakup regimes. The existence of the lateral pocket cannot be imaged directly, but it can be detected by a faint intensity change, caused by the light scattering at the openings. First,

it confirms that the necking starts from the junction as predicted by our model (Appendix 2.2.3). Second, it is remarkable to discover that pocket formation occurs regardless of the final breakup outcome. This observation, together with the coexistence of lateral and central breakups near the critical  $Ca^*$  indicates that the two processes are simultaneous. It hints at the breakup transition mechanism, attributed to the faster completion of central breakup that aborts the lateral breakup process with the interfacial rearrangement.

We obtained the regime map near the transition zone for  $Ca_o$  versus  $\bar{L}_o$  in **Figure 2.5c**. Here,  $Ca_o = Ca(w_i/w_o)/2$  is the outlet channel capillary number, and  $\bar{L}_o = L(0)(w_i/w_o)/w_o/2$  is the initial droplet length translated into outlet channel (divided by 2 for only one branch) normalized by the outlet width. We compare the characteristic breakup time for both regimes, defined as the duration from the rear cap reaching the corner until the breakup and represented in **Figure 2.5c** as the surface area of the round markers. Interestingly, the characteristic time decreases approximately with increasing  $Ca$  for both regimes. But at each transition point, the central breakup always has a shorter characteristic time than the adjacent lateral breakup. From the regime map, a longer droplet needs a lower critical  $Ca_o^*$  to transition to central breakup. We found that the relation between  $\bar{L}_o$  and its transition  $Ca_o^*$  can be well described by the scaling law  $Ca_o^* \sim b\bar{L}_o^{-1}$ . The latter is also found to describe the non-breakup/central breakup transition on conventional T-junctions for long droplets [77]. This indicates that the lateral/central breakup transition is probably dictated by enabling the central breakup, which is the faster process. This leads to a critical constant  $(Ca_o\bar{L}_o)^*$  that solely governs the lateral/central breakup transition. In the inset of **Figure 2.5c**, the separation of the two regimes by  $(Ca_o\bar{L}_o)^* \approx 1.9$  is shown.

However, this experimentally determined prefactor is much higher than the theoretical value obtained for the same geometry (A) but assuming no lateral breakup following the scaling analysis of Haringa *et al.* [77](see Appendix). We note the difference in enabling central breakup on these new T-junctions. The continuous flow arriving at the junction can: (a) bypass the entire droplet through gutters, (b) flows into the lateral pocket and increase its volume, or (c) push the rear cap and contribute to central breakup. In conventional T-junctions, there is no pathway (b), and (a) is negligible at higher  $Ca$ [77]. In the lateral breakup-enabled T-junctions, the pathway (a) may be enhanced by an enlarged ‘‘gutter’’ area of the continuous phase when  $Ca$  is high (prominent for high aspect ratio channel [81]). Together with the uniquely presented pathway (b), it indicates that the lateral breakup-enabled T-junction uses a smaller portion of the incoming flow for central breakup than a conventional T-junction. This means for the same droplet length  $\bar{L}_o$ , a higher  $Ca_o^*$  is required to enable the central breakup and the transition, reflected by the increased constant  $(Ca_o\bar{L}_o)^*$ . In **Figure 2.5c** we map the breakup regimes near the transition zone for four geometries with the same outlet widths in a logarithmic scale (From geometries A, B, D and E described in the Table). The decay rate of  $Ca_o^*$  with  $\bar{L}_o$  is similar for all the tested geometries as a power law with an exponent close to -1, similar to the above observation. The intersect of these -1 laws, proportional to the constant  $(Ca_o\bar{L}_o)^*$ , varies among the geometries. Geometries with a more prominent lateral breakup (higher value of  $\beta$ ) require a higher  $Ca_o^*$  to recover central breakup.

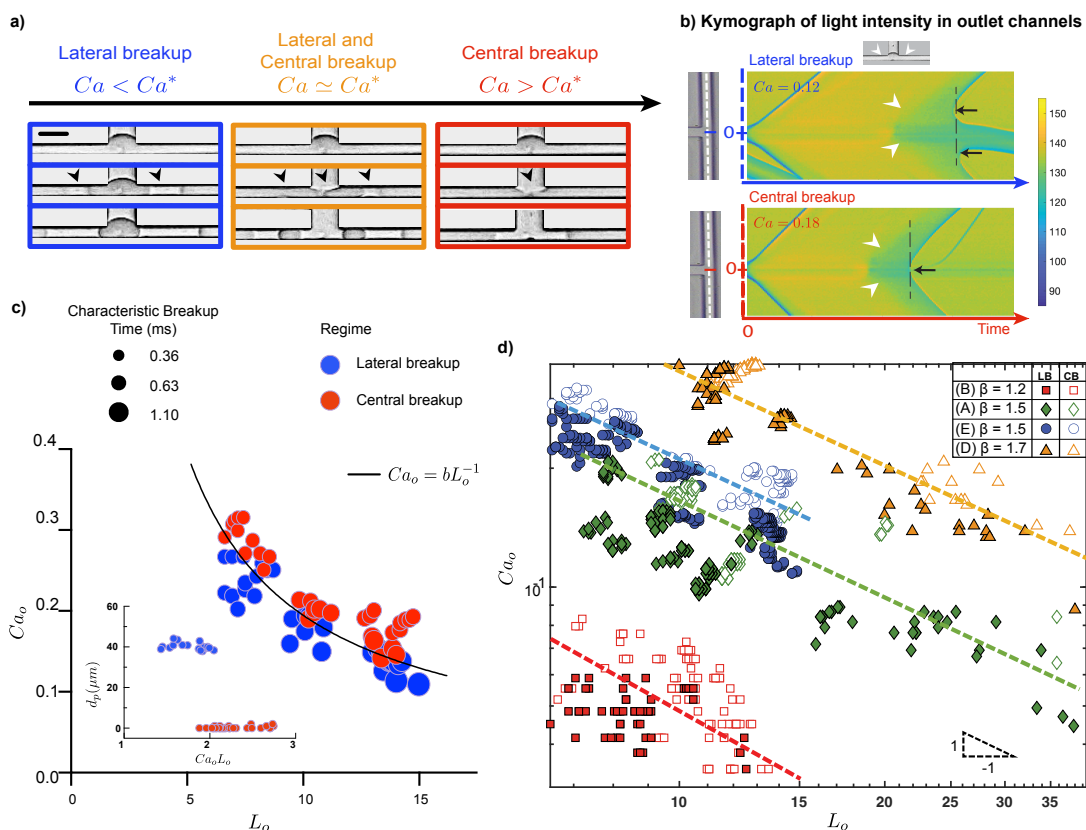


Figure 2.5 – (a) Time sequences of example breakup events for the same droplet length under three flow conditions. The breakup regime shifts from lateral to central breakup from low to high  $Ca$ . The scale bar represents  $30 \mu\text{m}$ . (b) Kymograph of light intensity along the central part of the outlet channel (white dashed line), for two droplets of the same size but with different regimes; The grey value is turned into colors in the colormap. At time zero, both droplets enter the junction, and the trajectory of the front interface forms a straight line. After the rear interface arrives at the junction (inset), the intensity change due to the light scattering from the pocket interface is captured (white arrowheads), which always starts from the junction as predicted. At the end of each process, a new interface(s) is formed at the locations indicated by the black arrows. (c) The breakup transition regime map of  $Ca_o$  versus  $\bar{L}_o$  for geometry A (Figure 2.2c), where  $Ca_o = Ca(w_i/w_o)/2$  and  $\bar{L}_o = L(0)(w_i/w_o)/w_o/2$ . Blue and red circles represent lateral and central breakups, respectively. The area of each circle is proportional to the characteristic breakup time, defined from when the droplet rear interface reaches the junction to the final breakup moment. The black curve represents the function  $Ca_o = b\bar{L}_o^{-1}$ , where  $b = 1.9$  in this case (geometry A). Inset:  $d_p$ , the pinch-off lateral distance from the junction center (in  $\mu\text{m}$ ) versus the product of  $Ca_o\bar{L}_o$ . (d) Logarithmic representation of the breakup transition regime map for  $Ca_o$  vs.  $\bar{L}_o$  for four geometries (A, B, D, E) with different  $\beta$  values, represented by four colors. The filled and hollow markers represent lateral (LB) and central breakups (CB). Dashed lines of slope  $-1$  are represented to guide the eyes.

We also mention that the geometry may alter the relative time scale of the two processes.

## Chapter 2. Mechanism of a new droplet breakup regime in T-junctions

For example, on geometries that favor less the lateral breakup (e.g. geometry B), there is no lateral/central simultaneous breakup near the transition region as shown in **Figure 2.5a** for geometry A, indicating a much slower lateral breakup at this moment than the central breakup. We thus warn that it is not impossible to have a lateral breakup process terminating before the central breakup process (of droplet flattening, concaving, and finally pinching off), provided that the geometry promotes lateral breakup to have its process finished earlier. In a nutshell, the droplet breakup fate in these novel T-junctions should be determined by the temporal dynamics of both breakup processes and is dominated by the faster one. This means the two most common droplet formation mechanisms in microfluidics- driven by a hydrodynamic force and driven by surface tension, simultaneously compete in the same geometry. By merely shifting flow condition, the droplet size and/or composition can be changed at real-time (**Figure 2.6**).

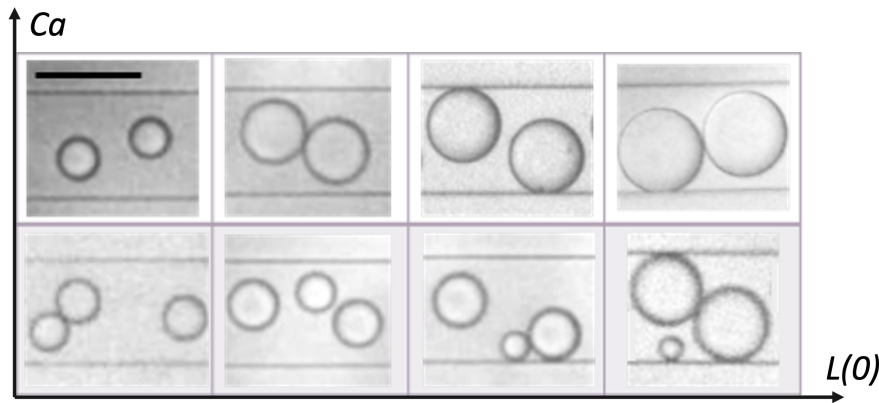


Figure 2.6 – Different daughter droplet composition from each droplet breakup event, with geometry B. From top to bottom: increasing the number of daughter droplets (by decreasing the capillary number  $Ca$ ). From left to right: increasing the daughter droplet size and/or size ratio (by increasing the droplet length  $L_o$ ). The scale bar represents  $100 \mu\text{m}$ .

## 2.3 Methods

### 2.3.1 Device fabrication

A silicon mold fabricated by Dry Reactive Ion Etching (DRIE) was used to create the microchannels. First, a  $1.5 \mu\text{m}$  photoresist layer was spin-coated on a double-side polished silicon wafer and was patterned with standard photolithography, including steps of exposure and development to obtain the 2D channel shape. The exposed wafer area was then etched using the Bosch process (DRIE, Alcatel AMS 200). The channel depth is proportional to the etching duration, and the value is measured with a surface profilometer (Tencor Alpha-Step 500). After the Si mold was silanized within a trichlor-(1H,1H,2H,2H-perfluorooctyl) (PFOTs)-filled desiccator for five hours, we poured PDMS pre-polymer (1:10 ratio mixture) onto the Si mold

and cure in 80°oven for three hours. We peel the PDMS replicas from the mold and, after punching inlet and outlet holes, seal the channels by bonding to a PDMS-coated glass slide (oxygen plasma bonding, 500 mTorr, 45 sec, 29 W). Coating of the glass slide (standard 25mm \* 75mm \* 1mm) is done by spin coating a thin layer of PDMS pre-polymer at 1700 rpm for 35s, then curing in the oven (as above). The hydrophobicity of the surfaces was naturally regained by placing PDMS in the oven for 3 days.

### 2.3.2 Experiments

The experiments were performed under an inverted microscope (Nikon Eclipse TE 300) and imaged with a high-speed camera (Phantom Miro M310). A syringe pump (CETONI Nemesys) with gastight glass syringes (Hamilton) controls the flow rates injected into the system. Depending on the flow rates, frame rates up to 50,000 frames per second were used to record the droplet breakup process. A customized ImageJ script is used to recognize the droplets and obtain the intensity profile automatically. A MATLAB (Mathworks) script calculates the droplet speed and length. The results were confronted with the observations to ensure accuracy.

To conduct the experiments, constant flow rates were fed to the system using CETONI Nemesys syringe pumps (Low-pressure module, Cetoni GmbH, Germany), 100  $\mu$ l gastight glass syringes (Hamilton 1700 Series), and Tygon tubings (Masterflex). To avoid possible fluctuations in the system, we used the actual droplet speed determined from the video to determine the capillary number. QX200<sup>TM</sup> Droplet Generation Oil from Bio-Rad (containing surfactant) was used for the continuous phase to avoid droplet coalescence. Deionized water was used for the dispersed phase. The viscosity of the droplet generation oil was measured using a rheometer (DHR-3 TA):  $\mu = 2.3$  mPa.s. The interfacial tension between the two phases was measured with the pendant drop method (Kruss Advance 1.6.2.0):  $\gamma = 1.6$  mN/m.

Table 2.1 lists the full  $Ca$  range we have tested for each geometry. For **geometries A,B,D,E** (positive geometries with normal aspect- and width- ratio), we conducted systematic experiments, and the results involving the LB/CB transition at the higher  $Ca$  range is shown in Fig.2.5 (please note the different definition of  $Ca$  and  $Ca_o$  for Table 1 and Fig.2.5). **Geometries G and H** (with high aspect- or width- ratio) are less characterized. After observing the LB phenomenon, we labeled them as positive geometries and reported the  $Ca$  range we have tested. Particularly, for geometry G (high width ratio), we observed for the whole  $Ca$  range only LB (no CB even at high  $Ca$ ); for geometry H (large aspect ratio), we observed multiple LB (instead of 1 LB) for each droplet, with the last breakup for the last part of the droplet can be LB (lower  $Ca$ ) or CB (higher  $Ca$ ). As we didn't have systematic characterization for these two geometries, these "enhanced" LB phenomenon is not explicitly described in the main text. For **geometry C and F** (negative geometries), after we observed CB, we lowered the  $Ca$  until seeing droplet non-breakup (droplet escaping, for geometry F), or until seeing it is still CB, but we reached the system limit (our high precision syringe pump cannot provide lower than 0.006  $\mu$ L/min flow rate; for geometry C). We labeled these two geometries as negative

geometries and reported the corresponding  $Ca$  range.

## 2.4 Discussion

### 2.4.1 Limitations of the current numerical model

In this chapter, we presented the study of a novel droplet breakup at a microfluidic T-junction. To shed light on the underlying dynamics leading to the new lateral breakup mechanism, we developed a model predicting the formation and growth of a pocket of the continuous phase in the low  $Ca$  regime. Such a numerical description of the breakup dynamics is meaningful as the dynamics couldn't be described from experimental data alone since it occurs in the unobserved plane. The model established the following scenario for the progressive inflation of a lateral pocket in the outlet channel: with the droplet advancing in the channel, the rear cap approaches the junction and decreases more and more the gutter curvature at this location, which eventually drops below the minimum possible value fixed by the outlet channel geometry. Exceeding this limit must lead to an increasingly negative curvature in the direction orthogonal to the flow, which leads to the inflation of the continuous phase pocket. Our modeling framework could also be applied to other surface-tension-driven breakup problems.

However, it is important to point out that this model is currently restricted to low  $Ca$  for several reasons: 1) as previously evidenced for bubbles [81], large values of  $Ca$  may lead to a flow configuration where the oil occupies more the cross-section and the gutter representation used in our model is no longer valid. 2) Both the internal dissipation and elongational resistance of the droplet, increasingly important with higher  $Ca$ , have not been included in our model. 3) Eventually, when the rear cap of the droplet arrives at the junction, a high  $Ca$  number would lead to an abrupt increase of flow rate entering the pocket, which may lead to a three-dimensional geometrical rearrangement of the droplet that we have no evidence for.

Moreover, there is currently a lack of comparison between the experimental results and the simulation model. During our experiments, we observed that the droplet breakup dynamics are not systematic at a lower  $Ca$  range (i.e.,  $Ca < 0.05$ ). Indeed, the droplet positions at the junction while waiting for the lateral breakup to happen are not fixed well, with back-and-forth oscillations of the droplet front interfaces. This raises the difficulty of robust measurement. At higher  $Ca$  ( $Ca > 0.1$ ), the droplet breakup dynamics become robust and systematic, but the simulation is unsuitable for higher  $Ca$  conditions. Therefore, we did not obtain a meaningful comparison between the simulation and the experiment. This could be left for future studies after optimizing the experimental design and conditions.

### 2.4.2 Deep channel effect

Previously in the field, almost all droplet breakup studies were conducted in shallow channels with a height-to-width ratio smaller than 1, whereas in our work, we have worked on a deep

channel with this ratio larger than 1. This explains why such a droplet breakup phenomenon is not discovered so far. In fact, from the derivation of the analytical design rule, we can see that the necking criterion for the capillary instability to occur (i.e.,  $R_g > R_g^* = w_o/2$ ) is analogous to the one ruling step emulsification [69] or snap-off [80] processes.

In the previous studies, step emulsification can only be induced by a “step” geometry where the channel height and width are both drastically increased, requiring non-standard fabrication procedures. Our finding points out that this is not necessary. For a rectangular channel, by setting up  $h \gg w$ , the droplet confinement level is dictated by the smaller dimension ( $w$ ). Thus, a single height and solely variations in the x-y plane generate the necessary change of confinement for inducing the capillary instability. In our case, although we have  $w_i > w_o$ , the width change is not drastic. It induces the capillary instability, but the actual breakup location varies with flow condition (Fig.2.4). If the width contrast is larger with a significant step, the lateral breakup location will be confined at (around) the step location. This is like step emulsification, only that it is achieved on a single-height device. We used this effect in Chapter 3 for single-cell encapsulation purposes.

### 2.4.3 The real cause for the transition

Experimentally, we have shown that the transition from LB to CB happens systematically at the higher  $Ca$  and larger  $L$  condition. For LB, the increase in droplet speed ( $Ca$ ) decreases the residence time of a droplet in the junction and so thus the time for the instability to develop, weakening the lateral breakup. For CB, the increase in droplet speed and length are both the causes of an enhanced pinching flow at the back of the droplet rear interface, which help overcome the Laplace pressure and drilling of the interface for the central breakup (CB). That is to say, when  $Ca$  and  $L$  are both larger, by default LB is weaker, and CB is stronger. An interesting question, therefore, is whether the transition from LB to CB at higher  $Ca$  and  $L$  is caused by the *disappearance of LB*, the *appearance of CB*, or both.

In T junction with deep channels (i.e., in our case), we have **non breakup -> LB -> CB** from vanishing  $Ca$  to higher  $Ca$ . For the LB -> CB transition, we systematically observed a -1 power law describing the dependency of the critical  $Ca^*$  on the droplet length  $L$  on different tested geometries. This drew our attention, as such a dependency is also observed in T-junctions with shallow channels (i.e, in the conventional studies), where it describes the transition of **non-breakup -> CB** (LB is forbidden). It indicates that a -1 power law is associated with the enabling of CB (for an elongated droplet as in our case). It is therefore tempting to consider that the transition of LB -> CB in deep channel T-junction, governed by a -1 power law, is also due to the enabling of CB, which ceases the LB process with droplet interface re-arranging. Out of curiosity, we later conducted a new study on geometry without a T junction but the deep channel and width ratio conditions are still fulfilled; thus, LB can still happen but not CB (Fig.2.7a (L)). We first verified if the same design rule still applies on this straight channel geometry ((Fig.2.7b). We flow droplets under different conditions in geometries with different

## Chapter 2. Mechanism of a new droplet breakup regime in T-junctions

parameters, and we clearly see that the same design rule predicts the presence of the LB in the (green) geometries very well. In one of the LB-positive geometries we characterized the breakup phenomena with respect to the droplet speed (y-axis) and droplet length (x-axis), shown in Fig.2.7c. Roughly speaking, from low to high  $Ca$ , the droplets experience from LB (green to yellow points) to non-breakup (blue points). Again, when LB happens, the breakup happens within the narrow section. The breakup location defined as the distance from the step to the breakup point inside the narrow section is shown with the color code. A lower droplet speed leads to a longer breakup location, while at a higher speed this distance is shorter and starts to get stabilized at around  $40 - 50 \mu m$ . This trend is similar to what we have observed in Fig. 2.4 with a T junction configuration. It shows that the straight channel configuration has captured well the lateral breakup features we observed in the previous studies.

In this case, let's look at the LB  $\rightarrow$  non-breakup transition, which describes the "disappearance of LB". It confirms that when droplet speed and length are larger, LB is indeed weaker and will eventually stop (i.e., nonbreakup). However, the transition rule here is not characterized by a "-1" power law but more like a "-0.5" power law (insert). It indicates that the influence of droplet length is weaker compared to CB. More importantly, it confirms that the transition of LB  $\rightarrow$  CB as we discussed above in a T junction geometry is *not* characterized by the disappearance of the LB, which would have been a "-0.5" power law. Instead, this transition is indeed dictated by the appearance of CB, which is a -1 law.

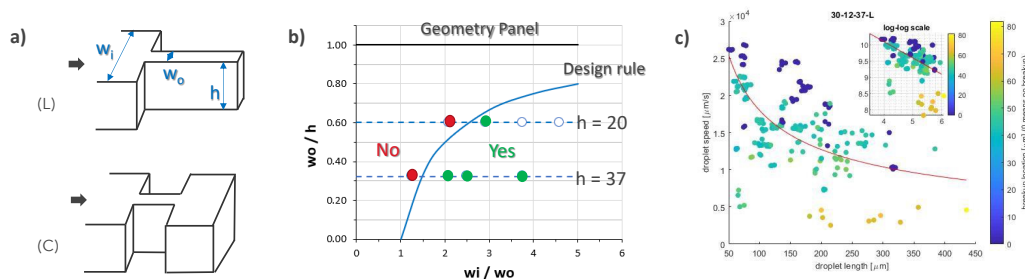


Figure 2.7 – a) Schematics and parameters used for the straight channel geometry; (L) is for geometry law verification experiments, (C) is for the cell experiments, which we will present in Chapter 3; b) Result of whether the droplet breakup can be observed in each (L) type geometry. Red points represent that in this geometry no droplet breakup inside the narrow section can be observed at all flow conditions. Green points mean that droplet breakup can happen, and the transparent points represent the geometries that are not tested in the end. The design rule is plotted as the blue curve, below which the geometries fulfill the capillary instability requirement presented in Chapter 2; c) The breakup location (in color) at different droplet lengths (x-axis) and speeds (y-axis). The breakup location is defined as the distance from the start of the narrow section (the step in the geometry) to the breakup point inside the narrow section, where 0 (blue) means no breakup happens. The non-blue points show the change of breakup location with flow conditions.

## 2.5 Conclusion and outlook

In summary, we reported on a novel lateral droplet breakup occurring in microfluidic T-junctions which leads to the formation of three daughter droplets. We experimentally evidenced that this new regime arises from an unbalanced capillary pressure at the drop interface induced by the strong gradient of confinement across the junction (provided that  $h > w_i > w_o$ ). A geometrical design rule was proposed accordingly to enable the lateral breakup regime. We also developed a model depicting the development of the lateral pockets responsible for the ultimate lateral breakup, for low capillary number  $Ca$ . Furthermore, we showed that a unique central breakup is recovered at higher  $Ca$ , a regime also observed in conventional T-junction. We showed that the critical capillary number  $Ca^*$  marking the transition from lateral to central breakup is compatible with an inverse dependency on the droplet length. This means the two main breakup mechanisms in microfluidics- hydrodynamic force-driven and surface tension-driven, simultaneously compete in the same geometry. This allows new microfluidics functionalities. On one hand, active control over the flow condition can change droplet composition and sizes without changing geometries; On the other hand, without active control, the change of the content or property of the droplet could possibly alter the temporal competition of the two breakup regimes thus shifting the breakup results. In the next Chapter, we will explore the possibility of passive control.



# 3 Deterministic single cell encapsulation based on Cell Triggered Splitting (CTS)

In the previous chapter, we thoroughly studied a novel droplet breakup phenomenon on a special type of T junction. In this chapter, we applied this understanding and developed a simple passive strategy for the deterministic encapsulation of single cells into droplets. Two geometries with different working principles derived from the same physical phenomenon (chapter2) are presented. This chapter is based on two paper manuscripts.

## 3.1 Introduction

As stated in the introduction chapter, the Poisson limit hinders single-cell study and needs to be tackled. The current approaches, passive or active, are not adequate for this purpose. From chapter 2, we have understood that in microfluidics T junctions that have both deep channels and a channel width change, a surface tension-driven droplet breakup regime is possible. At the same time, a droplet can also be split into two equal parts at the center of the T junction with a hydrodynamic force-driven mechanism. Both mechanisms compete in such a T junction, thus the droplets may experience different breakup outcomes- break into *two* with the hydrodynamic force-driven regime, or break into *three* with the surface tension-driven regime. While we have presented how an active switching of the flow condition can alter the competition outcome, in this chapter, we will present that a similar effect can be induced by a passive change of the droplet content. We use this effect to design our first single-cell encapsulation strategy, “Cell triggered splitting” (CTS).

## 3.2 The general strategy

As discussed in Chapter 2, the degree of confinement change is proportional to the degree of width change in deep channel geometry. While a small width contrast is not strong enough to restrict the breakup location, causing floating breakup sites in the narrow section (Fig.2.4), a drastic width contrast will confine the breakup location at the step between the narrower section and the wider section, inducing a breakup phenomenon similar to the known “Step

### Chapter 3. Deterministic single cell encapsulation based on Cell Triggered Splitting (CTS)

emulsification” - except that the “step” is created in the 2D channels (with the same height). Our two flow configurations for CTS (CTS-1 & CTS-2) have used small-width contrast and large-width contrast breakup phenomenon, respectively.

The general idea of CTS is shown in Fig. 3.1. At the first step of droplet generation (a), a random cell encapsulation is performed with low cell density ( $\lambda = 0.1$  to  $0.2$ ), producing *mother* droplets that are mostly empty or containing a single cell[82]. In the second step of droplet splitting (b), the mother droplets flow through the novel T junction, where empty droplets break into two parts, and the cell-loaded droplets break into three parts due to the perturbation from the cell to the system (CTS). In the following sections, we will show two ways of achieving such switching of droplet breakup regimes. One aspect in common, however, is the fact that the cell-triggered droplet splitting creates an additional *daughter* droplet containing that cell, which has a different size compared to the rest of the empty daughter droplets. As a result, the previously-random cell occupancy in equally sized mother droplets is transformed such that the new droplet sizes are correlated with their cell occupancy. All cell-containing droplets will have a distinct size. In the last step of droplet sorting (c), these cell-containing droplets can be collected automatically via any droplet size-based sorting method. All three steps are performed in one chip in a passive manner.

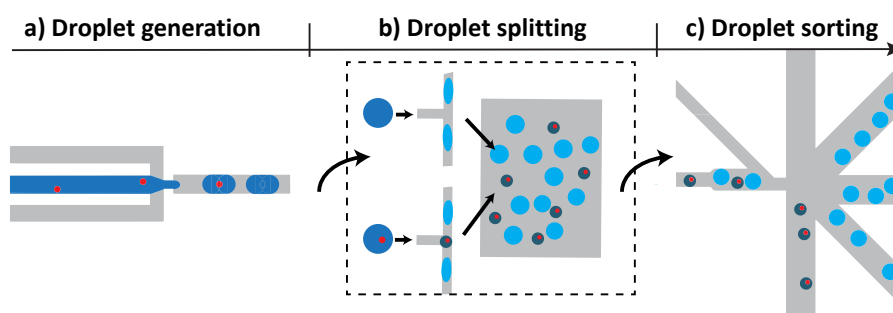


Figure 3.1 – **Overview of the CTS single cell encapsulation strategy:** a) Random cell encapsulation generating mother droplets of different content; b) CTS junction where empty and cell-loaded mother droplets are split differently, creating different droplet sizes that are linked to their the cell occupancy; c) The smaller droplets which always contain the cells are sorted passively based on size, here demonstrated with Pinched Flow Fractionation (PFF)[83].

In this chapter, we will demonstrate two CTS geometries that have been studied. In both cases, we used three inlets for operation- two inlets introducing water and oil are for the droplet generation; one additional oil flowrate is added downstream of the droplet generation unit before the droplet splitting geometry, for droplet spacing and droplet speed regulation.

### 3.3 Methods

#### 3.3.1 Chip fabrication

For both CTS-1 and CTS-2, we produce Polydimethylsiloxane (PDMS) replicas from silicon molds, then seal them with glass slides to produce the chips. For the silicon mold fabrication, AZ ECI 3007 photoresist ( $1.5 \mu m$ ) is used during standard photolithography. Then, the wafer with a patterned photoresist is etched with Dry Reactive Ion Etching (DRIE) using the Bosch process (Alcatel AMS 200). The etching time determines the height of the channels, the latter is measured with a surface profilometer (Tencor Alpha-Step 500). The obtained Si mold was silanized with trichloro-(1H,1H,2H,2H-perfluorooctyl) silane in a desiccator for five hours, which makes it ready for PDMS molding (using a 1: 10 mixing ratio). After the molding, we bond the PDMS replica to a glass slide with oxygen plasma (1 min, 29 W). The hydrophobicity of the channels was obtained by placing the freshly bonded device (with the activated surface) in the above-mentioned PFOTS-filled desiccator for five hours.

#### 3.3.2 Chip design and scaling (CTS-1)

For the deformable object of different sizes to be encapsulated, we give the following rules to scale the CTS-1 chip: First,  $w_o$  is chosen to be slightly smaller than the target object size. For relatively more rigid objects, the dimension difference between the object size and the  $w_o$  can be smaller. Then, the width ratio ( $\frac{w_i}{w_o}$ ) and aspect ratio ( $\frac{w_i}{h}$ ) can be chosen according to Eq.2.2 and according to the throughput requirement. A rare cell sample normally has a small sample volume and might require a lower flow rate, while a large sample might prefer a higher throughput. For a given geometry, the throughput can be adjusted by changing the operational flow condition along the (fixed) transition flow conditions (see below). In addition, the transition boundary itself can be significantly altered by the geometry as shown in Chapter2, mainly with the change of the aspect and width ratio ( $h/w_o$  and  $w_i/w_o$ ) of the T junction. This determines the bounded effective throughput range within which the flow condition can make an adjustment. A general rule is that increasing one or both of the ratio(s) would push the transition to happen at higher flow rates, thus operating with higher throughput. This is an important factor when considering the design of the geometry for different applications. Note that, we found that the transition boundary is only slightly influenced by the expansion angle  $A$  (for  $A = 8, 14$  and  $20$  degree that we have tested) and constriction channel length  $N$  (for  $N = 25, 50, 100 \mu m$  that we tested). The following results for encapsulation of HT-29 cells that are around  $13 - 14 \mu m$  in diameter are obtained on a T junction with  $A = 4^\circ$ ,  $N = 50 \mu m$ ,  $w_i = 30 \mu m$ ,  $w_o = 11 \mu m$  and  $h = 52 \mu m$ . In addition, we used a T junction with  $A = 4^\circ$ ,  $N = 250 \mu m$ ,  $w_i = 120 \mu m$ ,  $w_o = 55 \mu m$  and  $h = 180 \mu m$  for encapsulation of 10x genomics bead that are around  $70 \mu m$  in diameter.

## **Chapter 3. Deterministic single cell encapsulation based on Cell Triggered Splitting (CTS)**

### **3.3.3 Single cell encapsulation**

The observation of CTS is conducted under an inverted Nikon microscope (Eclipse TE 300) mounted with a high-speed camera (Phantom Miro M310). Longer encapsulation experiments are recorded under a Nikon microscope (Eclipse Ts2R) mounted with a uEye (IDS) camera. The single-cell suspension (in PBS) and fluorinated oil (QX200 DG Oil for Evagreen) are loaded in gastight glass syringes (Hamilton, 500 $\mu$ L) and injected into the microfluidics channels through a syringe pump (CETONI Nemesys), at a predefined flow combination until the end of the experiment. The applied aqueous flow rates range from 0.5 to 8  $\mu$ L/min, and the droplet generation oil flow rates from 3 to 50  $\mu$ L/min for the single cell experiments for CTS-1. For CTS-2, the shown experiment is conducted with  $Q_{water}$ ,  $Q_{oil1}$  and  $Q_{oil2}$  being 1, 4, and 7  $\mu$ L/min. The droplet size and cell size analysis are performed on the recorded videos using homemade ImageJ and Matlab scripts. The counting of the cell-loaded droplets is done manually.

### **3.3.4 Single bead encapsulation**

Next GEM Single Cell 5' Gel Beads from 10X genomics were diluted 20 times in DI water, then used as the aqueous phase with the above method.

### **3.3.5 Cell viability test**

After preparation of a single cell suspension, half of the suspension is kept at room temperature (Control group), and the rest is processed in the microfluidics chip at a throughput of 241Hz (for droplet generation) for 20 mins. At the end of the operation, the droplets floating on top of the oil in the collection Eppendorf were recovered and poured onto a super-hydrophobic film (Millipore Membrane filter, 1 $\mu$ m pore size), which absorbs the surfactant and the excessive oil for breaking the droplets. After 1 min, the aqueous phase was collected with a pipette (Experiment group). The cells from both the experiment and control groups were stained with Propidium Iodide (PI) and observed under a microscope to evaluate the membrane integrity. The HT-29 cells were modified to express the Green fluorescent protein (GFP) gene, thus showing green fluorescence. Cells expressing “only red” or “red plus green” fluorescence are considered with compromised membranes.

## **3.4 Lateral breakup/Central breakup competition**

The first CTS method “CTS-1” utilizes the competition between the lateral and central breakup as explained in chapter 2.

#### 3.4.1 Design and working principle

The geometry for “CTS-1” is almost the same as used in chapter 2. We only reduced the length of the outlet channel that has a width of  $w_o$  (smaller than a cell’s dimension) to avoid unnecessary cell squeezing damage (Fig.3.2)a. To enable the lateral breakup (LB), the same geometrical design rule of eq.2.2 needs to be fulfilled, which has a constraint on the aspect and width ratio ( $h/w_o$  and  $w_i/w_o$ ) of the T junction. More specifically, LB is enabled by setting a wide inlet channel that narrows into a smaller-width outlet channel, all having an aspect ratio greater than one.

Fig.3.2b shows the regime map on this modified geometry CTS-1. Similarly, LB that breaks the droplet inside the two arms of the outlet channel happens at a lower flow rate with a smaller mother droplet size (red dots), whereas the ‘Central Breakup’ regime (CB) that pinches the droplet from the middle occurs at a higher flow rate with longer droplets (blue dots). As explained in chapter2, at CB flow conditions, the capillary instability responsible for LB cannot develop till the LB breakup happens. The instability is suppressed by the enhanced pressure drop along the droplet and the fact that the droplets do not stay in the lateral channel long enough until shortcuted by CB. However, when the system is operated at a CB-close-to-LB regime (e.g., highlighted in Fig.3.2b), the LB breakup is close to breakup in time (Fig.2.5), and the system is very sensitive to any hydrodynamic perturbation. If a droplet that passes contains a cell whose diameter is slightly larger than the width of the narrow section ( $w_o$ ), the squeezing of the cell in that section enhances the lateral breakup instabilities. The presence of the cell retards the happening of the CB (Fig.3.2b). These effects cause the lateral breakup to re-occur automatically. An additional satellite droplet containing the cell is formed, together with two empty large droplets (Fig.3.2b). As the lateral droplet splitting is only triggered by the presence of a deformable particle such as a cell, *all* and *only* satellite droplets will contain single cells. Consequently, satellite droplets are a pure population of cell-loaded droplets. This is achieved automatically and passively by just flowing the mother droplets through the special T junction at a constant flow condition.

#### 3.4.2 Results

##### CTS with high efficacy and specificity

In this study, we use an outlet channel width ( $w_o$ ) of  $11\ \mu m$ , and HT-29 cells (average diameter of  $13.7\ \mu m$ ) to demonstrate the cell-triggered splitting. As all CB regimes that are close to the transition boundary are suitable for operation, there exist many working flow combinations with different throughputs on the same geometry. We first experimented with a mother droplet sorting rate of  $47\text{Hz}$  ( $Q_{water} = 0.5\ \mu L/min$ ). The single-cell triggering efficiency is defined as the success rate of satellite droplet generation upon the presence of a single cell in the mother droplet. For a total of 473 single cells, we obtained an overall triggering efficiency of 91.3%. The detailed analysis for different cell size categories shows that cells larger than  $w_o$  have achieved triggering efficiencies close to 100% (Fig.3.3a). This high triggering efficiency for

### Chapter 3. Deterministic single cell encapsulation based on Cell Triggered Splitting (CTS)

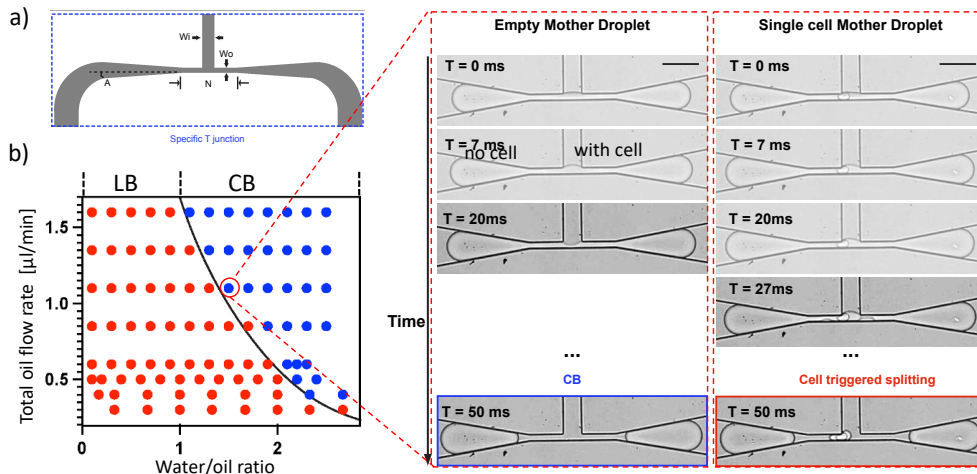


Figure 3.2 – **Design and working principle of the CTS-1.** a) The design parameters of CTS-1; b) Droplet breakup regime map for the lateral breakup (LB, red) and central breakup (CB, blue) on the CTS-1 geometry. Such a map can be established for each junction geometry for which lateral breakup can occur. The x-axis is the water/oil ratio in the droplet generator, mostly defining the mother droplet length; The y axis is the total oil flowrate (in  $\mu L/min$ ), including the droplet generation oil and a droplet spacing oil introduced into the system downstream to the droplet generator and upstream to the T junction. The insert shows at a CB-close-to-LB regime the splitting process of an empty droplet and a cell-loaded droplet, taken with a high-speed camera at a rate of 3000 FPS. Set time zero as the moment when the droplet rear interface fully entered the outlet channel, at  $T = 20ms$ , an empty droplet finishes breaking centrally (left); for a cell-loaded droplet, however, no sign of central breakup occurs at  $T = 20ms$ , due to the retardation of the cell at the junction; until  $T = 27ms$  the lateral breakup has happened, with a droplet interface splitting in one arm of the T junction, generating the satellite droplet around the junction area, encapsulating the cell automatically (right)

### 3.4. Lateral breakup/Central breakup competition

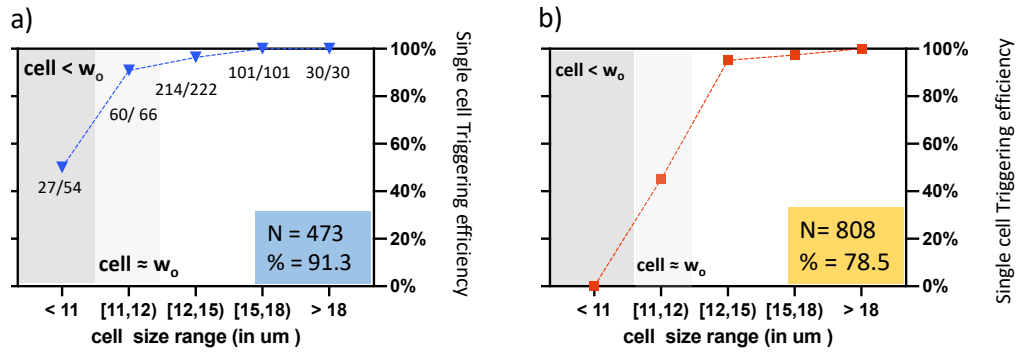


Figure 3.3 – **Single cell triggering efficiency at different cell size categories** The cell size range for each category is shown on the x-axis; the cell triggering efficiency for each category is shown on the y-axis. The total efficiency is obtained by dividing the total number of triggering cells by the total cell number. a) @ 47 Hz: single cell triggering efficiency for different droplet size categories is shown with blue triangles; ‘27/54’ means 54 cells are in this size category, out of which 27 have successfully triggered the satellite formation. The total number of cells characterized is 473; b) @ 241 Hz: single cell triggering efficiency for different droplet size categories is shown with orange squares; The total number of cells characterized is 808.

large cells remains true when a different flow combination with higher throughput- i.e., at a mother droplet sorting rate of 241 Hz ( $Q_{water} = 2\mu\text{L}/\text{min}$ ) is performed and was observed for a total of 808 cells (Fig.3.3b). While the triggering efficiency for cells smaller than or similar to the outlet channel width  $w_o$  ( $w_o = 11\mu\text{m}$ ) is not as sufficient as @ 47 Hz, the triggering efficiency for cells that are equal to or larger than  $12\mu\text{m}$  remains  $> 95\%$ . This indicates a highly selective triggering with a cutoff triggering (threshold) at around  $12\mu\text{m}$ , i.e., at a cell size slightly larger than  $w_o$ . Such knowledge can be used to design a chip for either full population encapsulation, i.e., redesigning of a  $w_o$  that is smaller than the full-size spectrum of the cell population, or a size-selective encapsulation, i.e., redesigning of a  $w_o$  that is only smaller than the size of target cells but similar to or larger than the rest of the cell population. At both throughput conditions, the obtained droplet size difference associated with cell occupancy is significant- over 12 times the difference in droplet volume between small satellite droplets and large empty droplets is observed. The satellite droplets have a good monodispersity, and their diameter is  $23 \pm 1.5\mu\text{m}$  @ 47 Hz and  $22 \pm 1\mu\text{m}$  @ 241 Hz (Fig.3.4a).

The specificity of the method, defined as the number of single-cell loaded satellites among the total population of satellite droplets, has been compared to the Poisson distribution under the same cell concentration ( $\lambda = 0.12$ ) in Fig.3.4b. The percentage of empty droplets is reduced from 89% to around 1%, while the percentage of droplets containing single cells rises from 11% to 94%. Empty satellite droplets rarely exist -satellites loaded with cells consist of  $> 98\%$  of the population. For a mother droplet containing two (doublet) or more cells (multiplet), and if the single cells are not adherent to each other, there is a high chance that only one cell is partitioned into one satellite (Fig.3.5). This self-correction function further reduces the ratio of doublets and multiplets in the satellite population compared to the initial mother droplet

### Chapter 3. Deterministic single cell encapsulation based on Cell Triggered Splitting (CTS)

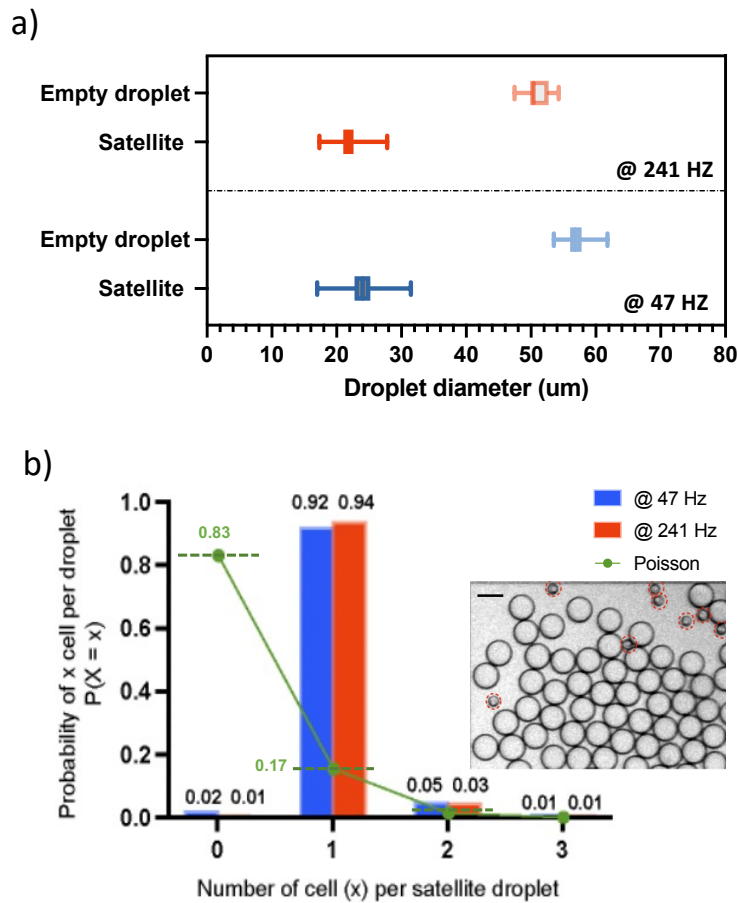


Figure 3.4 – a) The droplet size distribution @ 241Hz and @ 47Hz. The min and max values are shown as the whiskers, the 1st and 3rd quartiles are shown in the box, and the median is shown as the darker line inside the box. b) The observed ratio of droplets loaded with different numbers of cells is shown in bars (red and blue); the Poisson probability of a droplet to contain a certain number of cell numbers under the same cell density of  $\lambda = 0.12$  is shown with dots (green). Insert: bright field image obtained after the CTS before the sorting, scale bar =  $50 \mu m$ , satellite droplets are highlighted

### 3.4. Lateral breakup/Central breakup competition

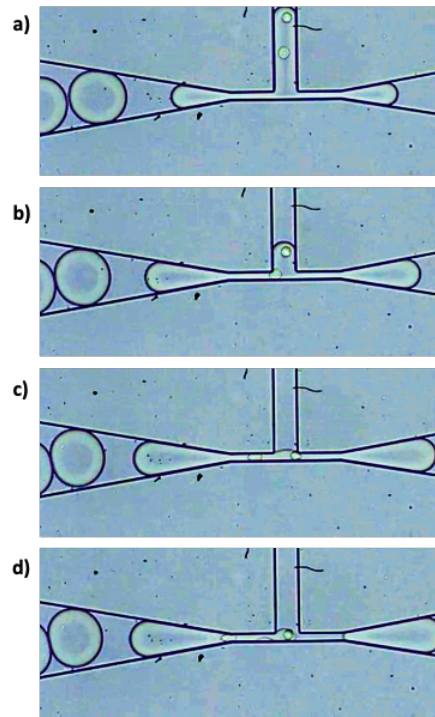


Figure 3.5 – The time sequence of droplet splitting when containing two cells

population. In our case, some doublets and multiplets result from adherent cells obtained during the cell preparation. These cells are partitioned into one satellite droplet as a single (large) particle. Note that for a given T junction geometry, as long as the fluid properties do not change, the working regimes (i.e., the operational flow conditions) are fixed and reproducible. Therefore, real-time flow tuning is avoided, which allows the system to start operating from the first cell entering the system until the whole sample is processed.

Remarkably, being a passive method without any detection/actuation limit, our method has shown efficient cell-triggered splitting at a mother droplet sorting rate up to 3100Hz ( $Q_{water} = 8\mu L/min$ ), giving 22.3 k cell loaded-droplets per minute (with  $\lambda = 0.12$  cells/droplet). An overall single-cell triggering efficiency of over 70% is demonstrated (including cell size population smaller than  $w_0$ ). Due to the low exposure time in the high-speed (11,000 FPS) video, we have difficulties in assessing the cell size (limited by the image quality), the triggering efficiency at different cell size ranges cannot be obtained. However, the 70 % overall triggering efficiency is close to the one we obtained for at 241 Hz (Fig.3.3b). We thus infer that a similar triggering threshold is playing a role. Such throughput has not been demonstrated by any other passive or active method so far.

## Chapter 3. Deterministic single cell encapsulation based on Cell Triggered Splitting (CTS)

### Passive sorting of small cell-loaded droplets

After the T junction splitting, the cell occupancy of the droplets is no more random but linked to the droplet size. The next step is to collect the smaller satellite droplets which contain the cells. Given the significant size difference, many existing sized-based sorting methods can be used. Here we use PFF (Pinch Flow Fractionation), where an oil flow pushes all droplets against a channel wall such that the smaller satellites align with the streamlines closer to the wall, whereas the larger droplets align with streamlines that are further away from the channel wall. A subsequent expansion geometry separates the two populations. The small ones flow into the bottom channel for collection, and the larger ones towards the middle channels for waste. In our demonstration, 89% of the satellites generated upstream went into the collection channel. The rest are misplaced into the waste channels due to occasional droplet traffic jams. We expect this to be avoided/improved with better geometry design. Remarkably, during 20 mins of operation at 241 Hz, over  $5 \times 10^5$  large droplets are generated, but there is not a single one misplaced into the collection channel, preserving a 100% purity of satellite droplets population for the final collection. Therefore, after the sorting step, we preserved a droplet population with over 98% cell loading efficiency, among which 92-94% contain single cells.

To confirm that the confinement of a cell in a channel slightly smaller than its dimension does not adversely affect the cell's viability, we conducted a cell membrane integrity test after operation at the throughput of 241 Hz. Cells are recollected from the created droplets from the outlet after going through the splitting and sorting geometries and are stained with Propidium Iodide (PI). The cell damage rate is only 3% higher than the one of the control experiment. Note that the preservation of the plasma membrane after microfluidics squeezing was also confirmed in other studies where cells were pushed through a constriction of half size at double the cell speed as compared to the present study [84, 85]. The collected satellite droplets are stable for transfer and storage. We observe no satellite droplet merging in the droplet collection reservoir during the 5 hours following their production.

### Single bead encapsulation

To demonstrate that this method applies to any deformable particle, we applied it to deterministically encapsulate deformable gel beads from 10X Genomics, which are currently widely used for single-cell RNA sequencing. Based on the simple working principle and design rule of the device presented in this study (SI section 1), we easily scaled up the geometry to accommodate gel beads with an average diameter of  $70 \mu m$ . The corresponding cell triggered splitting is shown in Fig.3.7 with a device with a lateral channel width  $w_o = 55 \mu m$ . Thanks to the monodisperse size distribution and homogeneous viscoelastic properties of beads, we reached 100 % triggering efficacy, with nearly 100% single bead droplet specificity (beads do not stick to each other). The created satellite droplets have a diameter of around  $90 \mu m$ , with a volume of  $V_{droplet} = 0.8nL$ .

### 3.4. Lateral breakup/Central breakup competition

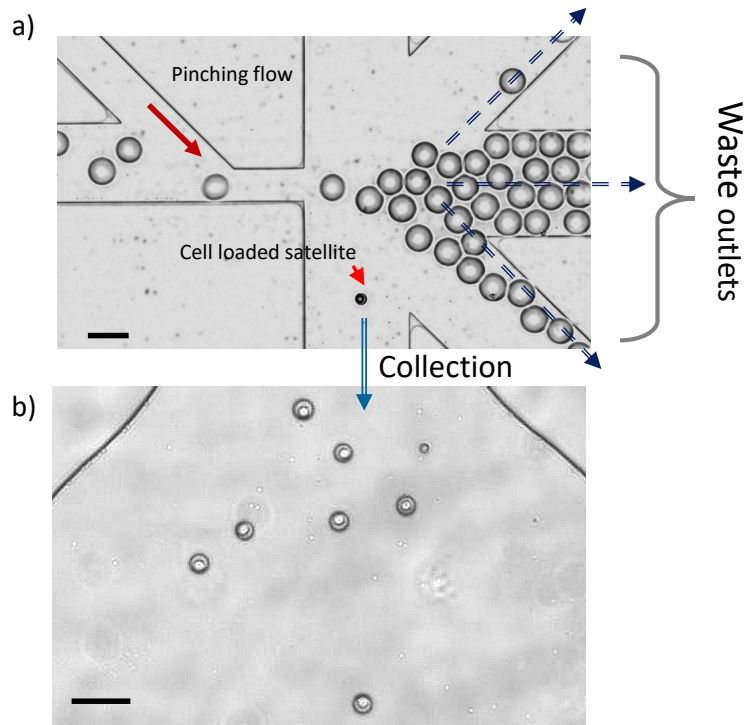


Figure 3.6 – **Passive size sorting using PFF.** a) Bright-field image at the sorting junction showing the different directions of the two types of droplets. The large empty droplets are distributed in the three central waste outlets. Cell-loaded small satellite droplets are directed towards the bottom collection channel; the Scale bar is  $75 \mu m$  b) Bright-field image at the entrance of an observation chamber downstream to the collection channel showing the cell-loaded small satellite droplets. Scale bar is  $75 \mu m$ .

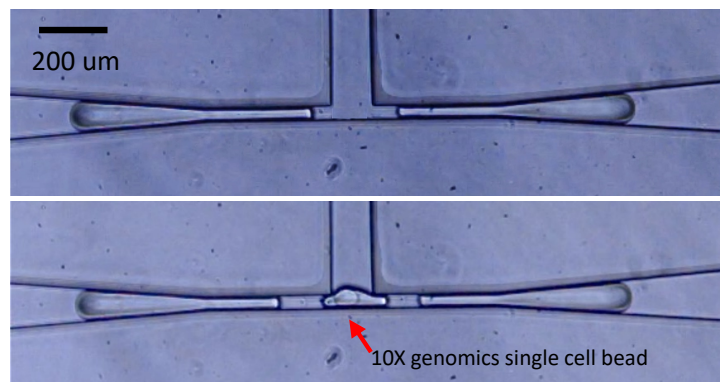


Figure 3.7 – **Lateral splitting induced by the presence of a hydrogel bead in the mother droplet** The easy scale-up and applicability to other deformable particles is demonstrated here using Next GEM Single Cell 5' Gel Beads from 10X Genomics, with a bead diameter  $D_b = 70 \mu m$ , lateral channel width  $w_o = 55 \mu m$ , at mother droplet sorting rate of 50 Hz. The resulting satellite diameter is  $D_s = 90 \mu m$ .

## Chapter 3. Deterministic single cell encapsulation based on Cell Triggered Splitting (CTS)

### 3.4.3 Discussion

In this section, we have shown the first cell-triggered splitting (CTS-1) method for deterministic single-cell encapsulation, based on the competition between the central breakup (CB) and the lateral breakup (LB) regimes discussed in Chapter 2. We demonstrated that the same principle works for both single cells and deformable particles and particles with different sizes, governed by the scaling law from Chapter 2. We found that nearly 100% of the cells larger than the lateral channel restriction ( $D > 12\mu\text{m}$ ) trigger the formation of the third smaller-sized droplets, among which more than 98% contain at least one cell, demonstrating the remarkable CTS sensitivity and selectivity. Because of the cell-triggering droplet formation mechanism, the cell occupancy of the smaller-sized droplets is always guaranteed –this is the intrinsic high specificity of this method. The CTS-1 method results in an object-loaded droplet of a not-so-large diameter compared to the encapsulated object. Although a smaller volume means a higher signal intensity and less dilutive destruction in the case of droplet merging, it also prevents single-cell incubation and/or longer time monitoring. CTS-1 is, therefore, more suited for instant screening and microfluidics manipulation of single cells (e.g., transport, merging, pairing, sorting, etc.). The remarkably-wide range of throughput possibilities is a great advantage for these applications. We demonstrated throughput from 47Hz to 3100 Hz, but we believe this is not yet the lower or higher limit of this method. Note that the ultra-high throughput for *label-free* droplet sorting (i.e., at a rate of 3100 Hz) is not yet demonstrated elsewhere, which is attributed to the extreme simplicity and sensitivity of the working principle. What's more, without the synchronization effect, CTS-1 can operate robustly for a long duration.

## 3.5 Step breakup/Central breakup competition

In this section, we will report the second CTS method “CTS-2”. We have shown that the CTS-1 method results in single cell-loaded droplets with a similar size to the cell itself (1.6 times in diameter). While it is particularly suited to construct biological assays that are adversely affected by dilution, there is also a need to generate large-size single-cell-containing droplets to enable, for example, single-cell incubation or single-cell experiments requiring long-term monitoring. Hence, we seek to develop a new geometry for CTS, which is the CTS-2.

### 3.5.1 Design and working principle

For CTS-2, we also used the competition between the central breakup and a surface tension-driven breakup. However, here the surface tension-driven breakup is in the format of “Step breakup” (SB): the droplet interface breaking always happens at a geometrical step where the narrow lateral section is expanded into a reservoir. In CTS-1 geometry, near the transition boundary the droplet breakup location is often very close to the junction, leading to small single-cell droplets. With CTS-2, we aimed to dictate where the droplet breakup could happen, by introducing a drastic change of channel dimension, i.e, the step. Fig.3.8a shows the CTS-2

### 3.5. Step breakup/Central breakup competition

---

geometry. It starts with a T junction described before, which implements the central breakup regime (CB). Both narrow sections are connected to a large chamber, which implements SB. Here, the LB we introduced in CTS-1 is much less important than SB and can be neglected. To design the CTS working principle, it is necessary to understand the process of SB: When a droplet is passing the junction, the fronts of the droplet that start entering the reservoirs would form growing bulbs with decreasing mean curvatures. Once the bulbs are large enough, the necking of the droplet interface happens which forms a thread at the steps. This process is similar to traditional step emulsification [69]. Around the threads, the pressure of the continuous phase is smaller than that in the reservoir ( $P_{th} < P_R$ ), creating a backflow into the thread that drives its thinning until the breakup of the interface happens. Normally, the SB is followed by a CB once the droplet rear interface reaches the junction and is subjected to the pinching from the continuous phase (Fig.3.8b).

In such microfluidic junctions, cells can be used to trigger the droplet-splitting phenomenon, but this requires adjusting the relative strengths of CB and SB by controlling the flow conditions. When a droplet has fully entered the junction but the bulb still has not grown enough to start the necking process, only CB happens (Fig.3.8c); this could occur with a relatively short droplet and at higher droplet speed. There are flow conditions where CB occurs, and the necking for SB has also started but does not have time to develop fully; thus, there is still only CB that occurs, but SB is already not far. In this case, the presence of a cell inside the droplet can be used to perturb the splitting condition. If a cell is squeezed in one of the outlet channels, the incoming flow is reduced due to the increased resistance,  $P_{th}$  drops and accelerates the thinning of the thread in this outlet. In the other branch, the flow is increased due to flow conservation ( $P_{th}$  high); the thinning is therefore avoided. Eventually, SB is induced at the step of the fluidic branch in which the cell is present, and CB will happen as usual that is not influenced by the cell. The co-occurrence of both SB and CB leads to the creation of a third droplet containing the cell (Fig.3.8d). This droplet is significantly smaller than the two (empty) droplets generated at the same time, which are mainly constituted by the volume of the bulbs.

## Chapter 3. Deterministic single cell encapsulation based on Cell Triggered Splitting (CTS)

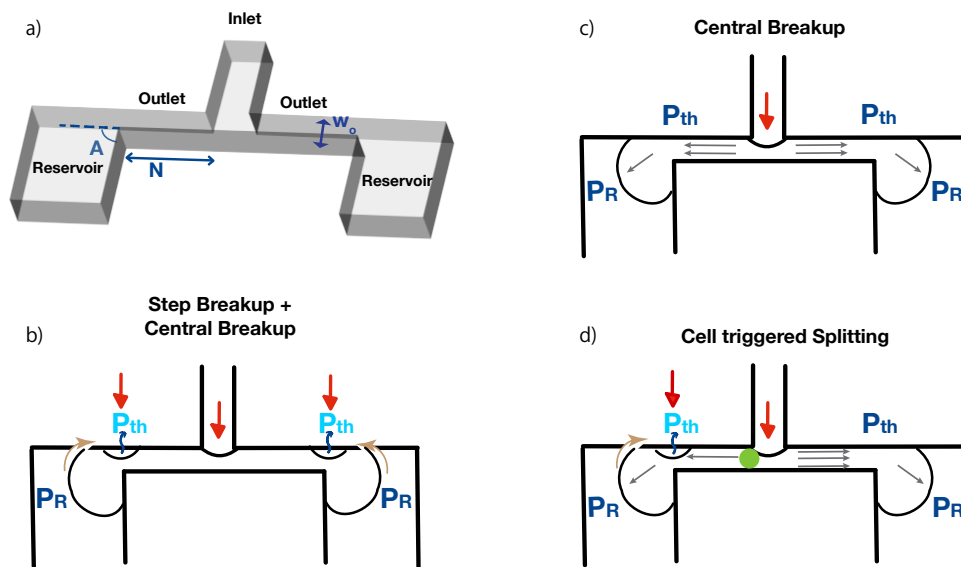


Figure 3.8 – **Working principle of the new CTS geometry.** a) Schematic and parameters of the CTS junction; b)-d) Schematics of different breakup regimes on the CTS junction; red arrows indicate the final droplet breakup locations;  $P_{th}$  and  $P_R$  represent the pressure of the continuous phase around the thread region and in the reservoir, respectively; the light and dark blue colors indicate the relative strength of the two parameters, with the light blue indicating a lower value than the dark blue. b) Step breakup (SB) and central breakup (CB) of a droplet in the CTS junction; brown arrows show the backflow of the continuous phase; c) CB-only breakup of a droplet in the CTS junction. The double grey arrows within the lateral outlet channels indicate a strong flow compensating  $P_{th}$ , eliminating the effect of “necking” at the step. d) Cell-triggered breakup of a droplet in the CTS junction. The green circle presents the cell; one and three grey arrows show the decreased and increased flow within the two outlet channels.

### 3.5.2 Results

#### Working regimes in different geometries

As the control of the relative strength of CB and SB is the key to the successful CTS operation of this type of fluidic junction, in this section, we characterized the different regimes with respect to various flow conditions for geometries with diverse parameters. Water-in-oil droplets of different lengths were obtained by varying the water/oil ratio at a microfluidic “flow focusing” junction while the speed of the obtained droplets was adjusted by injecting oil from another inlet at chosen flow rates.

During experiments, 4 droplet breakup regimes were observed:

- **Step emulsification:** Each mother droplet entering the junction results in multiple (more than one in each arm) breakups at the steps with the SB mechanism. Finally, the

### 3.5. Step breakup/Central breakup competition

---

last part of the mother droplet is divided in two by the CB mechanism. This condition is shown in Fig.3.9a) i. and is represented by squares in Fig.3.9b)-e).

- **Step and central breakup:** Each mother droplet entering the junction results in just 4 droplets, two generated at each step of the outlet branch with the SB mechanism and two generated with the CB mechanism. The SB and the CB breakup happen (almost) at the same time. This condition is shown in Fig.3.9a) ii. and is represented by circles in Fig.3.9b)-e). Occasionally, due to flow perturbation, only one SB but not two happens with the CB, creating 3 droplets; we categorized it into the same regime here.
- **Cell-triggered breakup:** Without a cell, each empty mother droplet is divided into 2 droplets by the CB mechanism. The SB mechanism (i.e., necking) starts but does not have time to fully develop, and breakup never occurs for empty mother droplets unless a cell is present in the mother droplet. This is the condition required for the CTS mechanism to occur, and when a cell is present in the mother droplet, a small droplet containing the cell is generated in addition to 2 large empty droplets. This condition is shown in Fig.3.9a) iii. and is represented by blue diamonds in Fig.3.9b)-e).
- **Central breakup only:** Each mother droplet is divided into 2 droplets by the CB mechanism. SB never occurs, even with the presence of a cell. This condition is shown in Fig.3.9a) iv. and is represented by crosses in Fig.3.9b)-e).

In Fig.3.9b-e, we mapped the different regimes versus the varying droplet generation water-to-oil flow rates ratios (y-axis) and the total flow rates (x-axis); each figure represents one geometry where its outlet length  $N$  (in  $\mu m$ ) and the angle at the output of the outlet channel  $A$  (in degree) (see Fig.3.8a) is shown as the title, and other geometrical parameters are constant. It is shown that in all studied geometries, the breakup regimes transition from “Step emulsification” to “Step and central breakup” and to “Central breakup only” with increasing total flow rates for any chosen value of the flow rate ratio for droplet creation. The former (total flow rates) is proportional to the droplet speed and the latter (water-to-oil ratio) roughly dictates the droplet size, with a higher ratio indicating a larger droplet. The working regime “Cell-triggered breakup” occurs only for mother droplets created with a water-to-oil ratio lower or equal to 1, and for a small range of droplet speeds. Moreover, some microfluidic junction geometries do not allow this regime to occur (i.e. N75A90 in Fig.3.9c).

The length  $N$  of the outlet channel potentially dictates the size of the cell-loaded droplets. It is therefore interesting to understand if we can choose the  $N$  arbitrarily or if there is a constraint. Fig.3.9b and 3.9c show the effect of increasing  $N$  from 50 to 75  $\mu m$ : without changing other geometrical parameters, this eradicates the “cell-triggered breakup” regime. The reason is that for a given mother droplet size an increased  $N$  reduces the droplet bulb sizes in the reservoirs preventing the necking condition and thus weakening SB. Interestingly, for  $N = 75 \mu m$ , if we increase the angle  $A$  from 90 to 105 degrees (Figure 3.9d) (Figure 3.9e), the “cell-triggered breakup” regime is re-established, signifying that a larger angle compensates for an increased outlet length. We understood this by realizing that as a droplet progresses in the junction, a

### Chapter 3. Deterministic single cell encapsulation based on Cell Triggered Splitting (CTS)

larger  $A$  will result in the bulb curvature decreasing faster for the same bulb volume in the reservoir; thus SB is strengthened again. This gives us a tool to regulate the outlet length  $N$  and thereof the droplet size we can obtain from this technique. What's more, by increasing further the  $A$  from 105 degrees to 120 degrees, the “cell-triggered breakup” regime even becomes more abundant. This is beneficial and should be considered during chip design.

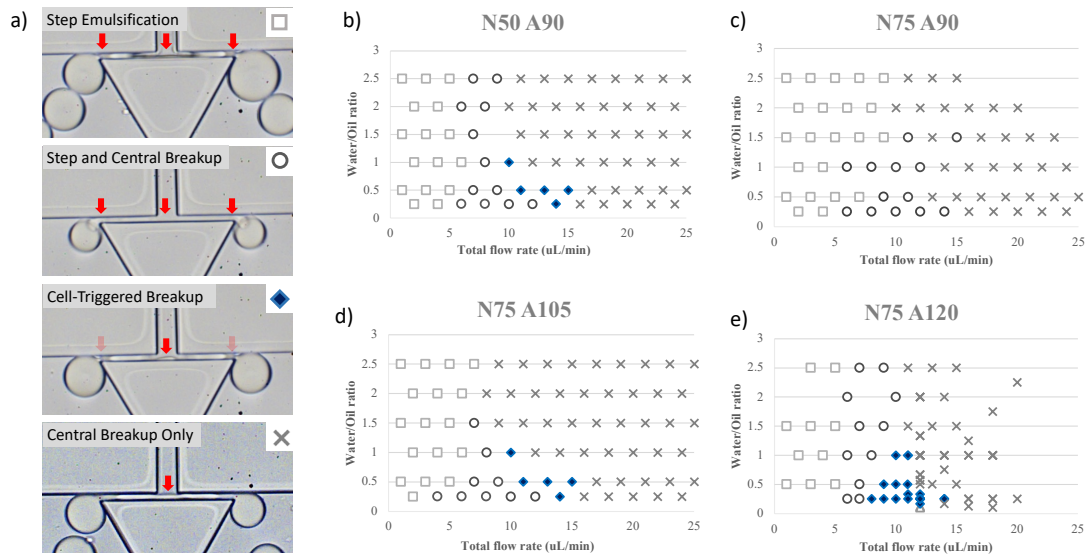


Figure 3.9 – **Different regimes on four geometries.** a) Bright field images showing the different splitting regimes summarized in the regime maps of b-e). Red arrows indicate the final droplet breakup locations; faint red arrows indicate the locations of the (halfway) “necking” of the droplet interface which eventually does not turn into a “breakup” of the interface. The images are taken on geometry N75A120. The working regime is the “cell-triggered breakup” regime represented by a blue solid diamond. b-d) Regime maps for geometry N50A90, N75A90, N75A105, and N75A120, with respect to different  $Q_{Water}/Q_{Oil}$  ratios (y-axis) and different total flow rates with a unit of  $\mu L/min$  (x-axis). All these geometries have channel height  $H = 75\mu m$  and outlet width  $w_o = 11\mu m$ . The working regimes are highlighted in blue color while the other regimes are in grey.

#### CTS-2 performance

Being an asynchronous method, the working condition of CTS-2 corresponding to the Cell-triggered breakup regime can be empirically decided beforehand using the maps presented in Fig.3.9. Once set, the cell-triggered splitting mechanism (CTS) will work automatically. Fig.3.10 a-c) and d-f) show the breakup of an empty and a cell-containing mother droplet, where the difference of the droplet interface at the neck is highlighted by the red arrows. The presence of a cell induces a new droplet formation containing that cell as expected. In geometry N50A90, the cell-loaded droplet has a diameter of  $28\mu m$ . This value is increased to  $40\mu m$  in geometry H75A120 (droplet “1”), corresponding to a volume 30 times larger than the one of the cell. The

### 3.5. Step breakup/Central breakup competition

size of both empty droplets, i.e., droplets “2” and “3” in Fig.3.10 f and c are 59 and 64  $\mu\text{m}$  in diameter respectively, which is significantly larger than the one of droplet “1”. This is critical for passive size sorting downstream. In this example, the splitting of mother droplets at the junction is performed at a rate of 250 Hz.

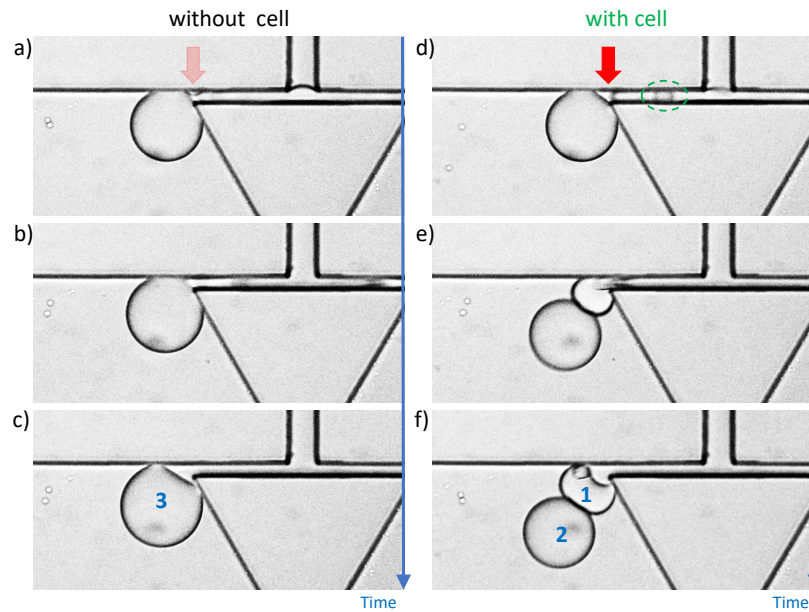


Figure 3.10 – **Proof of concept of CTS on geometry N75A120.** a-f). Bright-field image showing the time course of two droplet splitting events (a-c and d-f) for the same flow condition on the same geometry. The faint and solid red arrows highlight the “necking” and the “breaking” of the droplet interface respectively.

Fig. 3.11a characterizes the single-cell triggering efficiency on geometry N75A120. For a total of 269 single cells, 80% have induced CTS (pink bars), and 12% did not induce any breakup, which was observed more often for smaller cells (purple bars). When the cell is too big, it induces an early breakup not at the step but inside the lateral outlet channel at a distance close to the cell, creating a satellite droplet of a similar size to the cell itself (grey bars). This phenomenon is like the LB in CTS-1; it occurs for 8% of the cell population, correlated to the natural occurrence of overly large cells within a cell population. When cells are large enough to trigger a new droplet generation, the generated cell-containing droplets, which sum up to 88% of the total droplets, are always smaller than the empty droplets and can be efficiently sorted out downstream. Fig. 3.11b compares the satellite droplet population obtained in this experiment with a population obtained from random encapsulation under the same cell concentration of  $\lambda = 0.2$  cell/droplet. As only the presence of a cell would induce the creation of a satellite droplet, the obtained cell loading efficiency is intrinsically high: 96%. With this method, the overly large cells sometimes induce empty droplets of a size similar to the cell-loaded droplets during the early breakups. Nonetheless, the empty satellites represent approximately 4% of the total satellite population, which is significantly lower compared to

### Chapter 3. Deterministic single cell encapsulation based on Cell Triggered Splitting (CTS)

the percentage of empty droplets resulting from the Poisson distribution. In terms of droplets containing two or more cells (multiplets), their ratio can be further reduced by decreasing the initial cell concentration.

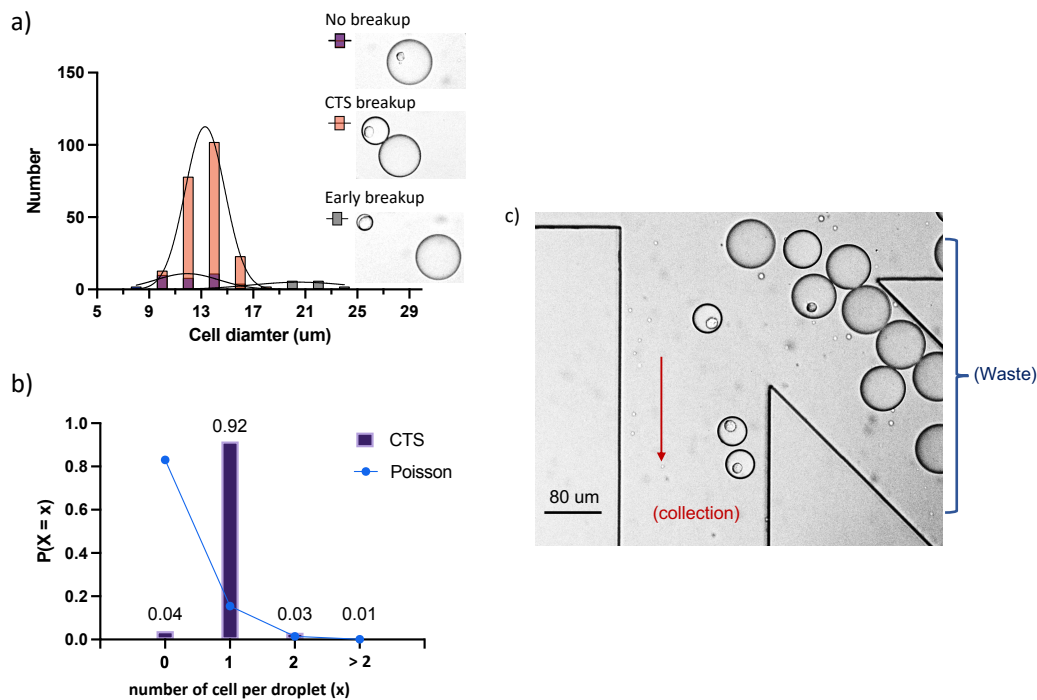


Figure 3.11 – **Performance of CTS on geometry N75A120.** a) Frequency distribution of three types of droplet splitting outcome- No breakup (purple), CTS-2 breakup (pink), and early breakup (grey)- with respect to different cell size categories (represented with cell diameter in  $\mu m$ ). The insert bright-field images explain the three splitting outcomes; The value of each bar represents the event count for each type of outcome (distinguished by colors) within each cell diameter category (bin width =  $2\mu m$ ). The black curves indicate the fitted Gaussian distribution for each splitting outcome, whose center of distribution is shifted from small to large cell size for No breakup, CTS-2 breakup, and early breakup. b) The probability of having  $x$  cells in one droplet within the CTS-generated satellite droplet population (“CTS”, purple bar) and within a random encapsulation-generated droplet population (“Poisson”, blue dots). For CTS population, the value of the probability (in ratio) is indicated on top of each bar. c) A bright field image showing the sorting of the droplets, including cell-loaded satellite droplets and large droplets

We used Pinched Flow Fractionation (PFF) to demonstrate the sorting of cell-loaded satellite droplets (Fig.3.11c). In fact, while cells usually randomly pick up either side of the T-junction, the sorting works best when the triggered droplets always leave the T-junction from one side which is the lower branch that guides the droplet to arrive at the opposite wall of the pinching flow (see the position of the triggered droplets in Fig.3.1c). Therefore, we made the lower T-junction branch  $2\mu m$  shorter than the upper one to create a preferential flow. We indeed

observed most of the cells left from the lower branch and so thus their triggered droplets. With that, we observed very efficient sorting. Almost no triggered cell-containing droplets are misplaced in the waste outlets; no large (empty) droplets end up in the collection channel. The selectivity of the droplets gained in the cell-triggered splitting step is preserved, i.e., we obtain 96% of cell-loaded droplets in the collection outlet.

### 3.5.3 Discussion

In this section we have shown a different microfluidics geometry for CTS with a different triggering mechanism, resulting in larger cell-loaded droplets consisting of 30 times the volume of the cell. The high triggering efficiency is preserved, but the generated cell-loaded droplets have a less good size monodispersity due to the presence of early breakup. The high single-cell specificity is slightly worsened also due to the early breakup potential.

Like the CTS-1 geometry, we expect the CTS-2 geometry to be also applicable to other deformable particles, for example, functionalized beads. A major difference, however, is that with the new geometry and the new working regime, the CTS operation is limited to a specific range in the regime map and does not allow for the use of a wide range of flow combinations, leading to limited options of throughput (250Hz in the example presented in this section). However, there is flexibility in controlling the size of the single-cell loaded droplet. As the parameters of the outlet channel geometry including  $N$ ,  $w_o$ , and  $H$  dictate the final size of the cell-loaded droplets, the droplet size could be modulated by varying these parameters to adapt to different applications. Of course, new experiments are required to empirically determine the working regimes each time the geometry is changed, and it is not guaranteed that all geometry will have the working regimes (e.g., N75A90 is a negative example). In this work, we demonstrate the influence of  $N$  and  $A$  on the occurrence of the CTS-2 working regime and on the resultant size of cell-loaded droplets. It would be of great interest to develop a geometric design rule to achieve control of the cell-loaded droplet size via geometry change without performing new experiments.

## 3.6 Discussion

In this chapter, we proposed the CTS strategy for performing deterministic single-cell encapsulation into droplets. It consists of two steps: the first step (critical) is the cell-triggered droplet splitting, which transforms the droplets generated by random encapsulation into large empty droplets and small cell-loaded droplets. The second step (less critical) is then to apply a size-based sorting for collecting the cell-loaded droplets. This CTS strategy relies on the performance of the cell-triggered splitting.

### 3.6.1 Other object-triggered effect

Historically there is another mechanism to realize object-triggered droplet generation, which uses a jetting mode for which the liquid thread ruptures into dispersed droplets upon perturbation from an object that has a larger radius than the radius of the cylindrical jet [86, 87, 88, 89]. As the larger object blocks the inflow of the jetting phase downstream to the object, a neck is formed and the interface is broken. However, the resultant droplets are small, with a thin film of the jetting phase around the objects. This method has been demonstrated with spherical particles, droplets, or bubbles (to trigger the generation of a droplet) but not with cells. If we want to use this mechanism for cells, maintaining the jet stability and keeping its radius below that of a cell is the major challenge. In our case, the liquid thread is maintained by the channel geometry, and only the width dimension is smaller than the cells (1D instead of 3D constraint) for the triggering effect. Cell-triggered splitting happens due to a capillary instability we set through special types of geometries and is enabled by priming the system with a favorable (i.e., close-to-transition) flow condition. In this condition, a cell enhances the instability and leads to the breaking of the interface. Notably, the working condition required in this method is easy to achieve and maintain which is essential for the method's robustness.

### 3.6.2 Cell triggered splitting without T junction

While a T junction is used in both CTS-1 and CTS-2, which enables the competition between a central breakup and a particular type of surface tension-driven breakup (i.e., LB for CTS-1, and SB for CTS-2), the necessity of the T junction becomes the next question. That is to say, would the straight channel geometry possessing a transition from LB to non-breakup without CB (Chapter 2) be enough for the CTS effect? We tested it on the straight channel geometry shown in Fig.2.7a (C). Compared to (L), we reduce the length of the narrow section to  $100\mu\text{m}$  to decrease the resistance and ease the potential clogging and harm to the cell. Fig.3.12 shows the non-breakup and breakup phenomena on this geometry. The switching can be mediated by switching the flow condition actively (a) or by staying at the same flow condition but passively changing the droplet content (b). In (b) the delayed effect caused by the cell can be seen, which indicates that the triggering mechanism might be the cell retardation effect that allows a longer developmental time of the capillary instability. This investigation shows that the presence of the T junction and the central breakup is not necessary for the occurrence of cell-triggered splitting. A CTS can be as well achieved via the competition between non-breakup and (lateral) breakup. However, we do notice that on the T junction very high throughput can be achieved (3100 Hz), whereas on the straight channel the triggering by the cell seems to be already less efficient at a throughput of around 3 Hz. The different transition laws (shown in Chapter 2) and the stagnation zone at the bifurcate junction of the T-junction might explain the difference.

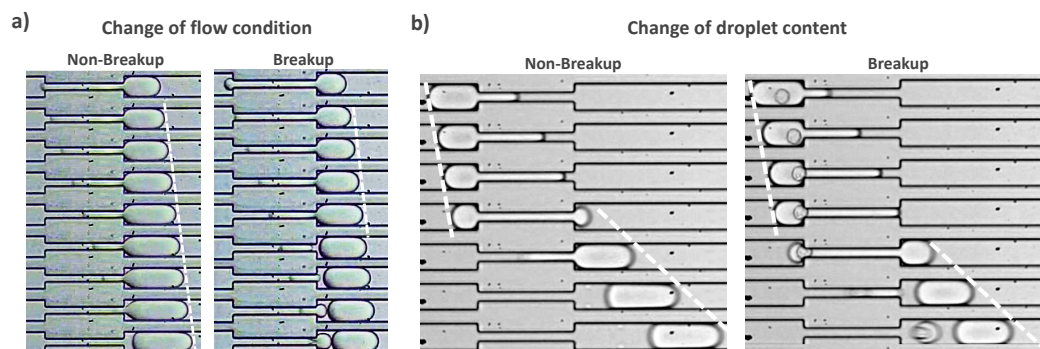


Figure 3.12 – **Droplet breakup results on straight channel geometry.** This geometry named “30-12-37-C” has a wider and narrower width as  $30\ \mu\text{m}$  and  $12\ \mu\text{m}$ , and has a height of  $37\ \mu\text{m}$ . Frame-by-frame bright field images taken at 600 FPS. a) Droplet breakup and non-breakup by changing the flow condition; in the breakup case the droplet has a slightly shorter length and a slower speed; b) Droplet breakup and non-breakup by changing the droplet content, i.e., with or without a cell. The flow condition for both cases is the same.

### 3.6.3 CTS as a real solution to Poisson Limit

The Poisson limit has been a long-standing issue in the field of droplet microfluidics. Currently, to bypass this limit people use active sorting to pick cell-loaded droplets from the empty droplets. The extra expenses and hardware/software complexity coming from the detection, decision-making, synchronization, and actuation indicate that this is rather a forced workaround resort than a real solution to this issue. Currently, there are different *passive* strategies to overcome Poisson distribution during single-cell encapsulation. The most studied strategy is to use cell ordering to match the droplet generation frequency. Here, with the operation limited to very specific cell concentrations (high) and flow rates (high), the synchronization is critical and demanding. Even when the cell ordering *and* the synchronization works well (which is usually not the case as compared to particles), the outcome is an increased ratio of cell-loaded droplets and not a deterministic result. Another strategy is to play with the droplet size and then apply size-based sorting. One method is to perform cascade splitting of droplets into smaller volumes until one size is more likely to have a cell[49]; Another method is to operate droplet generation in specific regimes such that the inclusion of a cell decrease or increase the droplet size compared to the empty ones[90]. Here, the first method is not deterministic, and the second one creates a size contrast rather small that is almost impossible to function properly in real applications. Due to these reasons, the above solutions also cannot be considered a real solution to the Poisson limit. In our case, we belong to the category of playing with the droplet size. However, due to the cell-triggering droplet formation mechanism, the cell occupancy of the smaller-sized droplets is always guaranteed – making it a deterministic solution. Also, the resultant droplet size contrast is significant and guaranteed, making it easy for downstream sorting. Compared to the first category of cell ordering, which requires synchronous operation and impairs the robustness and easiness to

### **Chapter 3. Deterministic single cell encapsulation based on Cell Triggered Splitting (CTS)**

---

use, the CTS method is completely asynchronous. This means without real-time tuning of the flow rates, one just drives the fluids through the chip with a “plug-and-play” operation, and a wide range of throughput can be freely adopted and maintained for any duration of the operation. In this regard, the CTS as a passive, deterministic, and asynchronous method could be a versatile and practical solution to the difficult problem of the Poisson limit.

#### **3.7 Conclusion and outlook**

In this study, we introduced a cell-triggered splitting method (CTS) as a solution to the Poisson limit during single-cell encapsulation in droplets. The physical basics of this method are from chapter 2. We introduced and characterized two variations of the CTS method. While both methods are deterministic, passive, and asynchronous (as the common properties of CTS), CTS-1 has a broad throughput range, high droplet size monodispersity, and a smaller size for the cell-loaded droplets; CTS-2 has a limited working range (around 200 Hz), but the droplet size is tunable and is, in general, more than 25 times the volume of the encapsulated cell volume, allowing for applications requiring cell incubation. The high purity of single-cell droplets created by CTS enables the deterministic construction of multi-cellular/ multi-cell-bead droplets, a need that is currently of growing interest but is still unmet.

## 4 Single cell encapsulation based on Single Cell Differentiated Trajectory (SCDT)

While single-cell droplets can be generated efficiently with CTS methods, there are limitations that we want to improve. First, the two-step approach undermines the overall efficiency as the two steps, i.e., the creation of size difference and the passive sorting based on the size difference, each has a certain success rate, and both need to be high to have a robust overall performance; In addition, the separation of two-cell or multiple-cell-containing droplets from single-cell-containing droplets is not possible with the CTS methods. In this chapter, we present a new concept, “Single Cell-Differentiated Trajectory” (SCDT) for the generation of single-cell loaded droplets based on the trajectory difference among empty mother droplets, single-cell loaded droplets, and multiple-cell loaded droplets.

### 4.1 Introduction

In this chapter, we will introduce a single-cell droplet acquisition method with direct droplet sorting. While passive sorting of droplets has been widely studied and has been demonstrated with droplet properties that include droplet size (the most studied), droplet viscosity/rigidity, droplet density, droplet surface tension, etc., to date, using droplet content for passive sorting is rare. In some studies, droplets with different cell densities varying from low, medium, to high can be separated from each other using external forces like acoustic force, magnetic forces, etc. [34, 91]. However, even the “low density” means more than 20 cells in each droplet. A droplet sorting based on the *single cell* content, i.e., the ability to distinguish among one cell, two cells, or more cell content, has not been reported so far. In the following, we will present a simple hydrodynamic mechanism where the presence of a single cell can make a difference in droplet trajectories; thus, droplet content-based sorting at the single-cell resolution can be achieved automatically in a passive manner. This principle is first realized on the CTS-2 geometry (chapter3) and is later extended to a generalized condition/geometry.

## **4.2 Working Principle**

In their study, Haner et al. [52] flow capsules of different viscosity through a junction that is connected to a large reservoir. At the junction, the incoming flow deforms the capsules (Fig. 4.1a, blue dotted arrows), where a stiffer capsule is deformed less and could travel in its original trajectory (green line) a bit longer before relaxing into the reservoir. Finally, in the reservoir, it ends up at a distance further away from the central line (red) compared to its softer counterpart ( $L_2 > L_1$ ). This study hints that the *deformation* and *relaxation* processes can be effectively used to create different trajectories of deformable objects (capsules, particles, droplets, etc.).

We first discovered in the CTS-2 geometry that the presence of a single cell could influence enough the *deformation* and *relaxation* status of the carrying droplets for their sorting. As shown in Fig.4.1b, the CTS-2 geometry is used in the flow regime where step and central breakup always happen, which generate three droplets including a small one from the volume of one branch (see “Step and central breakup” regime in Fig.3.9). As cells in the mother droplets will always be captured within the small droplets, our target droplets would be these droplets that inherited the cell occupancy of their mother droplets that might be empty or have one cell or multiple cells. When each of these target droplets comes free of the confinement of the outlet channel, its rear cap is deformed by the axial force from the narrow section. If a cell is present in the droplet, it occupies the droplet’s rear cap thus helping it resist this deformation (Fig.4.1b). Like in the above example, the less deformed cell-loaded droplet travels a longer distance along the axial direction compared to a more deformed empty droplet, resulting in trajectory separation in the large reservoir ( $L_2 > L_1$ , Fig.4.1b). In CTS-2 geometry, all droplets are carried to a straight gathering channel connected to a large chamber where the divergent flow profile further amplifies the initial trajectory difference leading to final droplet separation (See Fig.4.4a). In a simplified geometry which we will present later, to use this initial trajectory difference, we simply put a channel wall structure in between the two trajectories to guide the two types of droplets into different channels for separation.

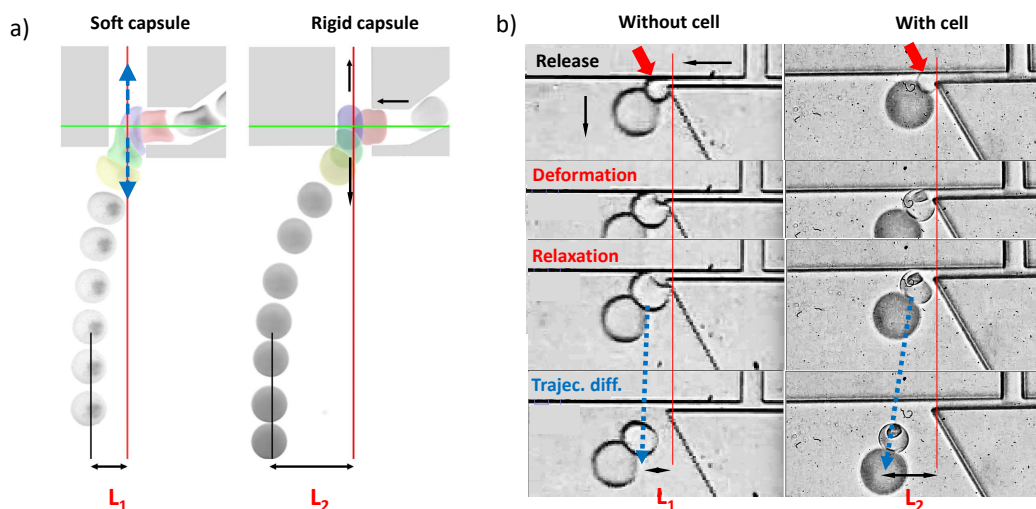


Figure 4.1 – **Working principle of Single Cell Differentiated trajectory (SCDT)**. (A) Trajectory difference between a soft capsule and a rigid capsule due to different degrees of deformation. The blue dotted arrows show the direction of the extensional deformation, and the black solid arrows show the flow direction, and both are the same in the two cases. The soft capsule (left) is less polymerized than its rigid counterpart (right), shown with the transparent color. The red line indicates the center of the reservoir, the green line indicates the center of the inlet channel. Adapted from [52]); b. Trajectory difference between an empty droplet and a cell loaded droplet at different time points under the same flow condition. The black arrows indicate the flow directions. At each panel, the two droplets have the same relative time stamps. The “deformation” panel illustrates the immediate droplet shapes right after the droplets are released from the lateral channel; The “relaxation” panel shows the moment when the droplet with the cell is completely detached from the walls, at which the empty droplet is still attaching the walls. The total “detaching” time is  $0.4\text{ms}$  and  $0.7\text{ms}$  respectively. The video is taken at 10,000 FPS. Here, the CTS-2 geometry is slightly modified to have different lengths over the two lateral channels ( $2\ \mu\text{m}$  difference), such that in the “Step and central breakup” flow regime (Fig.3.9) only one target droplet is generated due to the preferential flow into the side that is with lower resistance. It generates the target droplets (one per droplet breakup event) that are empty when the mother droplets are empty or contain the single cell(s) if the mother droplets have cells. The large empty droplets will always be directed towards the waste outlets and thus can be ignored here.

## 4.3 Results

### 4.3.1 Distinguishing singlets, doublets, and multiplets

We discovered that the travel trajectory of the target droplets within the reservoir could deviate more or less dependent on the number of cells inside the droplet. If we compare target droplets containing zero, single, two, or three cells, their distance-to-wall (D) in the straight gathering channel (green arrows in Fig.4.2) is systematically decreased with an increasing

## Chapter 4. Single cell encapsulation based on Single Cell Differentiated Trajectory (SCDT)

number of cells they contain (Fig.4.2). Each time by increasing one cell number, the target droplet deviates around  $10\mu m$  away from the junction (i.e., increased  $D$ ), quantified in Fig.4.2b as the column values. If we characterize only the droplets containing one cell, we notice that the cell size also influences the trajectory (Fig.4.2c). Roughly speaking, a larger cell size leads to a more prominent trajectory deviation for obvious reasons. As the trend is not strictly linear, it is possible that other properties of a cell, for example, rigidity, also influence the final droplet trajectory. Note that such sensitivity at the single-cell level indicates that potentially not only can cell-containing droplets be distinguished from the empty droplets- as currently achieved with active sorting or passive sorting (CTS, for example)- the single-cell droplet can also be separated from the doublets and multipllets, solving a currently non-addressed but commonly encountered issue in the field of single cell analysis.

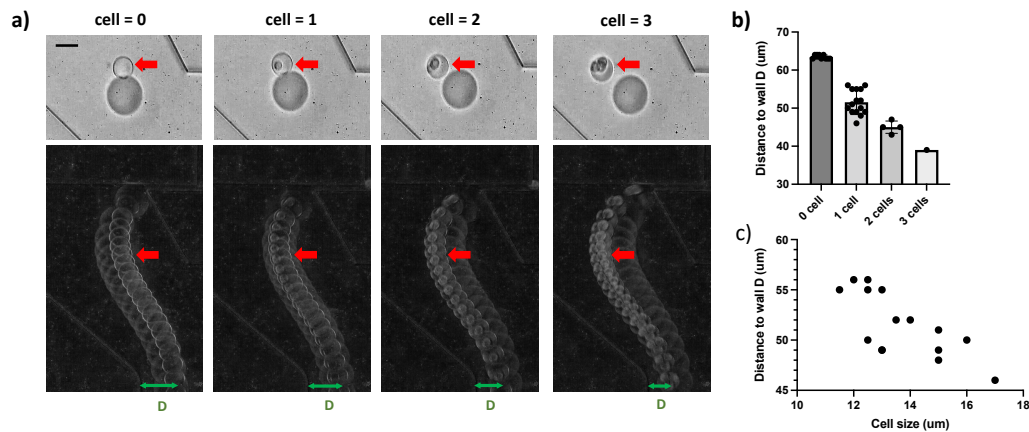


Figure 4.2 – **Influence of the cell number on the trajectory.** a) Upper panel: bright field images of the target droplets containing 0, 1, 2, and 3 cells (red arrows); note the relative distance between the target droplet and the empty large droplet whose trajectory keeps the same; scale bar =  $40\mu m$ . Lower panel: computed trajectories for each target droplet (pointed by red arrows) after being released from the lateral channel (each trajectory is from a single event); computed from the standard deviation of the grey value in the captured video; the green arrow indicates the distance from a target droplet center to the center of the straight gathering channel (i.e., the distance-to-wall,  $D$  in  $\mu m$ ). b) The distance-to-wall for each type of target droplet. The data points, mean value, and standard deviation are shown with the point values, the single column value, and the error bars. c) The distance-to-wall for droplets containing exactly one cell for each corresponding cell size ( $\mu m$  in diameter).

### 4.3.2 Influence of droplet size

We also investigate the effect of droplet size on the trajectory difference. With the CTS-2 geometry, we adjusted the flow condition within the “Step and central breakup” flow regime to obtain different sizes of target droplets with a diameter from  $30$  to  $40\mu m$ . We also move the condition slightly further to the “Central breakup” flow regime where one mother droplet is broken into two large droplets with a diameter of  $60\mu m$ ; these droplets are studied together

with the above target droplets as the deformation-relaxation process should also influence them. All these flow conditions are very close; here, we assume that the droplet size is the only parameter that varies. In this study, we only focus on the single-cell droplets and not the multiplets/doublets. The distance-to-wall difference between an empty droplet and a single-cell-containing droplet ( $\Delta D$ , i.e., the trajectory difference) is quantified. As the efficiency of separation also depends on the droplet size itself, we define a parameter  $\Delta D/D_d$  that normalizes the trajectory difference with the droplet diameter. It represents how many times the trajectory difference is compared to the droplet size itself. Note, as  $D$  is measured in the straight gathering channel that is narrower than the reservoir, the  $D$  obtained is a value scaled down by a ratio between the gathering channel width and the reservoir width.

Fig.4.3a shows that the normalized trajectory difference decreases rapidly with the increase of the droplet size. This is not surprising as for a larger droplet, a cell will occupy a relatively small region and thus has a minor influence. For the use of HEK cell, which is approximately 13 to 14  $\mu m$  as the averaged diameter, when the droplet has  $D_d = 41\mu m$ , the trajectory difference induced by a single cell measured in the straight gathering channel is already less than 10% of the droplet size. At  $D_d = 60\mu m$ , there is almost no trajectory difference. We dissect the droplet-releasing process frame by frame for the case of  $D_d = 60\mu m$  and notice that in this case, the cell's effect is so small that the deformation-relaxation process of an empty droplet and a single-cell containing droplet become non-distinguishable (Fig.4.3b). When  $D_d = 30\mu m$ , the trajectory difference is slightly smaller than the one with  $D_d = 34\mu m$ . The reason is at this droplet volume, the inclusion of a single cell has created a significant change to the droplet size itself (from 30  $\mu m$  to 32.2  $\mu m$ ), which has an opposite effect on the trajectory, thus compensating the final trajectory difference. In general, it is true that the smaller the droplet containing a cell, the further away it will be propelled from the center. As proof, in the rare cases where the overly large cell has triggered the early breakup of a small satellite droplet (Fig.3), this satellite droplet is propelled very far away from the junction, almost touching the opposite wall.

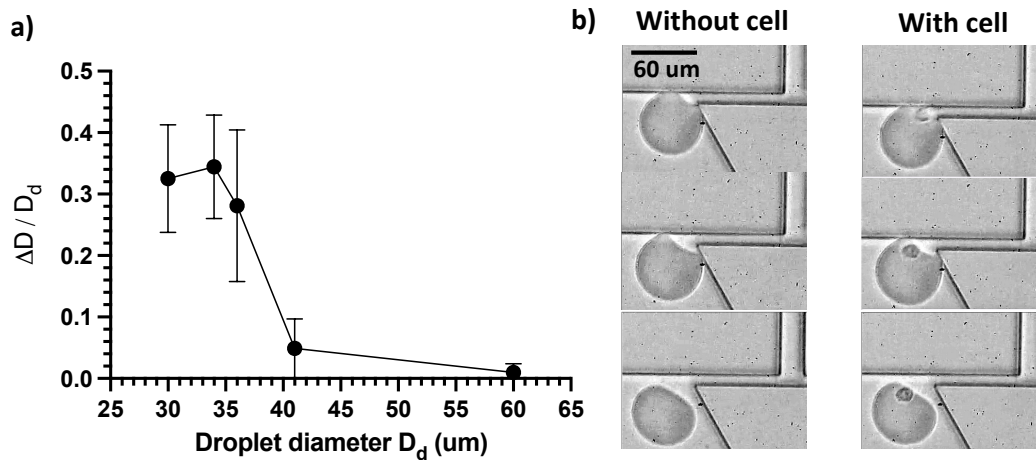


Figure 4.3 – **Influence of the droplet size on the trajectory difference.** a). The normalized trajectory difference ( $\Delta D / D_d$ ) versus the corresponding droplet diameter ( $D_d$ ). Each  $\Delta D$  data point is computed from a target droplet containing a single cell and its adjacent empty (target) droplet (one event before or after) in their difference in distance-to-wall ( $D$ , definition see Fig.4.2a); A minimum of 10 events are used to compute for each droplet size. b). The deformation-relaxation process of the large droplet ( $D = 60 \mu\text{m}$ )

### 4.3.3 Proof of concept

With CTS-2 geometry, the objective of separating different target droplets is achieved with a five-outlet structure with a divergent flow profile connected to the gathering straight channel. The initial trajectory difference among the droplets is maintained (proportionally) with the laminar flow; after entering the expansionary region with five outlets, they are diverted into their final collection channels. In this case, as the target droplets appear closer to the upper wall of the gathering channel (than the large ones), they are separated by the upper first separation wall (see Fig.4.4a). Fig.4.4b shows the sorting performance with a droplet size of  $34 \mu\text{m}$ . For all target droplets that contain single cells (i.e., the two columns with a plaid pattern), there are 348 out of 365 of them went correctly into the sample channels, corresponding to an efficiency of 95.3%. For all target droplets that went into the collection channel (i.e., the two columns with Green color), there are 348 out of 363 droplets containing single cells, corresponding to a selectivity of 95.9%. At this stage, we only demonstrated the separation between the empty and the cell-containing droplets without separating the single-cell droplets from the doublets. In fact, within the cell containing droplets that are in the collection channel, 12.3% of them are doublets. We did observe these doublets follow a different trajectory than the singlets in the same channel. Furthermore, only singlets are occasionally dispensed wrongly into the waste channel but never the doublets, showing that the latter are further away from the center outlets. In the future, one can create a secondary separation channel within the current single collection channel to obtain a pure population of singlets.

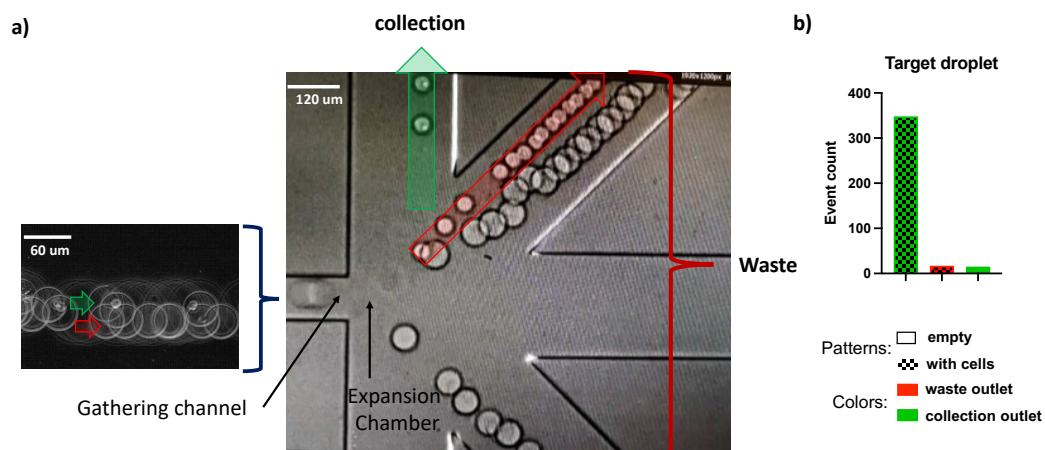


Figure 4.4 – **Sorting result of SCDT on the CTS-2 geometry**). a. (left) trajectories of the cell-loaded droplets and empty droplets in the gathering channel (right) bright field image of the sorting phenomenon. b. Statistics of the sorting performance. The color represents whether the counted target droplets appear in the collection (Green) or waste (Red) channels; The pattern represents whether the counted target droplets contain single cells (plaid) or are empty (plain)

#### 4.3.4 A generalized geometry

While the large droplets are ignored deliberately for demonstration purposes (large droplets are not counted in the above analysis), they did introduce unnecessary complications. For example, in the above experiments there are 25 cells partitioned into large droplets and thus ended up in the waste channel, i.e., the cells can be wasted due to the presence of the large droplets. 14 large droplets flew into the collection channel by mistake (mostly due to the droplet interaction at the separation corner), reducing the overall sorting efficiency. Furthermore, the alignment of the trajectories over the channels is more complicated if taking into account the fact that the trajectories of the empty large droplets need to be properly allocated as well (which is usually good by default but not always). Given these reasons, we seek a simplified geometry to use the same working principle we have shown above.

Fig.4.5a shows the geometry we designed specifically for SCDT. In the SCDT geometry, the bifurcate lateral narrow channel (i.e., the T junction) from the CTS-2 geometry is replaced with a one-way straight lateral channel, with width  $w = 12\mu m$  and different lengths of  $L = 5, 150, \text{ and } 250\mu m$ . Without the T junction, the target droplets are directly from the initial droplet generator and no secondary splitting will occur in the lateral channel, avoiding the unnecessary empty large droplets for any potential intervention. After this narrow lateral section, the channel expands into an asymmetrical reservoir with a  $\theta = 120^\circ$  inclination angle for the lower wall. The lateral section and the chamber are responsible for creating the droplet trajectory difference. Downstream, we also removed the “gathering-expansion” structure and replaced it with three symmetric outlets following the natural expansion of the functional

## Chapter 4. Single cell encapsulation based on Single Cell Differentiated Trajectory (SCDT)

---

chamber. Two of them are used for collecting the two types of droplets, while the last one is connected to the flow control unit to enable the laminar shifting of the trajectories as a whole. The goal of the latter is to match the separation of the trajectories with the corner separating the two outlet channels (highlighted with the transparent black box). We expect the single cell containing droplets to be accommodated by the leftmost outlet as they experience larger lateral migration than the empty ones according to the above principle.

Fig.4.5b shows the experimental sorting result with the overlapping droplet trajectories over different events. We demonstrated successful droplet sorting with a droplet diameter of  $40.5\mu m$ . In this chip, to create droplets with a small volume (e.g., diameter 30 to  $45\mu m$ ), without the secondary droplet breakup (“step and central breakup”) as in the CTS-2 chip, the incoming aqueous flow rate has to be set very low thus we have much fewer cells arriving for sorting (due to cell sedimentation, to be improved). Consequently, we observed only 6 droplets with single cells out of thousands of empty droplet events. Among them, 5 are correctly sorted into the leftmost outlet. We are amazed by the robustness of the empty droplet trajectories, which are all the same over thousands of events as shown in Fig.4.5b. This creates the basics for efficient droplet sorting, i.e., any trajectory disturbance from the single cells will guide the droplets into a different channel. Indeed, from Fig.4.3a,  $D = 41.5\mu m$  is already considered a relatively big droplet size which creates less distinctive trajectory difference compared to their smaller counterparts; and we still observed efficient sorting. Note that the  $\Delta D$  in Fig.4.3a is measured in the  $200\mu m$  wide gathering channel, and here at the separation point (red) the channel width is around  $700\mu m$ , thus we gained 3.5 times amplification of the net difference, which explains the efficient separation here. We also anticipate a much more significant separation if we bring the droplet size down (Fig.4.3a).

The above experiment confirms that, first of all, the on-site generation of the target droplets and the interaction with the large empty droplets, as appear in the case of CTS-2 geometry, is not necessary for creating the trajectory difference. Second, it shows that the key elements leading to the trajectory difference have all been captured by the SCDT geometry, which is the lateral narrow section and the downstream asymmetric and expansionary chamber.

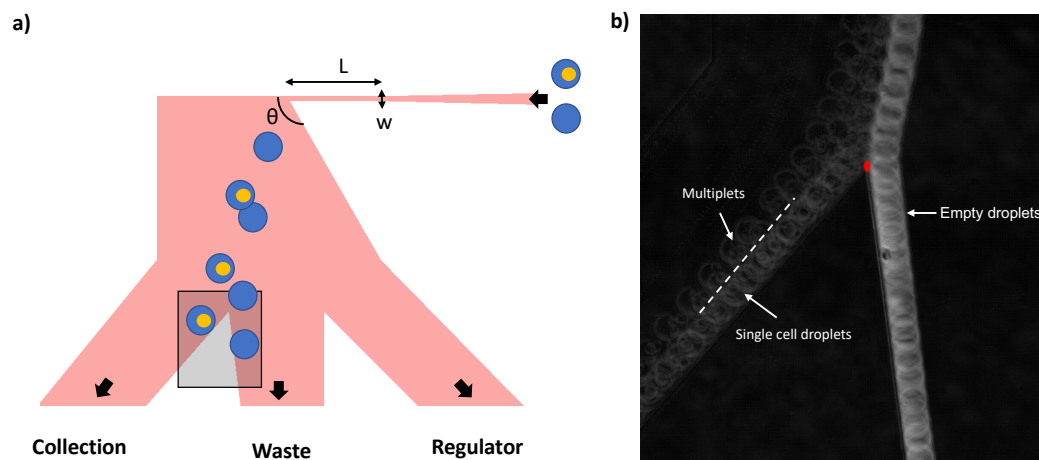


Figure 4.5 – **The SCDT geometry and proof of concept.** a). Schematic of the SCDT geometry and the parameters. The solid arrows show the flow directions. Blue and yellow circles indicate the droplets and the cells, respectively. The droplets are generated upstream and directly arrive at the inlet of the lateral channel shown by the rightmost arrow. No droplet splitting occurs prior to droplet sorting. b). The overlapping droplet trajectories from a video with 28 sorting events correspond to the highlighted region in a. Red point shows the separation point. The lateral channel length in this case is  $L = 250\mu m$ . The empty droplet, singlets, and multiplets are indicated. The brightness of each trajectory is proportional to the frequency of occurrence of that type of event.

We further conducted some experiments to understand the influence of the *droplet speed* and the *length of the lateral channel* on the sorting performance. Fig. 4.6 shows that with a similar droplet diameter at around  $D = 31.5\mu m$ , the trajectory difference between empty and cell-loaded droplets does not occur anymore when the droplet speed is too high. This result however needs to be further verified due to the lack of repetitions in the data sets. Two reasons might explain this phenomenon. First of all, with a too-high speed, the deformational force on the droplet might be too strong that exceed the cell's viscoelastic limit; thus the deformation-relaxation process becomes similar with or without the cell. Second, the time scale for axial migration for each droplet is set by the flow speed, which is largely reduced with the increase of the speed; thus the difference in axial migration might not be noticed anymore. These hypotheses can be verified in the future under a high-speed camera revealing the detailed process of droplets released at high speed. We also observed that with a lateral channel length of  $5\mu m$ , there is *no* droplet trajectory difference at all reasonable droplet sizes and droplet speeds we have tested. At  $L = 150\mu m$  and  $250\mu m$  under the same flow condition, the trajectory difference is re-established. It clearly shows the necessity of a long enough confinement prior to the droplet release.

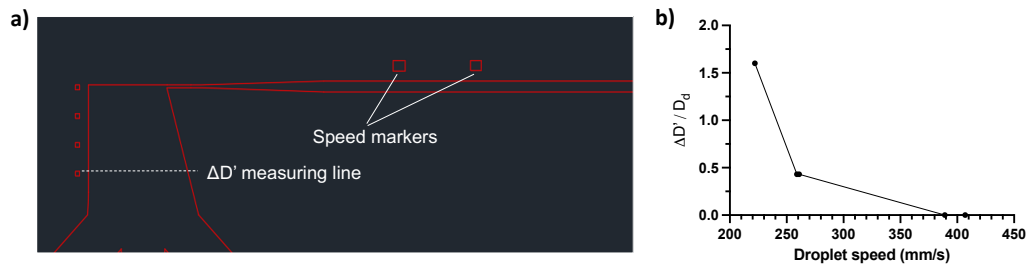


Figure 4.6 – **Influence of the flow rate.** a). Speed markers and measuring line for obtaining the droplet speed and trajectory difference in b.  $\Delta D'$  is defined as the distance between a cell-loaded droplet and its adjacent empty droplet measured at the level indicated by the dashed line. Note the difference between  $\Delta D$  and  $\Delta D'$ :  $\Delta D$  is measured in the  $200\mu m$  wide gathering channel, whereas for  $\Delta D'$  the channel width is  $450\mu m$  at the measuring line.  $\Delta D'$  is equivalent to 2.25 times  $\Delta D$ . b) Normalized trajectory difference versus droplet speed. For each experiment (data point) only one event is obtained due to the cell sedimentation problem.

## 4.4 Discussion

### 4.4.1 The narrow section and the single cell sorting resolution

In the above sections, we hypothesized that the reason for the droplet trajectory difference is due to the difference in the droplet deformation-relaxation process. In this hypothesis, the deformation degree of the droplet right after they are released from the lateral narrow section plays an important role, which is dependent on the levels of deformational force exerted on them. Haner et al. [52] have shown that if the flow configuration/mechanism fails to provide enough deformational force on the capsules, the same contrast in capsule's viscosity/rigidity will lead to less/no significant changes in capsule trajectories and thus poor sorting performance. Compared to changing the property of an entire droplet to realize the sorting, we now can distinguish the droplets' trajectories based on a very local change of the droplet property, as small as a single cell. Clearly, we have a strong mechanism that is sufficient to achieve this single-cell sorting sensitivity. We like to point out that this is likely due to the narrow section for two reasons. First, the focused flow stream that exits from the narrow section enables a localized and thus strong deformation of the droplets. This is the prerequisite for good sorting behavior. Second, the location of the cell is accurately placed at the most deformed part of the droplet, i.e., close to the rear interface, due to the narrow section. Experimentally we observed that when  $L = 5\mu m$  the cells exit early rather than at the last moment with the droplet, thus they do not occupy the rear deformed region as it is in the case for  $L = 150\mu m$  and  $250\mu m$ . It shows that a function of a (long) narrow section is to help displace the cell to the rear part of the droplet during release. Considering that no trajectory difference can be created in any condition in the case of  $L = 5\mu m$  (see above), it shows that the positioning of the cell at the right location is probably a key aspect. Indeed, when a cell occupies exactly the region where the largest deformation could happen, it could

make a significant contrast between an empty droplet and a droplet with a cell.

If we summarize, the localized deformation of the droplet plus an accurate positioning of the cell at the most deformed region, all caused by a narrow section that is slightly thinner than the cell, might explain the remarkable sensitivity at the single-cell level. At least, experimentally we have observed the necessity of the narrow section for distinguishable sorting at the single-cell resolution.

### 4.4.2 Other potential mechanisms

In addition to the above mechanism attributed to the deformation-relaxation process difference of the droplets, there might be other mechanisms that could explain the droplet trajectory differences. First, the squeezing of the droplet and the cell in the narrow lateral channel likely influences the internal fluid structure of the droplets and may contribute to the different propagation trajectories after the release. This mechanism can be confirmed with Particle image velocimetry (PIV). Another mechanism could be that the squeezing of the cell in the lateral channel increases the resistance and builds up the pressure in the channel, which when released, could cause a higher lateral speed of the droplet with the cells, resulting in a larger lateral migration. To test both hypotheses, one can build a long enough narrow section that is still thin but not thinner than a cell to see if the droplet trajectory difference can still be created. The result of this experiment will also have an important implication on whether this technique can be applied to a rigid object.

### 4.4.3 A versatile droplet/particle sorter based on the asymmetric wall effect

Similar to CTS, we expect that the SCDT mechanism will also work for sorting the droplets containing single deformable particles, as the latter would create the same effect on the droplets as the single cells according to the working principle. The scaling rule will be a narrow section that confines the particle and an expanded reservoir that connects to it. Above, we explained the function of the narrow section in achieving the single cell sorting resolution and the function of an expanded chamber (with a divergent flow profile) in realizing the final sorting. Next, we will discuss the aspect of the “asymmetric wall effect”. Altogether, it will justify the design rule of “narrow section + asymmetrical reservoir” as the key for sorting, and we propose that our geometry works as a general droplet sorter that not only sorts droplets based on the content but also on other properties like droplet size, speed, and viscosity, etc.

The asymmetrical flow profile of the SCDT device is shown in Fig. 4.7a. Let’s start with the Pinch Flow Fractionation (PFF) to discuss the sorting principles. In PFF, a pinching flow (arrow) is applied to push every particle/droplet against the lower channel wall such that the bigger objects are centered at the higher streamlines and the smaller ones are at the lower streamlines. With the streamlines becoming divergent in the reservoir, the objects are also separated Fig. 4.7b. Now we replace the wide pinching section with a narrow section that will always confine

## Chapter 4. Single cell encapsulation based on Single Cell Differentiated Trajectory (SCDT)

---

the objects as if the objects are pinched all the time. In this case, the objects are naturally well aligned to the same level regardless of their different properties. If with a symmetric expansion chamber (Fig. 4.7c), all objects will follow the center streamlines and no separation can be achieved. However, if we introduce a wall in the middle of this expansion chamber, we now have half of the stream profiles and more importantly, the effects due to the presence of the wall (Fig. 4.7d). When droplets have different sizes, the larger ones naturally occupy the lower streamlines due to the geometrical constraint from the wall. Moreover, the symmetric wake around the droplets is broken due to the wall, which creates a “wall induced lift force” that is especially prominent when droplets are close to the wall[92], which is the case when they are just released from the narrow section. This force is proportional to  $F \propto \rho U^2 a^6 / H^4$ , where  $\rho$ ,  $U$  are the density and velocity of the fluid,  $H$  is the hydraulic diameter, and  $a$  is the diameter of the particle/droplet[92]. A larger droplet experiences a much higher lift force than the smaller one which could propel it further away from the wall. Both effects combine to lead to that the larger droplets being dispensed to the lower outlets and are separated from the smaller ones. We have observed ( unintentionally) during the experiments that smaller droplets take a path further away from the exit of the narrow section.

In the case of droplets with different speeds, contents, or rigidity, the lateral migration of the droplets when exiting the narrow section is differed by the different properties. The asymmetric flow profile translates the different lateral migrations into the occupation of different sections of streamlines, thus enabling sorting. This is not possible with a symmetric flow profile. Overall, we like to point out that our special geometry design might be used as a versatile sorting tool for many sorting scenarios in microfluidics. The sensitivity for each mode of application however needs to be determined.

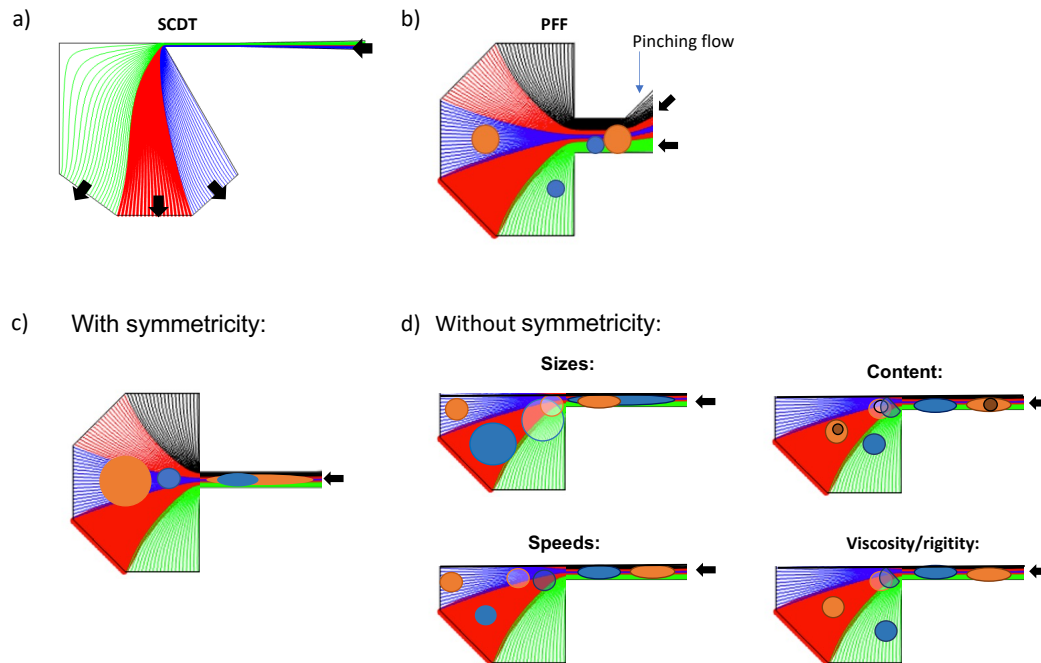


Figure 4.7 – **Illustration of the asymmetric wall effect (AWE)** Streamline profiles for all geometries. The flow direction is from the *right to the left* (black arrows). In each geometry, the streamlines corresponding to different outlets are partitioned into different colors accordingly. All streamlines point to their own outlets as shown in a (black arrows), same as for the others. Circles with different colors represents the droplets of different types.

## 4.5 Conclusion and outlook

In this chapter, we introduced a novel Single Cell Differentiated Trajectory (SCDT) mechanism for passive droplet sorting based on its single cell(s) content, which modifies the droplet deformation-relaxation process and influenced its trajectory in the downstream expansion chamber. The SCDT mechanism can be used as a powerful tool for label-free and deterministic single-cell encapsulation into droplets. We demonstrated this mechanism first with the CTS-2 geometry from the previous chapter, then on a simplified geometry specially designed for SCDT. The successful redesign strengthens our mechanical understanding of the design rule and the working principle. In both cases, we demonstrated the efficient sorting of the cell containing droplets from the empty droplets. While we show that the trajectory difference between an empty droplet and a singlet, and between a singlet and a doublet or multiples, are equally significant, we didn't demonstrate the separation of singlets from doublets or multiples yet. This can be implemented by using a cascade bifurcate collection design. Compared to the CTS method, SCDT preserves the benefits of being passive and asynchronous. In addition, it is a single-step sorting method with great simplicity and flexibility in tuning the droplet sizes, with the potential to further distinguish the singlets from the multiples.



# 5 Single object encapsulation based on passive blocking

## 5.1 Introduction

In the previous chapters, we presented two passive and deterministic approaches for single-cell encapsulation- Cell triggered splitting (CTS) and Single-cell differentiated trajectory (SCDT). While these approaches work well with single cells and other deformable particles, there are two main aspects we want to improve further in this chapter. First, both approaches rely on sorting after random encapsulation, which raises the need to statistically limit the number of multiplets using a high degree of dilution for particle/ cell samples. It causes a waste of reagent and operation time and still suffers from the waste of the cells via multiplets; Second, neither approach can be applied to rigid particles (e.g., with magnet), which have broad biological applications but would result in clogging in those devices. An ultimate (and elegant) solution would be to generate a droplet only when a cell or a particle has arrived. Indeed, while the previous chapters have been dedicated to single-cell droplet “(post) sorting” for deterministic collection of single-cell droplets, this chapter will focus on single-cell droplet “(selective) generation” to prevent the Poisson limit from the start. This approach uses a passive blocking principle on a “K-shape” device, and we named it "K Blocking".

## 5.2 Working Principle

The working principle of the K Blocking approach is shown in Fig.5.1. Oil flows through the main channel while water joins it from a vertical inlet. A suction channel with a reduced gate is placed 25  $\mu\text{m}$  downstream of the inlet junction, which, with adequate negative pressure, acts as an evacuation bypass for the incoming water phase. As a result, the oil and the water are in contact through a stable laminar interface, preventing droplet generation in the main channel (“water-all-in” condition). When a particle arrives with the water phase, it is carried toward the suction channel and blocks it. As the water stream can no longer flow into the suction channel, it is forced to penetrate the main channel. At this moment, the junction acts like a traditional T-junction for droplet generation, forming a droplet encapsulating the trapped

particle (“Blocking” condition). When the droplet continues to flow downstream, it also brings the particle away from the blocking location via surface tension. The suction channel is open again, which allows the system to resume the water-all-in condition for encapsulating the next particle. This mechanism allows an auto-running particle encapsulation process that is completely *deterministic*.

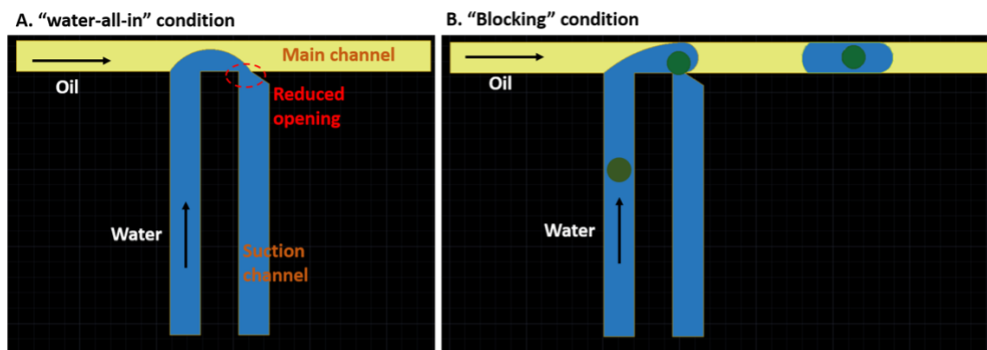


Figure 5.1 – **Working principle of the K Blocking approach.** The yellow, blue, and green colors present the oil, water, and cell phases. Arrows present the flow directions. (A): “Water-all-in” condition: incoming water stream is all directed into the suction channel, preventing droplet generation in the main (collection) channel. (B): “Blocking” condition: A particle arriving will block the suction channel, causing the aqueous phase to flow into the main channel to form a droplet. The droplet takes the particle via surface tension. The system resumes the “water-all-in” condition after releasing the droplet and the particle.

### 5.3 Fabrication development

For the above mechanism to work, it is highly critical to forming a good sealing of the evacuation channel via blocking. This poses specific requirements for the size, location, and shape of the gate of the evacuation channel, which could be challenging in terms of fabrication. In this thesis, we tested several fabrication strategies. Here we give a summary of the different strategies we used. Fig.5.2 shows the cross-sectional profile of the device obtained from each fabrication strategy. The red arrows point to the critical gate (of the evacuation channel).

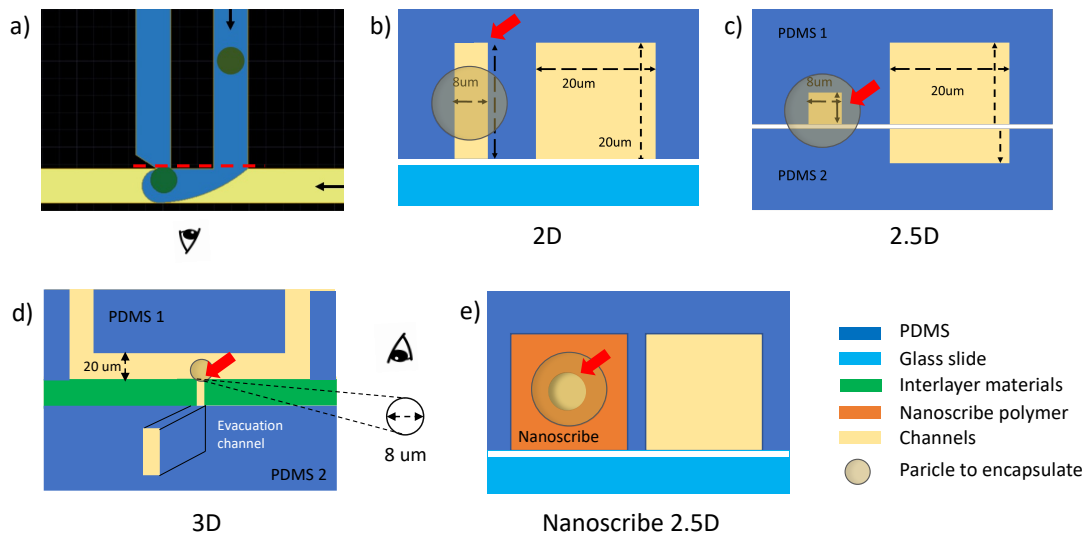


Figure 5.2 – **Devices from different fabrication strategies.** a) On the inverted working principle schematic, the dashed red line and the eye symbol indicate where the device profiles presented in b,c, and e have been taken; b) The 2D device made from one single-height PDMS and glass; c) The 2.5D device made from a double-heights PDMS and a single-height PDMS; d) The 3D (sandwiched) device where the top and the bottom layer are a single-height PDMS layer and are designed with the main + water inlet channels, and the lateral evacuation channel, respectively. The interlayer is aligned with the top and the bottom layer with a vertical evacuation channel drilled with a laser. Again, the cross-sectional profile is shown where the evacuation channel gate is off-plane. The top view of the latter is indicated by the black dashed lines; e) The Nanoscribe 2.5D device; it is similar to the 2D device, but the critical gate is fabricated with the customized Nanoscribe 3D printing.

### 2D device

In the first iteration (Fig.5.2b, 2D device), a single-height PDMS device is created from a silicon mold using photolithography. The evacuation channel is designed with a smaller gate from a 2D design. Experiments show that this configuration does stop the particle at the gate because of the smaller width dimension, but the water phase continues to be directed into the evacuation channel from the top and bottom of the channel, thus no droplet is formed as expected. A bad gate shape causes the failure that the particle can not well block.

### 2.5D device

In the second iteration (Fig.5.2c, 2.5 D device), a two-height PDMS (PDMS1) and a single-height PDMS (PDMS2) are separately fabricated and aligned together to form a large inlet channel and an evacuation channel of a square cross-section gate, located in the middle height of the channel. This configuration allows a smaller gate to be covered by the particle. With the 2.5D device, we started to see droplet generation upon particle arrival and blocking. However, we also observed that an unpredictable and non-negligible portion of the aqueous phase flow still penetrates the evacuation channel, leading to unrobust droplet generation. We attribute

this difficulty to the fact that the channel gate is square and not round; Also, the particle might not align well with the gate as it might stay at a different  $z$  location than the middle height location due to its higher density compared to water.

### 3D device

With this knowledge, we seek to build a 3D structure where the gate for blocking is moved from the side to the bottom of the channel (Fig.5.2d, 3D device). It is made of three sandwiched layers where the critical gate is located in the interlayer created via vertical drilling of a circular channel by laser machining. The main channel and the water inlet are defined in the top PDMS layer; The continuation of the vertical evacuation channel until reaching an outlet port for pressure control is defined in the bottom PDMS layer. Indeed, with traditional photolithography, the circular gate at the sides of the channels is not possible; In addition, the particles will sit on the bottom gate by default, avoiding ambiguous blocking alignment caused by the side-blocking strategy. We have tried different interlayer materials, including float glass (soda-lime glass), borosilicate glass, Poly(methyl methacrylate) (PMMA), and Polyethylene terephthalate (PET), to create the vertical evacuation channel from laser machining. We have also tried different laser machines, including an excimer laser and Femtosecond laser. We observed that for all combinations of materials and lasering methods, to achieve the cell scale blocking and encapsulation, the critical gate dimension required (2 to 8  $\mu m$  in diameter) is at the limit of the laser resolutions. This means poor reproducibility of the size and shape of the gate even under the same fabrication parameters; The roundness is poor (deformed into an ellipse shape), and there is material re-deposition around the gate, causing severe roughness for cells/particles to be released when needed. At the larger scale (above 20  $\mu m$  in diameter), the reproducibility of the gate shape is significantly improved. The gate is however still not round with more material deposition.

**Nanoscribe 2.5D device** Ultimately, we developed a novel fabrication strategy combining 3D direct laser writing and conventional PDMS lithography. All the channels are defined in a single-height PDMS layer, where the evacuation channel is as wide as the water inlet. We then used the two-photon stereolithography printer (Nanoscribe GmbH, Stutensee, Germany) to print in situ a 3D block at the beginning of the evacuation channel, which defines the critical gate. With the Nanoscribe technique, the infrared laser is focused on the UV-sensitive resist whose intensity at the focal point passes the two-photon absorption threshold, initiating energy transition and hence a polymerization reaction. The photoresist is first scanned in the bottom  $x$ - $y$  plane, then in the next  $x$ - $y$  plane with a different  $z$  location (and so on and so forth), with a resolution smaller than 700  $nm$  in the  $z$  dimension and 200  $nm$  in the  $x$ - $y$  dimension. This allows superior precision for the micro gate we want to build. At first, we printed the 3D block on a flat substrate and then transferred it to the target location. Problems like PDMS shrinkage, difficult alignment, and sophisticated transfer have caused poor fitting of the block, resulting in severe leakage (Fig.5.3 left). We later discovered that the 3D Nanoscribe block could be printed in situ on the open PDMS surface despite the channel topography. A seamless fitting of the block into the channel is realized by starting laser writing into one side of the PDMS channel (which causes no consequence) until reaching the opposite side of the

PDMS channel. The space in between is all polymerized into the 3D block, which ensures no leakage (Fig.5.3 right). Other technical developments include: 1. finding the right surface treatment to enhance resin -PDMS adherence; 2. the development of a manual focusing protocol; and 3. the efficient loading of resin overcoming the capillary effect at the corners of the channel topography. Ultimately, our protocol allows the fabrication of a leak-free and precise 3D microfluidics device. Because of the high resolution of the Nanoscribe printer, we obtained a good quality circular channel of  $2\mu\text{m}$  in diameter (Fig.5.3 right). Note that while in our case the geometry is a simple circular channel of a diameter of 2 to  $7\mu\text{m}$ , the 3D flexibility and precision brought by the two-photon lithography also allow the fabrication of any other shapes or sizes of the geometries. We name this method “Nanoscribe 2.5D”.

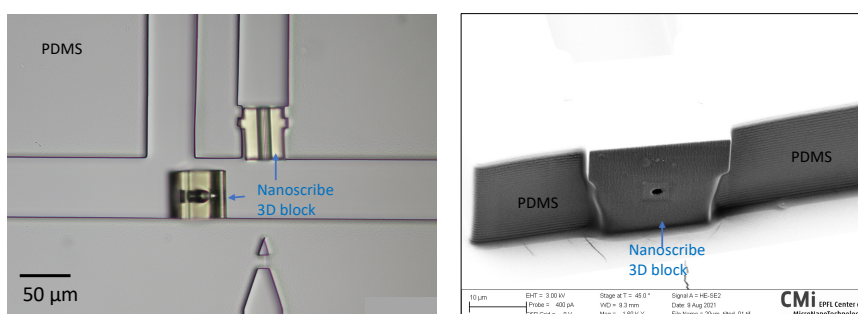


Figure 5.3 – **Different fabrication results of the Nanoscribe 2.5D devices.** (Left): we printed a larger-scale 3D block (block width =  $50\mu\text{m}$ ) and successfully transferred it to the desired location. The fitting between the block and the channel is however not good; (Right): Nanoscribe in situ printing with a suction channel gate of merely  $2\mu\text{m}$  in diameter that is well defined.

## 5.4 Result

### 5.4.1 Unsuccessful events with 2D and 2.5D devices

Fig.5.4 show some results obtained with the 2D and 2.5D device. While 2D device has completely failed in droplet formation, 2.5D device is able to generate droplets. Due to leakage, however, the droplet generation behavior is not robust (does not function as a normal T-junction). Sometimes, there is a depletion of the water bridge during droplet generation, excluding that particle from the formed droplet (Fig.5.4b); Sometimes, after droplet generation the whole droplet volume is depleted again, leaving only the particle at the gate (Fig.5.4c); Most of the time, the droplet generation duration varies significantly from one event to another, resulting in a large variation in droplet sizes (Fig.5.4d).

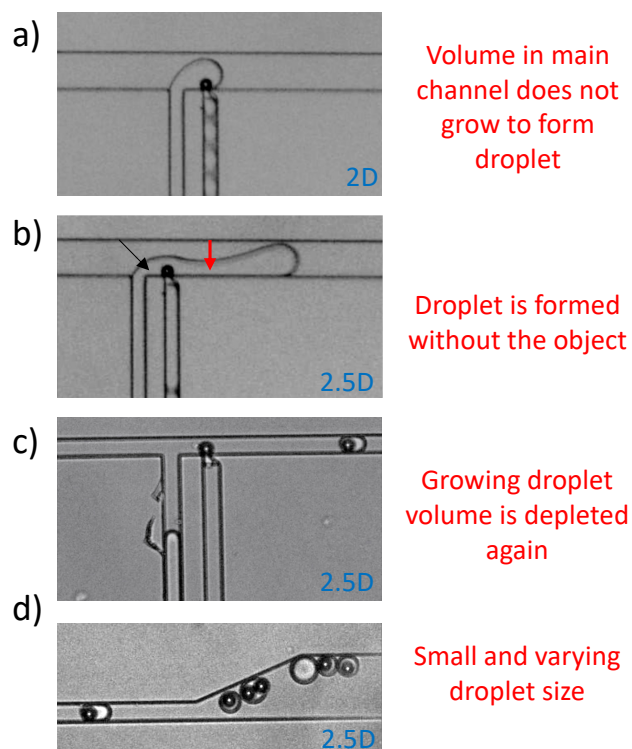


Figure 5.4 – **Unsuccessful results using 2D and 2.5D devices.** Note, in b) the red arrow indicates the actual pinch-off location; the black arrow indicates the expected/ideal pinch-off location; Leaking from the evacuation channel causes the unwanted pinch off. In d) the droplet containing two beads is a result of the droplet fusion of two initially very small droplets.

#### 5.4.2 Proof of concept with “full-blocking” mode

With the fabrication technique of Nanoscribe 2.5D, we created a perfect circular gate of a diameter of  $7 \mu m$  for encapsulating beads with a diameter of  $15 \mu m$ . With this device we observed, for the first time, the phenomenon corresponding to the working principle, as a convincing proof of concept for the mechanism (Fig.5.5). We observed that the bead blocks the evacuation gate perfectly, which induces the generation of a droplet that later carries the bead away. After Fig.5.5d when the tip of the aqueous phase arrives at the suction gate, the “water-all-in” condition is immediately resumed. The flow rate we applied here is  $0.16 \mu L/min$  and  $0.08 \mu L/min$  respectively for the oil and water, in a  $20 \mu m$ -wide-and-deep chamber. The throughput is dependent on the bead density in the solution as well as the droplet formation duration. In this experimental condition, it took  $60 ms$  from the onset of the blocking until the successful droplet release, which limits the throughput to below 17Hz.

However, the problem we observed from the 2.5D device (square gate) is not completely eliminated here with the Nanoscribe-2.5 D device (round gate). Only 2 out of 5 beads displayed

the perfect gate-blocking condition. In other cases, water leaks from the evacuation channel, hence a jetting condition is formed and a droplet is generated downstream to the bead instead of including it (see Fig.5.4b). Due to the un-robustness, we didn't continue to explore more flow conditions. Again, the problem might come from the side-blocking configuration. The sucking force is applied laterally from the gate to keep the bead suspended in the middle of the channel where the gate is located. In the meantime, the bead tends to sediment when it has no speed. Two effects are in competition, which might be the reason for the unrobust blocking. Instead of locating the suction gate in the middle of the cross-section (as it is currently), it might be beneficial to locate it lower in the suction channel. In addition, the 3D configuration (with a vertical suction channel) which is meant to solve this issue, can now be redesigned with the Nanoscribe + PDMS fabrication technique. An example is shown in Fig.5.6), where the critical geometries including the vertical suction channel and part of the buried lateral suction channel can be defined in a Nanoscribe block, which is built in a PDMS channel that connects to the pressure source. The proof of concept experiment has shown that the K-blocking mechanism is feasible if under a full blocking condition. We believe that a precise vertical suction gate can ultimately lead to perfect blocking.

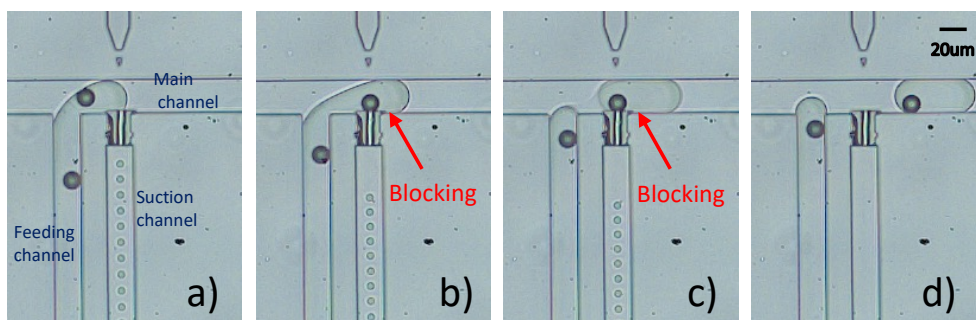


Figure 5.5 – **Proof of concept demonstrated with Nanoscribe 2.5D device.** Bright-field images of the automatic encapsulation process. a) “water-all-in” condition before the bead’s arrival. All water and some oil flow into the suction channel, forming droplets inside there; b) the bead arrives and blocks the suction channel, with no droplet formation in the suction channel from this moment, suggesting a perfect blocking; the water thread starts to grow into the main channel; c. a droplet is finally created by the pinch force of the oil; the little movement of the droplet train inside the suction channel compared to that in b suggests that no water and probably only a little amount of oil enters the suction channel during this droplet formation process; d) the droplet takes the bead away from the suction area and both of them move downstream; due to the re-opening of the suction gate, the oil comes in and immediately floods out the droplet train previously in the suction channel, the system is back to “Water-all-in” condition.

#### 5.4.3 An interesting working condition with “partial-blocking” mode

While the working principle we described so far will not work under poor blocking condition, we discovered a new and efficient working principle that works regardless of the bad

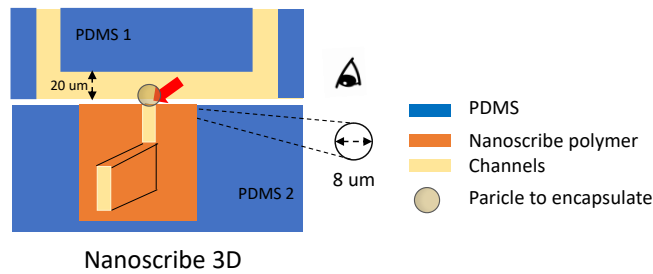


Figure 5.6 – The hybrid 3D device made of Nanoscribe block and PDMS channels

sealing (i.e., “partial blocking”). This experiment is conducted with  $Q_1 = 0.1 \mu L/min$  and  $Q_2 = 5 \mu L/min$  in a 3D device. Under this large oil-to-water flow rate ratio, droplets are generated immediately after the disperse phase penetrates into the main channel before the tip has reached the suction channel gate. However, these droplets are directed into the suction channel and are not collected in the main channel. Thus, it is also a water-all-in condition only without a static bridge of the disperse phase around the junction (“droplet-all-in”). When a droplet contains a bead, the bead prevents the droplet from entering the suction channel due to the size constriction. Although some disperse phase is depleted by the gate when the droplet passes over, a decent amount of droplet volume is still kept. Theoretically, the relative location of the bead inside the droplet would result in different degrees of depletion of the droplets, thus harming the monodispersity of the final droplet size. Interestingly, this is not observed. For the five bead-encapsulation events we observed, the encapsulation success rate is 100%, and the droplet diameter is  $70 \pm 2.3 \mu m$  with less than five percent variation. We think this is due to two reasons: 1. the initial droplet size is not big in this droplet generation regime, thus there is not much variation in the relative location; 2. due to the high oil flowrate, the time that the droplet (and the bead) pass over the suction area is very short, thus the depletion is not significant.

Although in this experiment the constant droplet generation frequency is at 10 Hz, this working principle has a great potential for high throughput. First, it intrinsically requires large oil flowrate for the instant droplet generation at the T-junction, easier to obtain high throughput; Second, passing over the gate does not have any time limit, and in fact the faster the better (i.e., better monodispersity); Third, not only T-junction but also other droplet generation geometries like flow-focusing can be used for this working principle, which could achieve ultra-fast droplet generation. We consider this new working principle an important alternative for the K-blocking concept. Especially, it bypasses the need to have perfect blocking and it allows droplet generation at a higher throughput.

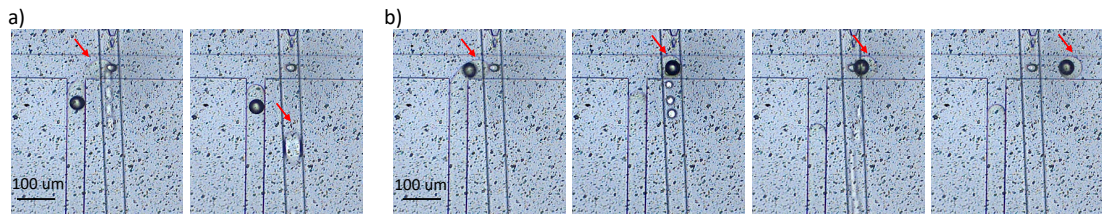


Figure 5.7 – **K blocking principle under “partial-blocking” condition.** This experiment was conducted in an old 3D device with an ellipse gate that is  $18\mu\text{m}$  wide, for the encapsulation of a bead around  $45\mu\text{m}$  in diameter. a) Process of empty droplet generation and the immediate evacuation; b) Process of bead-loaded droplet generation and the escaping towards downstream collection. Here, the camera focused on the main and water inlet channels (top layer); the vertical evacuation channel can only be identified as a hole in the interlayer; the bottom layer with the remaining part of the evacuation channel is out of focus. Red arrows point to the droplets.

## 5.5 Discussion

### 5.5.1 Design rule for the full-blocking mode

If we summarize the processes of a droplet generation event under the full-blocking mode to succeed, we can identify three steps (or criteria) to fulfill:

1. Complete blocking of the evacuation channel by the particle;
2. Droplet generation under “dripping” or “squeezing” regimes;
3. The bead is released from the blocking location *within* the droplet.

First, when the system achieves complete blocking without any leakage, this device is turned into a normal “T-Junction” where the generation of a droplet is systematic. On a usual T-junction, there are different droplet generation regimes, dependent on the relative strength between the viscous force and the surface tension force, captured by the capillary number  $Ca$  (Chapter 2). At a low capillary number ( $Ca \ll 0.01$ ), the water tip has the time to occupy the width of the main channel entirely; thus, the breakup is dominated by the drop of pressure across the water tip in the main channel, the regime is called “squeezing”; At larger  $Ca$ , a partial filling of the main channel by the discontinuous phase starts to happen, where the viscous force becomes dominant for the breakup, leading to the “dripping” regime; Further increasing  $Ca$  leads to “jetting” regime, where the droplet generation location shifts downstream [93]. These regimes are shown in Fig.5.8a. If the droplet generation regime is “dripping” or “squeezing”, it is certain that the droplet will include the bead when it is generated. The happening of jetting mode can be due to a leakage from the evacuation channel which depletes the water bridge and creates a tunnel for the oil to pass. This will not happen if the first criterion of complete blocking has been achieved. The jetting can also happen due to inappropriate flow

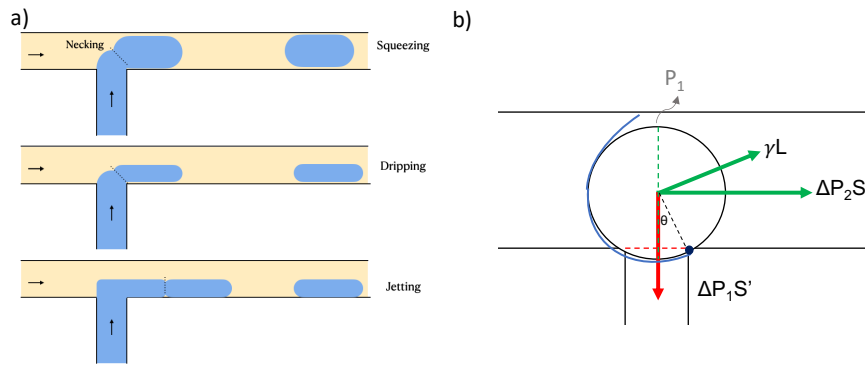


Figure 5.8 – a. Different droplet generation regimes in T junction; b. The different forces exerted on the particle that is above the evacuation gate. The channel wall is shown with black lines, blue line indicates the droplet interface, a red arrow for the pressing force, and green arrows for the pushing forces.

conditions. Fu. et. al.[94] show that jetting is more likely to happen with a higher water-to-oil flow rate ratio and a higher water-to-oil viscosity ratio under a larger capillary number defined with the continuous phase. This knowledge should help us better choose flow conditions to avoid the jetting mode.

If the first two criteria are fulfilled, we are sure that a particle will trigger the generation of a droplet containing that particle. With the droplet moving downstream in the main channel, its rear interface will eventually touch the immobilized particle. At this moment, two scenarios can happen:

**a.** The drag force exerted on the particle through the droplet rear interface is strong enough to overcome the pinning force exerted on the particle. In this case, the droplet and the particle will together be released from the junction, and the K-blocking mechanism can function automatically as expected.

**b.** The drag force cannot overcome the pinning force of the particle. In this case, if the oil flow in the main channel pushes the droplet beyond its deformation limit, the droplet will detach from the particle and moves downstream without the particle (Fig.A.3); if for the droplet, the drag force is balanced with the surface tension that prevents the further deformation of the droplet, the droplet will be pinned by the particle at the junction. In both cases, the K-blocking mechanism cannot work. Therefore, it is necessary to understand in what condition a particle can be released with the droplet. We will briefly discuss a scaling law for predicting the particle-releasing problem for a given flow condition and a given geometry.

### A simple Torque balance

We show the competing forces on a particle blocking the gate in Fig. 5.8b. The pressing force is shown in red. Assuming  $P_3$  is imposed, when the (full) blocking happens, there is no flow

and thus no pressure drop within the suction channel thus, the pressure below the particle is immediate  $P_3$ . The pressure difference across the particle ( $\Delta P_1 = P_1 - P_3$ ) exerts a pressing force  $\Delta P_1 S'$  that stabilizes the particle during the droplet formation process, where  $P_1$  is the pressure above the particle and  $S' = \pi(\frac{l}{2})^2$  is the gate area of the suction channel ( $l$  is the gate diameter).

The pushing forces are shown in green. Before the droplet touches the particle, itself is a free-moving object experiencing a drag force that is well depicted in the literature. This drag force is relatively small. Once it is “pinned” by the fixed particle, it starts to feel an enhanced “drag force” due to the resistance to flow of the continuous phase ([95]). This resistance to flow exerts a pressure drop across the droplet ( $\Delta P_2$ ), which is exerted on the particle through their joint interface. Take the cross-section of the main channel as  $A$ , the projection of the particle’s cross session in the main channel as  $S$ , a force of magnitude  $\Delta P_2 S$  is pushing directly (an enhanced drag force) on the particle through the joint interface (for simplicity, here we use  $S$  as an approximation for the projection of the joint interface), and  $\Delta P_2 (A - S)$  is responsible for the droplet deformation. Due to the droplet deformation that is caused by the force of  $\Delta P_2 (A - S)$ , surface tension also acts on the particle through the contact area, scaled as  $\gamma L$ , where  $L$  is the circumference of the joint interface,  $\gamma$  is the surface tension coefficient. In total, it is  $\Delta P_2 S + \gamma L$  that gives the particle an enhanced pushing force which might help it escape from the trapping zone. All the rest of the pushing force is responsible for the continuous deformation of the droplet.

As part of the particle is inside the suction channel, we assume the release of it into the main channel is through rotation around the right corner of the channel (assume non-slipping condition). The enhanced drag forces and the pressing force create torques of different directions: the former help the particle rotate into the main channel ( $T_2$ ); the latter pulls the particle back to the trapping area ( $T_1$ ).

Set the particle radii as  $r$ , we have:

$$T_1 = \Delta P_1 S' r \sin \theta \quad (5.1)$$

$$T_2 = \Delta P_2 S (r \cos \theta) + \gamma L r \quad (5.2)$$

If  $T_2 > T_1$ , the particle can be removed from the trap. The derivation of  $\Delta P_1$  and  $\Delta P_2$  is presented in Appendix A.3.

We verified this model with the full-blocking experiment. We obtain  $T_1 = 1 \mu N \cdot \mu m$ , and  $T_2 = 9.9 \mu N \cdot \mu m$ . It shows that the torque to rotate the particle from its location is almost 10 times larger than the torque to trap it. It predicts the release of the particle as also observed in the experiment.

The model shows several interesting results. First, by comparing the magnitude of the different forces we obtain the pressing force as  $\Delta P_1 S' = 0.30 \mu N$  and the pushing forces which include

## Chapter 5. Single object encapsulation based on passive blocking

$\Delta P_2 S = 1.41\mu N$  and  $\gamma L = 0.08\mu N$ . We can see that the surface tension is more than one order of magnitude smaller than the enhanced drag force, signifying that the main reason for removing the particle from the suction area is through the pushing from the oil. Second, to ensure particle releasing,  $\frac{T_2}{T_1} > 1$  is required. Ignoring the surface tension term, we obtain an expression:

$$\frac{T_2}{T_1} = \frac{aL_D \cdot (\frac{b}{h})^4 \cdot (\frac{l}{r})^3 \cdot \sqrt{1 - \frac{l}{2r}} \cdot (\frac{Q_1}{Q_2})}{(1+c)(R_{out} + R_S)} \quad (5.3)$$

where  $a = \frac{64\pi\mu}{(4-\pi)^2}$  is a constant,  $b = 1 + \frac{h}{w} + \sqrt{\left[1 - \frac{h}{w}\right]^2 + \pi \frac{h}{w}}$  is a correction factor for the aspect ratio of the rectangular channel where maximal value can be obtained at aspect ratio equal to one (i.e., a square shape cross section),  $c$  is the ratio between oil and water flowrate that is being evacuated in the suction channel,  $l$  and  $r$  represents the diameter of the gate and the radii of the particle,  $Q_1$  and  $Q_2$  is the injected oil and water flow rate from the inlets, and  $R_{out}$  and  $R_S$  is the channel resistance of the (main) outlet channel and the suction channel. If we take into account the influence of  $h$  on  $R_{out}$  and  $R_S$  assuming a single height device with rectangular channels, we obtain :

$$\frac{T_2}{T_1} \propto \frac{L_D (\frac{b^4}{h}) \cdot (\frac{l}{r})^3 \cdot \sqrt{1 - \frac{l}{2r}} \cdot (\frac{Q_1}{Q_2})}{(1+c)(\frac{L_{out}}{w_{out}} + \frac{L_S}{w_S})} \quad (5.4)$$

where  $L_{out}$ ,  $L_S$  and  $w_{out}$  and  $w_S$  are the length and width of the outlet main channel and the suction channel respectively. In terms of the design rule, it shows that the probability of a particle being released is dramatically increased if the particle-to-gate size ratio ( $r/l$ ) is large. In general, it is better to have a smaller dimension channel with square shape cross section. In such a case, a smaller gutter radius will be created to form a large pushing force for a given flow rate of the oil. It is also recommended to minimize the  $\frac{L}{w}$  ratio for both the outlet and the suction channel to minimize their resistance. During the operation, a large  $\frac{Q_1}{Q_2}$  ratio is favored. It is also beneficial to lower the  $c$  through wetting property control and by avoiding excessive suction pressure.

### 5.5.2 Potentially more suited for rigid bead encapsulation

In microfluidics, it is common to use trapping operations to realize different functions for the cells. For example, Duchamp et. al. [96] used a trapping geometry to immobilize one type of cells and allow another type of cells to each continuously “roll over” the first type of cells. Samlali et. al.[59] use trapping geometry and sequential operations of two-phase flows to trap and then encapsulate single cells. Clipp et. al. [97] used a hydrodynamic trapping array to immobilize one type of cells, which are approached by the second type of cells under the control of the Dielectrophoresis (DEP) forces. In these approaches, single-cell trapping is demonstrated either passively (only via fluidic design without external control) or actively (with external control). In all cases, only a portion of the incoming flow is carefully directed into the trapping region for trapping the single cells without rupturing them or making them

extrude. Indeed, a balance needs to reach between (low) trapping efficiency and (significant) cell harm/loss. In our case, the working principle requires that *all* water phase is directed into the evacuation channel. Here, no risk is present that a cell will not arrive at the trapping zone, and the deformable objects have more chance to provide a perfect sealing of the suction gate even if the shape of the latter is not perfect; on the other hand, it also means that a cell or a deformable particle can be easily compromised under such a strong force; in addition, the more it is inside the evacuation channel, the harder it is to be released from the channel and therefore lost in the channel (eq.5.3). Whether or not this mechanism will force a pressure that will extrude a soft object blocking the channel gate affects the range of applications for this mechanism.

Here we want to discuss one event which we observed when we were still using the 3D fabrication approach and we created an ellipse shape channel gate of a diameter of around  $8 - 9\mu m$ . We obtained the “water-all-in” condition with  $Q_1 = 1.2\mu L/min$ ,  $Q_2 = 0.2\mu L/min$ , and  $P_3 = -110mbar$ . Given the relatively large gate size (we cannot go further down with the 3D approach as explained above), we report only a case with an ultra-large cell that has around  $19\mu m$  in diameter. After it arrived, it indeed blocked the gate and induced the generation of a new droplet. But itself was lost in the evacuation channel. This shows that a soft material might not stand this mechanism.

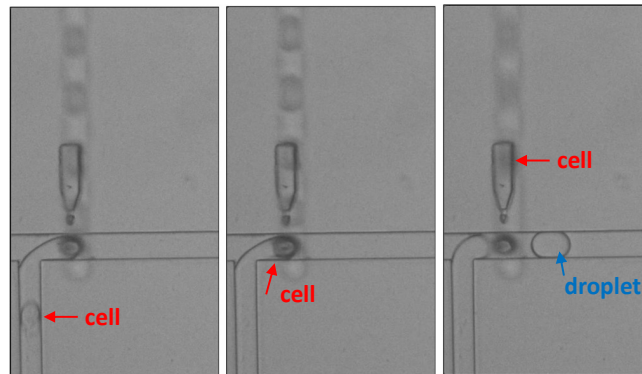


Figure 5.9 – **One event with cell on the 3D device** For this event, the camera focused on the main and water inlet channels (top layer).

## 5.6 Conclusion and Outlook

In this chapter, we introduced another approach for the deterministic encapsulation of single particles into droplets. The working principle uses the passive blocking effect to achieve that a droplet will only be generated or collected when it is loaded with a particle. We introduced two working modes- the original mode is where aqueous phase is directed into an evacuation channel as a continuous phase bridging the water inlet and the evacuation gate- particle triggers droplet generation (“water-all-in” mode); the new mode is where aqueous phase tip will always be broken into one droplet, which is then directed into the evacuation channel (if

## Chapter 5. Single object encapsulation based on passive blocking

---

empty) or to the main collection channel (if has a particle)- particle triggers droplet collection (“droplet-all-in”) mode. The former requires a “full blocking” for droplet generation, the latter only requires “partial blocking” as droplets have always been generated. In order to realize the first mode, we developed different fabrication strategies and found that the combination of 2-photon 3D writing (for the critical parts) and PDMS fabrication (for the non-critical parts) give a great compromise between precision and cost. Indeed, when it comes to having a perfect blocking, it poses critical requirements for the gate geometry (i.e., fabrication) as well as the flow condition; due to the relatively small oil flowrate, there is also the need to consider whether the particles can be taken by the droplets, whereas this is not a concern in the second mode with a strong oil flow rate. For this concern, anyway, we have developed an analytical model for predicting the particle releasing behavior. This model is only verified by one experiment (that has the perfect blocking) so far. Both modes ensure that this approach for deterministic single particle encapsulation is completely passive and deterministic. Unlike the sorting-based methods we introduced in chapter 3 & 4 which use the cells’ deformation property, this approach (with both modes) might be more suited for rigid particles (that cannot extrude into the evacuation channel), thus forming a good complement to the above methods. Until now, for rigid particles, only inertial ordering can be applied (i.e., cannot be densely packed) to enhance its particle loading efficiency. Our approach might be the first deterministic, passive and asynchronous method that could apply to the rigid particles.

In the future, one can improve on the geometry of the evacuation gate and to realize an automatic “full blocking” for the first mode. This mode might create a better control on droplet size but with a lower throughput compared to the second mode with “partial blocking”. It is thus also very interesting to study the second mode and to find out the working efficiency, the throughput limit, the collected droplet size limit, and the particle density limit.

## 6 Deterministic droplet pairing and merging

So far, we have obtained a full toolset for deterministic single-object encapsulation, covering deformable and rigid objects, for small or large objects, within small or large droplets, and under different throughputs. These techniques cover almost all encapsulation scenarios for the current applications of droplet-based microfluidics. They provide a pure population of single object-loaded droplets. In this chapter, we will further develop a deterministic droplet pairing and merging technique for using these pre-generated droplets. The goal is to accurately merge different droplets containing distinct types of objects with a controlled merging ratio.

### 6.1 Introduction

Currently, single cells assays that require the pairing of one single cell with another one or more cell/bead are highly sought. Examples include single-cell RNA sequencing (one cell + one bead), single-cell antibody screening (one cell + one bead), single-cell targeted genome analysis (one cell + one bead), cell-cell interaction screening (one cellA + one cellB), cell-cell communication profiling (one cellA + one cellB + one bead), etc. Currently, the most popular construction method for these droplet assays is co-flowing different object suspensions through a droplet generation junction to co-encapsulate the different objects randomly into each droplet. The object occupancy of the droplets thus follows dual Poisson statistics featuring very low efficiency and severe cell loss. For example, even aided by the super Poissonian distribution via packing of deformable beads, the current commercially available single-cell RNA sequencing does not apply to rare cell samples and causes at least half of the cells not to be analyzed[20]. In the case of pairing two distinct cell types which are of great importance in immunology and cancer biology [98, 99, 100, 101], only random co-encapsulation can be used, which creates most droplets with undesirable combinations (between 86.5% to more than 99% of the total population), and only 1-13.5% of total cells are eventually combined with one other cell. For three objects to be encapsulated, the situation is significantly worsened. We propose that to overcome this limit, multi-object droplet assays need to be constructed from pure single-cell/particle droplets and the precise pairing and merging of these droplets with accurate compositions.

In this chapter, we have developed a deterministic merging device with a principle called “In-flow merging”. So far, we have realized the proof of concept with two types of droplets that are generated on the same merging device. In the future, we would need to transfer this knowledge to merge pre-generated droplets as intended.

### 6.2 Working principle

Fig.6.1a shows the working principle of the In-flow merging method. We designed a waiting line structure to store droplet type A (called “droplet A” or “droplets A” in the following for simplicity), and we flow droplet type B one by one into the main channel. The main channel width is smaller than the droplet B diameter such that a confined droplet B when passing the waiting queue of droplets A will be forced into contact with the forefront droplet A in the queue. At the junction of the waiting line and the main channel, a localized AC electric field is always applied and disturbing every droplet pair that passes by, causing electrocoalescence. The two droplets thus merge and the part originally from droplet B will continue to be pushed downstream, take the part from droplet A with it for collection. The empty spot created in the waiting line will be filled up instantly by the second droplet A due to the small distance and increased flow resulting from a decreased resistance, which prepares the next merging event, and so on and so forth. The waiting line is pre-filled with droplet A during the operation; thus droplet B can be injected at different frequencies (regular or irregular). This principle eliminates the synchronization effort (i.e., real-time flow rate tuning) while still allowing the system to run in the continuous flow condition. The “no pairing, no leaving” principle also ensures that all droplet A will be paired by one and only one droplet B. Indeed, even if electrocoalescence does not happen 100% each time a droplet B meets a droplet A, the missed droplet A is not lost but can be paired and merged with the next droplet B, guaranteeing the pairing accuracy for droplet A. The pairing efficiency of droplet B can also be improved via recycling. As only two sizes of droplets- small size containing droplet B and large size containing one A and one B- exist downstream, a simple size sorting will recover the unused droplet B for reinjection to the system for the second round of pairing, limiting the waste.

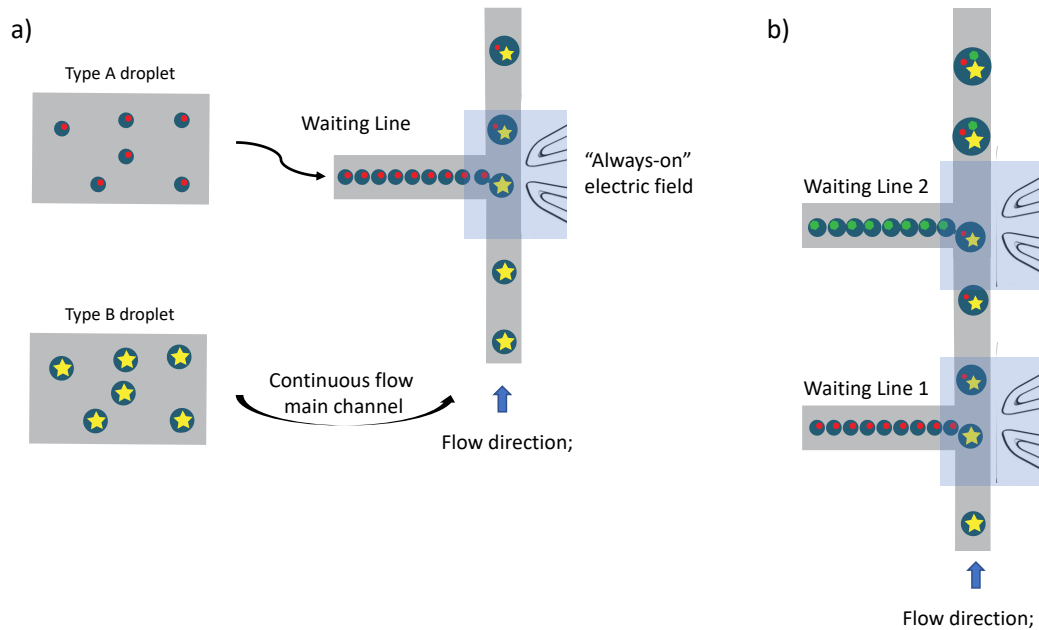


Figure 6.1 – **Working principle of the In-flow merging approach.** Blue arrows indicate the flow direction, where the vertical channel is the main channel. The blue shaded areas illustrate the localized electric field, and the distinct objects (with different sizes) within the droplets are represented by different symbols (red circles, yellow stars, green circles, etc.). a) Illustration of merging two types of droplets. (B) Illustration of merging three types of droplets.

The same principle can be easily extended to achieve the deterministic merging of more than two types of droplets. As shown in Fig.6.1b, a third droplet type can be stored in a second waiting line. After two consecutive electrocoalescence, a droplet containing three distinct objects can be created automatically in the collection outlet. For each new droplet type to be added to the final combinatory droplet, one waiting line can be appended accordingly. In the case of 100% electrocoalescence efficiency at each merging step, the number of waiting lines does not have an influence on droplet assembling efficiency. In the case of not 100% electrocoalescence efficiency, the error rate will increase with an increasing number of waiting lines (i.e., droplet types). However, the desired combinatory droplet would always have a unique and different size than the rest of the droplet types, which can be recovered by size from downstream. In addition, the overall efficiency of obtaining desired combinatory droplet is still significantly higher than the pure-Poisson statistics, as all droplets will at least have a single B (i.e., the type introduced from the continuous flow).

### 6.3 Result and Discussion

For the above working principle to work successfully, a good combination of fluidic conditions and electrocoalescence conditions is required. In this section, we will discuss separately the optimization of the two parts. And finally, we will present the merging performance of the

device up to today.

6.3.1 Fluid elements

In this method, a key aspect is to prepare the waiting condition of droplets A via fluid control. Our fluidic elements are shown in (Fig.6.2a). At this stage droplets A and B are generated on chip (empty) through a flow-focusing geometry (green circles) for proof of concept. After the generation, droplets A flow through four fluidic structures (J, A, B, WL) before reaching the merging point (red path). Droplet B will arrive at the merging point directly ( yellow path). After the junction, both paths join into one main path for collection (brown path). The condition of different fluidic elements (J,A,B,WL) during operation is further shown in Fig.6.2b. The J element is a shortcut channel connected to the atmosphere to evacuate a

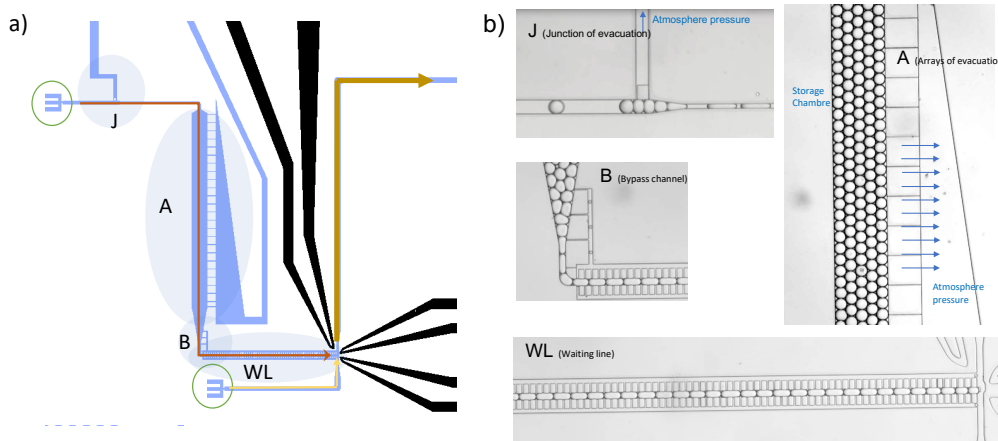


Figure 6.2 – **The optimisation of the fluidic elements.** a) Schematic overview of the chip design. The blue color indicates the fluidic channels and the black color represents the electrodes. The red path is for droplet A after it is generated; the yellow path is for droplet B after its generation; the thick brown path is after merging the path for the new droplet. b) Bright-field images taken during the experiments for the different individual fluidic elements.

significant amount of incoming oil flow from the system. A square post stands in the junction to prevent droplets from leaving. Downstream to the J element, the droplets flow into a chamber where the excessive oil flow is further extracted through an array of small channels that are also connected to the atmosphere (A element, design idea from [102]). After two times of flow reduction, the droplets are loaded into the waiting line structure (WL), slowed down by the pillar array ([103]), and stopped in front of a post at the end of the waiting line. Excessive droplets will continue to accumulate in the storage chamber, which completes the chip priming step. Afterwards, the droplet A injection can be stopped or resumed at any time. A bypass structure (B) is designed at the chamber-to-WL transition area (narrowing neck) to prevent pressure accumulation that might cause droplet merging.

Optimizing fluidic elements particularly concerns the modulation of the degree of passive oil

extraction via the design of J & A elements. We used numerical simulation to aid the design optimization. As a rule of thumb for design, we seek for a moderate and positive pressure gradient in the WL for automatic droplet loading and refilling of the WL while keeping droplets away from breaking. It is also essential to ensure the stopping of droplets A in the waiting line. More details can be found in AppendixA.4.

#### 6.3.2 The electrocoalescence theory

After achieving the waiting behavior of droplets A, the next goal is to improve the electrocoalescence efficiency as well as selectivity, meaning that the first droplet A should be sensitively merged with droplet B but it should not merge with the second droplet A.

Currently, it is commonly accepted that the processes of two droplet coalescing in an electric field include: droplets approaching each other, the film in between drains and thins, and finally the film ruptures and merge [104]. There are three possible mechanisms to cause a droplet pair in an electric field to approach each other:[105]: 1. electrophoresis (EP), where droplets of opposite charges in an electric field are attracted to each other; 2. dielectrophoresis (DEP), in a gradient of the electric field a drift is created due to permittivity difference between the droplet and the insulating oil; 3. dipoles interaction, the electric field polarizes the uncharged droplet (as dipole) which experience mutual attraction. While both dipole interaction and DEP utilize the difference of polarizability in droplets and the surrounding oil media, the EP force relies on the net droplet charge. In our case, we have uncharged droplets as the electrodes are not in direct contact with them. In addition, we apply AC electric field to avoid potential electrochemical side effects affecting biological assays, which also undermine the effect of EP. EP is thus ruled out in our case. Studies show that a nonuniform electric field can enhance electrocoalescence of water-in-oil emulsions[106, 107]; also, it is not possible to configure a uniform electric field in all three dimensions across the two droplet interfaces, due to the channel constraint. In our study, a non-uniform AC electric field is applied. While dipole interaction is considered the main mechanism for electrocoalescence in a uniform field, in this case, both the dipole interaction and DEP play a role.

Luo et. al. pointed out that among the two contributions, it is the interaction of the dipole that plays a dominant role when the two droplets are placed closely [107]. He derived the inter-droplet attractive force due to dipole-dipole interaction of two (unbounded) droplets in a nonuniform electric field as:

$$F_{12} = \frac{-12\pi\epsilon_m K_e^2 |E_1| |E_2| R_1^3 R_2^3}{|d^4|} \times f \quad (6.1)$$

where  $\epsilon_m$  is the dielectric constant of the medium (oil),  $K_e$  is the Clausius-Mossotti factor representing the effective polarizability of the droplets (more see below).  $E_1$  and  $E_2$  is the electric field at the location of each droplet.  $R_1$  and  $R_2$  are the corresponding radii of the droplet, and  $d$  is the distance in between.  $f$  is a factor taking into account the angle between the induced

## Chapter 6. Deterministic droplet pairing and merging

---

polarization vector (E-field direction) and the vector that connects the two droplets' center, i.e., the dipoles interaction force is influenced strongly by the orientation of the induced dipoles. This force also decays rapidly with the droplet pair distance ( $\propto d^{-4}$ ).

In terms of DEP, the time-averaged DEP force acting on an unbounded droplet in a dielectric media is given by[108]:

$$\langle F_{DEP} \rangle = 2\pi R^3 \epsilon_m K_e \nabla \left| \vec{E} \right|^2 \quad (6.2)$$

Therefore, it is the gradient of the squared electric field instead of the magnitude of the field itself that influences this part of the force exerted on the droplets. In our case, droplets have both higher permittivity (around 40: 1) and conductivity than the oil, the resultant  $K_e$  is thus always positive under low or high frequency. This means that the DEP force will always draw the droplets towards the high field gradient, which is located between the two electrodes at the right side of the merging point. Due to the channel confinement, droplet B cannot move further toward the electrode, but droplet A will be drawn towards droplet B, helping to bring both droplets closer and squeezing the oil film in between. From above, the two electric forces are dependent on the polarization degree of the droplets and the oil medium, and so will the electrocoalescence efficiency. Our electrode design and the optimization of the electrode configuration via simulation to enhance the electrocoalescence selectivity, are presented in Appendix A.4.

### 6.3.3 The merging performance

**The process of merging** With the optimized combination of fluid elements and electrode configuration, we achieved the desired deterministic droplet pairing and merging behavior. Specifically, when chip fabrication has no defect, we observed automatic and consistent behaviors for droplet A during its filling and waiting processes. When droplets B pass by, electrocoalescence starts to happen. Fig.6.3 shows a typical merging event, which includes: the smooth loading of droplets A (green), droplets A stopping at the merging point, one droplet B (blue) arriving and merging with the first droplet A, the new droplet (yellow) leaves, and finally the droplet A queue is filled up for the next event. Typically, droplets A can stay in the waiting line without leaving for at least five minutes. In practice, droplet B injection operation is prepared in advance, which can be performed immediately after droplet A waiting line is achieved; thus five minutes is more than enough. In some cases, electrocoalescence does not happen very efficiently or selectively, meaning that some droplets B do not succeed in taking droplet A, or droplet B takes two droplets A at a time via droplet A-A merging (i.e., A-A-B merging). This is a matter of electrocoalescence sensitivity and selectivity, which is influenced by several factors shown below.

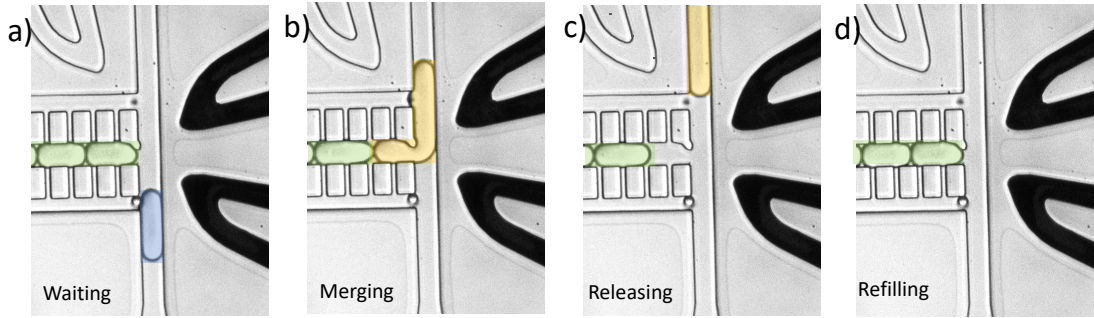


Figure 6.3 – **Proof of concept of the in-flow merging** a-d) Bright-field images of the time points for when droplet A queue is waiting, droplet A-B merged, new droplet leaves the merging point, and the rapid refilling of the empty spot by the second droplet A in the queue. The green, blue and yellow droplets indicate the droplets A, droplet B, and the newly merged droplet, respectively.

**Influence of the electric parameters** The influence of AC frequency is first investigated. Its influence on droplet electrocoalescence in a *nonuniform* field is unclear. In a *uniform* AC field, Teo et al. [109] pointed out that electrocoalescence efficiency only slightly increases with increasing frequency. In contrast, Anand et al. [110] and Priest et al. [111] found that the electrocoalescence efficiency is independent of the frequency or even the type of waveform (DC or AC). For the nonuniform AC field, as we used here, the study on the frequency influence on electrocoalescence is rarely found. We applied two frequencies- 100 Hz and 10,000 Hz- with the same root mean square voltage ( $V_{RMS} = 80V$ ) on the same chip. In a DI water-in-oil system, at 100Hz the droplets almost do not merge, with time, the pressure builds up slowly and more droplets tend to exit the WL. At 10, 000 Hz, the moment the signal is turned on, the droplets A start to exit the WL as if they experience a strong pulling force. While exiting, they also merge with other droplets A in the queue. In our case, increasing the frequency significantly enhances the merging efficiency (and even too much).

This frequency dependency could be explained with the Clausius-Mossotti factor  $K_e$ , which exists in both the dipoles interaction equation and the DEP equation (Eq.6.1, 6.2). We know that at lower and higher frequency, the real part of  $K_e$  has  $Re(K_e(\omega \rightarrow 0)) = \frac{\sigma_1 - \sigma_2}{\sigma_1 + 2\sigma_2}$  and  $Re(K_e(\omega \rightarrow \infty)) = \frac{\epsilon_1 - \epsilon_2}{\epsilon_1 + 2\epsilon_2}$ , respectively. Here,  $\sigma_{1,2}$  and  $\epsilon_{1,2}$  are the conductivity and permittivity of the droplet and the oil medium, respectively. As the conductivity of DI water and fluorinated oil is similar ( $5.5e-8 S/m$  vs.  $4.5e-8 S/m$ ),  $K_e$  at lower frequency is close to zero ( $K_e = 0.06$ ). Both forces are therefore quite weak (still positive). In contrast, the permittivity contrast of the two materials is significantly (80 vs. 5.8). At higher frequency ( $\omega \rightarrow \infty$ ) when the permittivity difference is more important,  $K_e$  is increased ( $K_e = 0.81$ ), the electrocoalescence effect from both mechanisms are prominent. For better controllability and to reduce the power consumption, we decided to work under a frequency of 100 Hz from now on, and improve the electrocoalescence efficiency and selectivity with other means. We have compared the sine shape and square shape waveforms, which have no influence on the results.

## Chapter 6. Deterministic droplet pairing and merging

---

Influence from the other parameters is shown in Fig.6.4. For each droplet B that passes the junction, we can obtain four possible results: the droplet B does not merge with droplet A (no merging); one droplet A exit before the corresponding droplet B arrives (exit); the droplet B merges with the first *and* the second droplet A in the queue (AAB merging), and finally the ideal case where the droplet B merges with *only* the first droplet A (AB merging). Each column sums up at 100%, representing all events of a passed droplet B. From a), at 100Hz we applied five different  $V_{RMS}$  on the electrodes for DI water droplets. With increasing  $V_{RMS}$ , we observed decreasing ratio of no merging events and enhancing AB merging. However, when  $V_{RMS}$  is too high, AAB merging is also enhanced, decreasing the selectivity. At 700V, the whole train of droplets A in the waiting line is merged into a single phase and the device functions as a pico-injection operation. This experiment shows that increasing the voltage will enhance the merging behavior, but there is a limit constrained by the selectivity and the requirement to preserve all droplets.

b) shows that when droplets B pass too fast, the AB merging probability is significantly reduced, which unfortunately indicates an upper limit for the merging throughput for the current device. This is probably due to not enough electrocoalescence efficiency which requires certain droplet A-B contact time for electrocoalescence to happen.

c) is when we change the droplet medium from DI water to cell medium DMEM (Dulbecco's Modified Eagle Medium) that has higher conductivity ( $1.6S/m$  vs.  $5.5e-8 S/m$ ). We discovered the following changes: 1. we start to see droplets merging in a "(droplet A) head-to- (droplet B) head" manner, i.e., droplets start to merge from the moment when they just meet, instead of merge in the last moment with '(droplet A) head-to- (droplet B) tail" as in the case of DI water; 2. the electrocoalescence happens with a lower  $V_{RMS}$  value, for example, 40 V at the optimal condition compared to 177 V at the optimal condition for DI water ; 3. the selectivity is significantly increased, with 88.2 % of AB merging and zero AAB merging event, for a total of 166 droplet B that has passed the merging area. These changes show an improvement in electrocoalescence efficiency with increased conductivity. This phenomenon can be explained by the Clausius-Mossotti factor  $K_e$ . At a lower frequency, as we are using here, the conductivity difference between the droplet and the oil medium has increased the value of  $K_e$ , and so the effect of electrocoalescence. While the enhancement of electrocoalescence efficiency should be true for all droplets A, the reduction of AAB merging frequency is surprising. It is as if the first droplet A has "absorbed" the main effect, increasing the total selectivity.

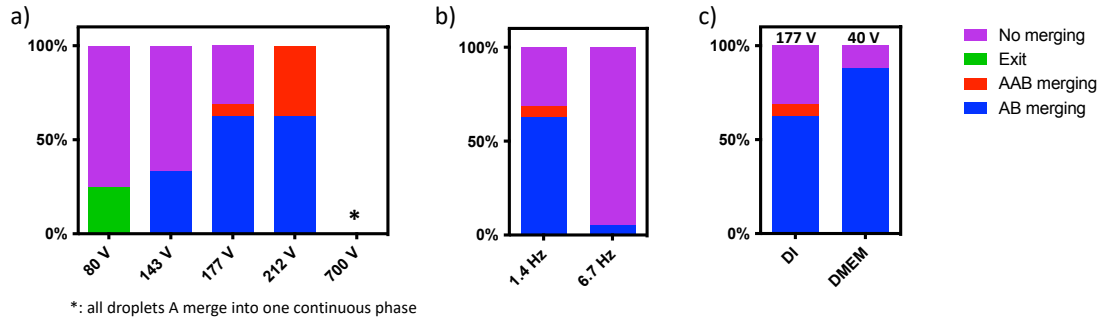


Figure 6.4 – **Droplet merging performances under different electric parameters.** The number of total events counted is equal to the number of droplet B that passed the junction. All events sum up to 100%. The number of events per experiment varies from 20 to 290, with most of the experiments having above 60 events. a) For DI droplets the electrocoalescence performance under AC frequency of 100 Hz at different  $V_{RMS}$ . b) For DI droplets the electrocoalescence performance under AC frequency of 100 Hz at  $V_{RMS} = 177V$ , under different flow condition. The droplet B passing frequency is shown on the x-axis. c) The electrocoalescence performance under an AC frequency of 100 Hz for DI as well as DMEM.

## 6.4 Fabrication and Experimental

### 6.4.1 PDMS chip fabrication

The device used in this study is made of PDMS. The design of the channel is conducted in AutoCAD, where the 2D microfluidics channel shape for the fluidic elements, as well as the electrode, is defined in a 2D design file. We made the PDMS mold out of a silicon wafer patterned with photolithography using this 2D design file. The fabrication of the silicon mold and PDMS replica is the same as in chapter 2.

### 6.4.2 Electrode fabrication

With the PDMS chip ready, the fabrication of the electrodes is the last step for chip fabrication. It relies on using an alloy wire with a low melting temperature and a diameter fitting well with the holes in the microfluidic chip punched accordingly. At the above-melting-point temperature, the low melting point alloy is filled into PDMS channels under the capillary effect. This fabrication technique eliminates the alignment effort compared to a planar electrode patterned on a glass slide (which needs to be aligned and sealed with the PDMS), and is thus time- and- cost-effective. The steps in making the electrodes for one chip are the following:

1. Cut two 6 mm long pieces of soft tubing and insert a hollow metal stick in it. The rough part of the metal stick should be kept in the open air while the smooth part should be partly isolated by the soft tubing. This metal stick will later be connected to the melted

## Chapter 6. Deterministic droplet pairing and merging

---

electrode as a connection pin for operation.

2. Turn on the hot plate and wait until it reaches a stable temperature of 90°C.
3. Take a 2 mm piece of the metal wire and insert it into the hole of one electrode.
4. Place the chip on the hot plate for 30 seconds and start to push the melted metal wire with the hollow metal stick previously prepared, and with the rough part of it. Push until it reaches the end of the pinhole.
5. Inspect the continuity of the electrodes under the optical microscope and with a digital multimeter checking the resistance

### 6.4.3 Experimental control

The flow rate is controlled via a pressure source and a pressure regulator. The AC electric signal is generated with a function generator and is amplified by Kepco BOP-1000M with a gain of 100 V/V. Before applying to the electrode, the  $V_{RMS}$  value is obtained from a digital multimeter.

## 6.5 Discussion

### 6.5.1 The optimal performance and current limitation

In summary, the optimal performance is shown in Fig.6.4c, achieved with DMEM as the aqueous phase, the fluidic elements being “J + A (25) +B + WL”, the electrode configuration shown in (Fig.A.5d) and with a 100 Hz AC frequency at  $V_{RMS} = 40V$ , with a merging point design of “P1” (see Appendix.A.4.2). For a total of 166 merging events, nearly 90% of the AB merging is performed at the first time a droplet B has passed the junction. During the entire process, no AAB merging nor droplet A existing events happened. This guarantees 100% correct pairing for droplet A. The droplet merging ended when the preloaded droplets A in the waiting line and in the storage chamber are finished (no new supply of droplet A in this experiment). The droplet merging is performed at a frequency of 1.3 Hz.

There are certain limitations of the current device. First, there is an upper limit for the merging throughput, as shown in (Fig.6.4b). It shows that under current electrocoalescence sensitivity if droplet B flows too fast, droplet merging does not happen. While increasing voltage will enhance the electrocoalescence efficiency, there is an upper limit above which the droplet A-A merging would start to happen. Therefore, this issue fundamentally is a constraint from the selectivity that would need to be improved. Strategies like fabricating planer electrode pair underneath the droplet pair could be an option. We also observed the limit coming from the speed of releasing droplet A into the main channel after the merging. Currently, the orthogonal crossing design between the waiting line and the main channel requires droplet A to turn 90 degrees during release, which under high speed would cause a re-breakup at the corner. In

addition, while the vacancy of the forefront droplet A can be automatically re-filled by the next one in the queue, it requires some time to finish this process, which is non-negligible compared to the time intervals between the arrivals of two droplet B if the interval is very short. Therefore, we have limits from three aspects: the electrocoalescence selectivity, the droplet A releasing easiness, and the droplet A refilling rate, which constraint the throughput of this approach. By optimizing the electrocoalescence sensitivity and selectivity, flow condition, and channel geometry, this limit might be eased but would require further development. Currently, this approach is only suitable for lower throughput applications. The reproducibility of our approach is also an issue. The efficiency of droplet AB merging is not only dependent on the electric configuration but also on the fluid condition. We have observed that a higher pressure drop in the waiting line helps the electrocoalescence as if the applied voltage has been increased. In reality, the variation of pressure drop along the waiting line is common, which leads to different electrocoalescence efficiencies under the same parameters. A main source of variation is the geometry defects from the chip fabrication, especially when it comes to the high aspect ratio pillar array along the waiting line. After improving our fabrication method, we observed much less variation in the fluid and merging behavior of the droplets. It shows that when the fluid preparation is a key to success in a passive method, such a method is sensitive to the resistance changes and thus is vulnerable to geometrical variations. This raises a higher requirement for fabrication quality.

### 6.5.2 Comparison with other merging techniques

There exist different droplet merging strategies. The ones that can be used for *pre-generated* droplet merging for pairing different types of droplets are mainly two strategies. One strategy uses different-sized wells to trap in the same place different types of droplets to form the desired droplet pairs followed by the electrocoalescence [32, 96, 112]. This technique uses sequential loading of droplets, whose throughput per batch is determined by the number of wells on the device, which is usually at the scale of a few hundred. To ensure the pairing efficiency, all wells need to be occupied which normally requires the loading of excessive droplets, and the well dimensions are tailored to each size of the droplets, which needs to be monodisperse. Compared to this method, our method operates in continuous flow thus the throughput is proportional to the operation time. It does not require a specific range or monodispersity of the droplet sizes. Another merging method is based on the continuous and alternating re-injection of two sizes of droplets, each representing one distinct type. When the smaller droplet (moving faster) catches with the larger droplet, electrocoalescence happens during the passing of these droplet trains through the electric-field-ON channels [113, 114, 115]. Here, the synchronization effort is required to make sure exactly one small droplet is paired with exactly one large droplet during re-injection. The latter is usually achieved with dense packing and a controlled release of the droplets, which requires flowrate tuning and droplet size monodispersity. To reduce synchronization errors, the larger type of droplet (e.g., containing barcode bead) can be injected with a higher frequency to reduce the chance of two or more smaller types of droplets (e.g., containing single cells) getting merged

## Chapter 6. Deterministic droplet pairing and merging

---

with one big droplet. This approach might provide a higher throughput than our approach. However, in the case of rare droplets, the time it is required for flow rate tuning might already cause severe loss of the precious droplets samples.

As compared with the existing two methods, our method can ensure the merging efficiency of one type of droplet with the “no pairing, no collection” strategy. All droplets A will be merged with one and only one droplet B, this is extremely important when it comes to rare sample analysis. For both of the previous approaches, specific droplet sizes are required, with a narrow size distribution tolerated. This requirement is not relevant in our case- we just need to make sure that droplets A and B can be confined by the waiting line channel and the main channel, respectively. Size variation among the droplets is totally allowed, which could be quite common in the case of pre-generated droplets. What’s more, the well-assisted and the in-flow synchronization approaches are both designed for the pairing of two types of droplets. Our approach can be easily extended to pairing and merging three or more distinct types of droplets (by adding waiting lines). The operation time is the same as in the case of merging two droplets. To give an example, with current throughput, to obtain 1000 double-merged or multi-merged droplets always requires a bit more than 2 hours of operation.

### 6.6 Conclusion and outlook

In this chapter, we introduced a novel droplet pairing and merging approach. Due to the waiting line concept, deterministic droplet pairing is realized in the continuous flow but without real-time flow rate tuning and synchronization. The pairing efficiency for the droplet type in the waiting line is guaranteed. Both fluid configuration and electrocoalescence configuration are important for the success of this approach. The former prepares droplets in the waiting condition, the latter ensures efficient and selective droplet merging. We have optimized both parts and obtained a good merging performance using the optimized parameters. Currently, this approach is limited to lower throughput and thus might be more suited for the pairing and merging of precious droplet samples. For the moment, droplets generated in situ are used for proof of concept. In the future, we expect to switch to those pre-generated droplets created from the deterministic single-cell/particle generation methods introduced in the previous chapters.

# 7 Summary and Conclusion

## 7.1 Summary

### 7.1.1 Summary of results

In this thesis, we targeted a common and difficult issue of droplet microfluidics concerning the random single-cell encapsulation, known as the Poisson limit. Specifically, we aimed to provide new solutions for building multi-object single-cell assays that are of extreme interest in clinical and research applications but are the worst-hit area by the Poisson limit. Towards this end, the following achievements were obtained in this study:

1. We made a discovery of a new droplet breakup regime on a famous type of microfluidics geometry: microfluidics T-junctions. This discovery enables our later technological development.
2. We analytically, experimentally, and numerically resolved the new droplet breakup mechanism, which included finding the origin of the droplet instability, developing a geometrical rule for creating the instability with any T junction, and numerically modeling the droplet breakup dynamics (at lower  $Ca$  range).
3. After understanding the new regime, we further studied the competition between the conventional and the new droplet breakup regimes in the same geometries and obtained a mechanical understanding of the regime transition.
4. Based on points 1 to 3, we developed the first deterministic single-cell encapsulation strategy overcoming the Poisson limit for a single object: Cell Triggered Splitting (CTS). Utilizing the competition between breakup regimes, CTS automatically creates different droplet sizes associated with cell occupancy, which enables the passive acquisition of droplets containing single cells.
5. We realized two variations of CTS with different chip designs and working principles, i.e., CTS-1 and CTS- 2. We characterized their different performances, which would suit

different application scenarios.

6. We developed the second deterministic single-cell encapsulation strategy for overcoming the Poisson limit: Single Cell Differentiated Trajectory (SCDT). We proposed a simple mechanism to distinguish droplet trajectories based on their single-cell contents. Influences of droplet size and speed on the performance are discussed. Such a trajectory-differentiating mechanism can potentially be applied to droplet sorting based on other properties.
7. We developed a new fabrication strategy that achieves precise and dimension-limited 3D geometry within PDMS chips.
8. Using point 7, we developed the third deterministic single object encapsulation strategy using a passive blocking mechanism: K blocking. The Poisson limit is avoided from the beginning using this method. The passive “rule-to-success” is discussed, and two working modes are demonstrated.
9. Finally, towards building dual- or multiple- object single-cell assays from deterministically obtained single-object droplets, we developed an “In-flow” droplet merger with a waiting line concept. Efficient one-to-one merging of two types of droplets is realized after optimization. The waiting-line principle guarantees the correct pairing of the waiting-type droplets, which is of particular interest for rare and valuable cell samples.

### 7.1.2 Deterministic single object encapsulation

This section is dedicated to the acquisition of single-object droplets, mentioned in the above summary in points 4 to 8. It aims to summarise and compare the features of all deterministic single-object encapsulation tools that have been developed in this thesis (i.e., from Chapters 2 to 5) to give implications for future applications.

- **(CTS)** It adopts a post-encapsulation secondary breakup-mediated droplet sorting strategy, requiring three steps: random cell encapsulation, size difference creation, and size-based sorting. The CTS method is a highly deterministic method due to the “no cell, no splitting” principle and the significant droplet size difference leading to efficient sorting (>98% cell loading rate in the smaller droplets + 100% small droplet purity after sorting). Both CTS-1 and CTS-2 can provide *label-free* single cell sorting at a throughput higher than the currently reported methods [116, 117, 118, 119, 120], with CTS-1 reaching an ultra-high throughput of 3100 Hz.
- **(SCDT)** It adopts a post-encapsulation direct droplet sorting strategy, requiring two steps: random cell encapsulation and direct sorting. SCDT method is the first content-based droplet sorting method with single-cell resolution, with the potential to automatically distinguish the singlets, doublets, and multiplets. It also provides easy scaling of the product droplet size (i.e., scaling from the initial generation).

- **(K blocking)** It adopts a *passive* droplet on-demand generation strategy, requiring single step of particle-triggered droplet generation. More suited for rigid particles, K blocking is the first *passive* on-demand droplet generator (Fig.1.6), which avoids random encapsulation completely.

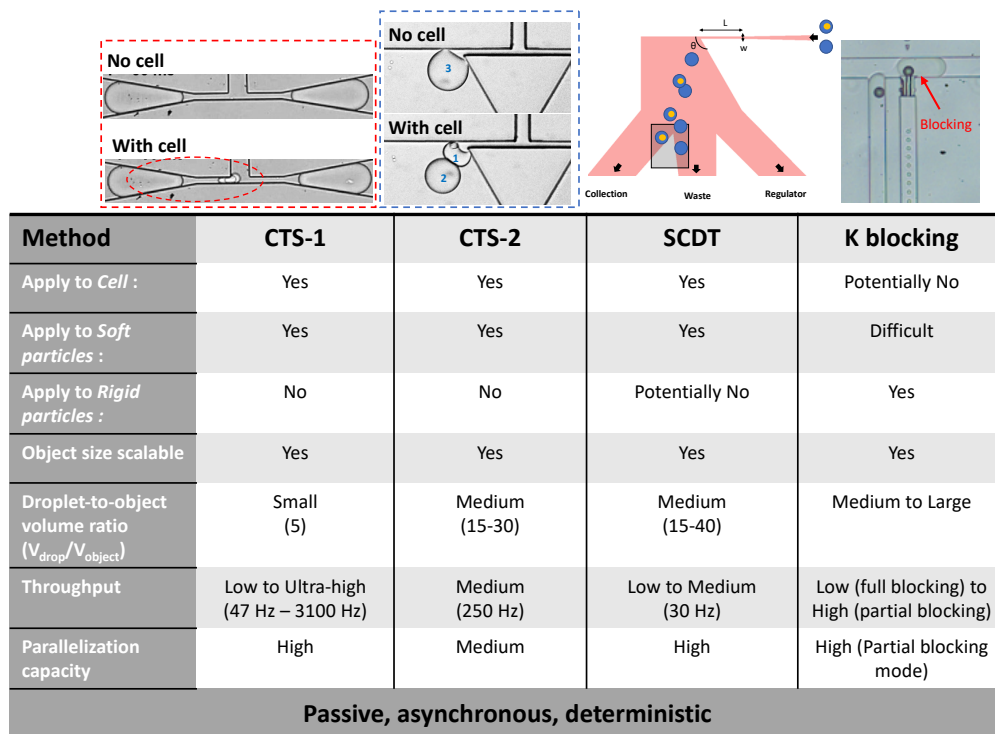


Figure 7.1 – Comparison of different single-object (cell/particle) encapsulation techniques developed in this work

More features of these techniques can be found in Fig.7.1. With that, we can now claim a full set of single-particle encapsulation tools covering almost all single-object encapsulation applications. This includes solutions for fragile cells, different-sized deformable particles and rigid particles, and obtaining product droplets with varying absolute sizes and droplet-to-object volume ratios. A wide range of sample volumes can be targeted with adjustable throughput. The choice of technique can be made based on the application requirements. All these technologies are *deterministic*, as the distinguishing actions (e.g., droplet splitting, sorting, generation, etc.) are only “triggered” by the object itself. They are *passive*, indicating a simple setup with no costly or complex (active) components. They are also *asynchronous*, meaning flowrate tuning is avoided and the “plug and play” operation is enabled for robustness and simplicity.

### 7.2 Conclusion and Outlook

Today, single-cell study has great potential in a good variety of clinical and research applications. Droplet microfluidic providing well-defined micro-compartments with manipulation flexibility, high throughput, relative simplicity, and low cost, excels from other single-cell platforms like valves, microwells, and various types of traps. Over 20 years, while droplet microfluidics has rapidly developed, Poisson (random) cell encapsulations remain a fundamental issue. It demands high dilutions of cells to limit the noise caused by the droplets containing multiple cells. This severely affected the ever-growing multi-object single-cell assays requiring distinct multiple objects in one droplet. For these assays, the necessity of diluting each object leads to less than 1 % of the droplets having the correct combinations, causing acute cell loss, biased or missed results, and the incapability for rare cell samples. To avoid this issue, the existing techniques using simultaneous encapsulation of multiple objects are incompetent—the passive methods require critical synchronization between the arrival of all objects and the droplet generation frequency and are yet non-deterministic [121, 122]; The active methods require sophisticate and expensive elements and thus are limited by cost, complexity, and throughput[20]. We proposed that a perfect solution to the above issue would be a simple and robust creation of droplets containing single objects, followed by deterministic merging of these droplets with desired ratios. This strategy gives full flexibility and accuracy for the final multi-object droplet assays. At the end of this thesis, we conclude that we have developed enough tools to achieve the goal. These include a full set of deterministic single-object encapsulation tools for the first step and a deterministic droplet merger for the second step. At this stage, both steps of microfluidics techniques are developed separately; combining the two steps to building the final multi-object assays is of high interest and should be further implemented. In addition, while all the introduced devices and fabrication methods are useful techniques themselves, they require biological validation to prove their application relevance.

The future of single-cell screening/characterization involves ever-larger sample size, requiring the development of high throughput methods. While our droplet merger is currently limited by lower throughput, there is a known droplet merging approach that compensates for this limit. This merging strategy is based on the alternating re-injection of two types of droplets each having one distinct size. When the smaller droplet (moving faster) catches with the larger droplet, a droplet pair is formed and electrocoalescence happens during the passing of the droplet pairs through the electric-field-ON channels [113, 114, 115]. This method allows high-throughput (500Hz[114]) droplet merging with sufficient one-to-one pairing accuracy. With that, our various deterministic single-cell encapsulation tools capable of simple and high-throughput acquisition of single-cell droplets can play a better role in multi-object droplet assays. One example is to use CTS to produce a massive number of small droplets containing cells and large droplets containing barcode beads, then perform the merging to achieve high-accuracy and high-throughput ScRNA sequencing. Currently, according to 10X genomics company, ScRNA sequencing is performed at a maximum rate of 60k cells per run with a maximum of 30% of cells being captured. Following the above strategy, ScRNA sequencing

can be performed at 1800k per hour with significantly improved cell capture efficiency thanks to the exclusion of empty droplets. We would have an ever larger capacity to describe the full picture of a complex cell system with minimal cell loss, a request to study developmental biology (e.g., cell lineage), oncology, immunology, immuno-oncology, etc.

Another example is to use CTS to produce small and large droplets for two distinct types of cells and merge them to perform label-free and high throughput cell-cell assays. Indeed, while cell-cell interaction is essential to many physiological processes, studying cell-cell interaction is historically relatively low throughput, relying on mechanoforce analysis, microscopy imaging, etc. In comparison, droplet microfluidics with high throughput, well-defined cell environments, and cell retrieval capacity, is a promising tool. However, acquiring two cells in one droplet is rather difficult due to the Poisson limit. Our approach would significantly enhance the poor encapsulation performance of dual Poisson distribution. One application that benefits from this is TCR-T cancer immunotherapy. Using the depicted cell-cell droplet assays, the identification of rare potent T cells from massive patient-derived T cells can be performed via high throughput screening of the T cell and (engineered) antigen-presenting cell (APC) pair. The activation signal induced by specific cell-cell interaction indicates which T cell is of interest that can be potentially retrieved for therapeutic development. This application could only be enabled by efficient and high throughput cell-cell droplet assays described above. Note that as the activation signal is already fluorescence-based (typical readouts for cell-cell assays), our approach's label-free feature (i.e., no artificial fluorescence staining) also plays an essential role as compared to other high throughput but fluorescence-based single-cell droplet acquisition methods.

For rare or low-input cell samples, the throughput is not a concern, but the accuracy is. The combination of SCDT and "In-flow" offers maximum accuracy in this case. After realizing the highly efficient cell-loaded droplet sorting with SCDT, we should further exploit its single-cell resolution power, distinguishing single-cell droplets from dual-cell and multiple-cell droplets. Currently, obtaining a population of droplets containing exactly one cell is a pain point in droplet microfluidics. It is not easy whether in passive or active manners; however, it is critical for assay accuracy. Another critical aspect concerns the precision of droplet pairing and merging. Our "In-flow" method guarantees the perfect one-to-one pairing and merging for the rare/precious type of droplets. One can imagine using SCDT to generate a pure droplet population containing single rare cells and another population with single barcode beads, which are then fed to the "In-flow" system for capturing each cell with a barcode bead for RNA sequencing. Combining the two offers the superior capacity to analyze every rare cell. Some relevant rare or low-input cell samples requiring transcriptome analysis include patient tumor samples, embryonic stem cells (150 cells), circulating tumor cells, individual tissue samples, etc. The next step would be to realize these biological applications. Improving the current throughput (i.e., processing 1000 cells within 2 hours) is also interesting for future work. Indeed, with a similar working principle as pico-injection, even if we can not reach the same throughput as a few kHz due to the additional requirement of preserving the waiting-line droplets, there is still a large space for improving from the current throughput of 2Hz. In

## Chapter 7. Summary and Conclusion

---

addition, cell-cell interrogation has long been a critical appeal in biological studies but is still dependent on fluorescence readout. By adding one more waiting line to the “In-flow” system, one can easily construct “cell A - cell B - barcode bead” assays to extract and monitor the transcription information during the cell-cell communication/interaction processes. We believe that the high precision that can be achieved in any two-object (cell) droplet assays is a particularly valuable feature in the era of single-cell study.

In addition to the technological development of droplet microfluidics to strengthen its role as an efficient and versatile single-cell platform, we have also contributed to the fundamental droplet study for the physics society. Over 20 years, T junctions have been known as one of the most used droplet creation geometries, and the creation of droplets is only achieved with hydrodynamic-forces-driven mechanisms. In this thesis, we demonstrated that the surface-tension-driven mechanism is also possible with T-junctions. It leads to a completely different “lateral breakup” phenomenon that can compete with the hydrodynamic-force-driven mechanism- the first microfluidics geometry with both breakup mechanisms. A simple analytical rule was proposed as a design principle for the followers, and we developed the first numerical modeling framework suitable for the lateral breakup regime in T-junction. A new transition is introduced for the community. Specifically, in a T-junction from vanishing  $Ca$  to higher  $Ca$ , the breakup transition is no longer from non-breakup to central breakup but is rendered from lateral breakup to central breakup. This changes the paradigm of droplet modulation by introducing new functionalities, including real-time *active* control of different droplet sizes and compositions and the *passive* object-triggered creation of new droplets. We have shown that all these are enabled by shifting from a conventionally adopted shallow channel geometry to a deep channel geometry. It is interesting to study more of this less-explored domain in microfluidics. Indeed, one benefited example is step-emulsification, which by adopting the deep channel geometry can now be performed in simpler geometries with a single height. We expect more to be explored in the field of deep-channel microfluidics.

This thesis includes the theoretical and technological development of droplet-based microfluidics. We expect the obtained results to greatly contribute to this field’s advancement. More biological validation is expected in future work.

# A Appendix

## A.1 Mathematical modeling of the inflation of the lateral pockets at low Ca

Hereafter, we fully characterize the inlet and outlet gutters regime of the droplet (shown in **Figure 2.3a**), as they couple with equation (2.7) and (2.9) for the pocket dynamic through the boundary conditions and the conservation of the droplet volume. We then show that they constitute all together a closed system that is made non-dimensional, and after some mathematical rearrangements, can be directly integrated in time.

Let  $R_g^{(i)}(s, t)$  designate the radius of the gutter in the inlet channel (see **Figure 2.3a**) whose internal coordinate is  $s \in [0; L_i(t)]$ , purely along the  $x$  direction. Solving eq.(2.4) subject to  $R_g^{(i)}(0, t) = F_i$  leads to

$$R_g^{(i)}(s, t)^3 = F_i^3 - q_i(t)As \quad (\text{A.1})$$

where  $q_i(t)$  is the inlet gutter flow rate. By continuity, we can express it in terms of  $k(\eta, t)$  using eq.(2.8) as

$$q_i(t) = \frac{4\gamma}{r_{h,S}[z(0, t) = h/2]} \frac{\partial k(0, t)}{\partial \eta}, \quad (\text{A.2})$$

(we recall that  $\eta = 0$  designates the opening of the pocket at the junction and  $\eta = L_p(t)$  its closure (see **Figure 2.3a**). The four boundary conditions for  $z(\eta, t)$  and  $k(\eta, t)$  write  $z(0, t) = z(L_p(t), t) = h/2$ ,  $k(0, t) = 1/R_g^{(i)}(L_i(t), t) - 2/w_o$ , and  $k(L_p(t), t) = 0$ . The outlet gutter, of length  $L_o(t)$  (see **Figure 2.3a**), has a radius  $R_g^{(o)}(\alpha, t)$  whose internal coordinate is  $\alpha \in [0; L_o(t)]$ , purely along the  $y$  direction. The radius  $R_g^{(o)}(\alpha, t)$  is characterized by solving eq.(2.4) subject

## Appendix A. Appendix

to  $R_g^{(o)}(0, t) = w_o/2$  (since  $k(L_p(t), 0) = 0$ ) :

$$R_g^{(o)}(\alpha, t)^3 = \left(\frac{w_o}{2}\right)^3 - q_o(t)A\alpha, \quad \text{where} \quad q_o(t) = \frac{4\gamma}{r_{h,S}[z(L_p(t), t) = h/2]} \frac{\partial k(L_p(t), t)}{\partial \eta} \quad (\text{A.3})$$

Its length  $L_o(t)$  is easily determined by imposing  $R_g^{(o)}(L_o(t), t) = F_o$ . As will become clear in a moment, the problem is closed by imposing of conservation of the total volume of the droplet. From now on quantities are made non-dimensional, by  $h$  in space and  $\mu h/\gamma$  in time

$$\begin{aligned} h(\tilde{s}, \tilde{\eta}, \tilde{\alpha}) &= (s, \eta, \alpha), & \frac{\mu h}{\gamma} \tilde{t} &= t, & h^2 \tilde{S} &= S, & \frac{h^2 \gamma}{\mu} \tilde{q} &= q, & \frac{1}{h} \tilde{k} &= k, & h \tilde{z} &= z, \\ \frac{\mu}{h^4} \tilde{r}_{h,S} &= r_{h,S}, & \text{and} & & \frac{\gamma}{\mu} C a &= U. \end{aligned}$$

Equations (2.7) and (2.9) thus non-dimensionalized, they are then put in the form of a classical conservation law for  $\tilde{z}(\tilde{\eta}, \tilde{t})$  and  $\tilde{k}(\tilde{\eta}, \tilde{t})$ :

$$\begin{bmatrix} 1 & 0 \\ 0 & 0 \end{bmatrix} \frac{\partial}{\partial \tilde{t}} \begin{bmatrix} \tilde{z} \\ \tilde{k} \end{bmatrix} + \frac{\partial}{\partial \tilde{\eta}} \begin{bmatrix} -B \frac{1}{r_{h,S}[\tilde{z}]} \frac{\partial \tilde{k}}{\partial \tilde{\eta}} \\ -\frac{\partial \tilde{z}}{\partial \tilde{\eta}} \left[ 1 + \left( \frac{\partial \tilde{z}}{\partial \tilde{\eta}} \right)^2 \right]^{-1/2} \end{bmatrix} = \begin{bmatrix} 0 \\ \tilde{k} \end{bmatrix}, \quad \text{for } 0 \leq \tilde{\eta} \leq L_p(t) \quad (\text{A.4})$$

where all the tildes have been dropped and  $B = 1/w_o$  is a constant (it is understood that  $L_p$  and  $w_o$  have been made non-dimensional by  $h$ , etc...). System (A.4) is re-written under the change of variable  $\xi = \eta/L_p(t)$  in order to be solved over the time-independent domain  $0 \leq \xi \leq 1$ , which is significantly more convenient. The partial derivatives are transformed as  $\partial_{\tilde{t}} \rightarrow \partial_t - (d_t L_p) L_p^{-1} \xi \partial_\xi$  and  $\partial_{\tilde{\eta}} \rightarrow L_p^{-1} \partial_\xi$ :

$$\begin{bmatrix} 1 & 0 \\ 0 & 0 \end{bmatrix} \frac{\partial}{\partial t} \begin{bmatrix} \bar{z} \\ \bar{k} \end{bmatrix} + \frac{\partial}{\partial \xi} \begin{bmatrix} -\frac{dL_p}{dt} \frac{1}{L_p} \xi \bar{z} - \frac{B}{L_p^2} \frac{1}{r_{h,S}[\bar{z}]} \frac{\partial \bar{k}}{\partial \xi} \\ -\frac{1}{L_p^2} \frac{\partial \bar{z}}{\partial \xi} \left[ 1 + \frac{1}{L_p^2} \left( \frac{\partial \bar{z}}{\partial \xi} \right)^2 \right]^{-1/2} \end{bmatrix} = \begin{bmatrix} -\frac{dL_p}{dt} \frac{1}{L_p} \bar{z} \\ \bar{k} \end{bmatrix} \quad (\text{A.5})$$

where  $z(\eta, t) = \bar{z}(\xi, t)$ , then  $k(\eta, t) = \bar{k}(\xi, t)$ . Under this change of variables the flow rate  $q(\eta, t) = \bar{q}(\xi, t)$  occurring inside the pocket, and the flow rates  $q_i(t)$  and  $q_o(t)$  occurring inside the inlet and outlet gutters, respectively, express :

$$\bar{q}(\xi, t) = \frac{4}{r_{h,S}[\bar{z}(\xi, t)] L_p(t)} \frac{\partial \bar{k}}{\partial \xi}(\xi, t), \quad q_i(t) = \bar{q}(0, t) \quad , \text{and} \quad q_o(t) = \bar{q}(1, t).$$

The boundary conditions of the system (A.5) are re-written :

$$\begin{aligned} \bar{z}(0, t) &= 1/2, & \bar{z}(1, t) &= 1/2, \\ \bar{k}(0, t) &= \left[ (F_i^3 - q_i(t) A L_i(t))^{-1/3} - \frac{2}{w_o} \right], & \text{and} & \bar{k}(1, t) = 0. \end{aligned} \quad (\text{A.6})$$

## A.1. Mathematical modeling of the inflation of the lateral pockets at low $Ca$

(with the non-dimensional  $A = 3C/(4-\pi)$ ). A third equation is necessary for the third unknown  $L_p(t)$ , and the problem is closed by imposing the volume conservation  $V(t) = V(0)$ . Let  $V_g^{(i)}(t)$  designate the volume of the part of the droplet contained in the inlet channel and where a gutter is present (i.e. for  $0 \leq s \leq L_i(t)$ ); the volume of the rear cap is in addition  $V_{cap}^{(i)}(t)$ . Accordingly, let  $V_g^{(o)}(t)$  be the volume of the part of the droplet contained in one of the two outlet channels and where a gutter is present (i.e. for  $0 \leq \alpha \leq L_o(t)$ ); the volume of one front cap is in addition  $V_{cap}^{(o)}$ . We recall that the expression for the cross sectional area of the discrete phase in the pocket region is  $S[z(\eta, t)] = (\pi - 4)w_o^2/4 + 2w_o z(\eta, t)$ , such that it is associated to a volume contribution in a outlet channel of  $\int_0^{\eta=L_p(t)} S[z(\eta, t)] d\eta$ . Eventually :

$$\begin{aligned} V(t) &= 2V_{cap}^{(o)} + V_{cap}^{(i)}(t) + V_g^{(i)}(t) + 2V_g^{(o)}(t) + 2 \int_0^{\eta=L_p(t)} S[z(\eta, t)] d\eta \\ &= 2V_{cap}^{(o)} + V_{cap}^{(i)}(t) + V_g^{(i)}(t) + 2V_g^{(o)}(t) + 2L_p(t) \left[ \frac{(\pi - 4)w_o^2}{4} + 2w_o \int_0^{\xi=1} \bar{z}(\xi, t) d\xi \right] = V(0) \quad (\text{A.7}) \end{aligned}$$

In addition, the cross sectional area the drop in a region where a gutter (of radius  $R_g$ ) is present is  $S_g^{(i,o)} = hw_{i,o} - (R_g^{(i,o)})^2(4 - \pi)$ , such that

$$V_g^{(o)}(t) = \int_{\alpha=0}^{\alpha=L_o(t)} S_g^{(o)}(\alpha, t) d\alpha = \frac{1}{Aq_o(t)} \left[ hw_o \left( \left( \frac{w_o}{2} \right)^3 - F_o^3 \right) - \frac{3(4 - \pi)}{5} \left( \left( \frac{w_o}{2} \right)^5 - F_o^5 \right) \right],$$

and we compute similarly :

$$V_g^{(i)}(t) = hw_i L_i(t) - \frac{3(4 - \pi)}{5Aq_i(t)} [F_i^5 - (F_i^3 - L_i(t)Aq_i(t))^{5/3}]$$

In order to mimic a constant-velocity progression of the droplet in the inlet channel before the rear droplet interface reaches the junction, as observed experimentally, the length  $L_i(t)$  is chosen as a ramp in time

$$L_i(t) = \begin{cases} L_i(0) - 0.85 \cdot t \cdot Ca & \text{if } 0 \leq t \leq t_J \\ 0 & \text{if } t \geq t_J \end{cases} \quad (\text{A.8})$$

which acts as a source of excitation for the system (A.5) through the boundary condition for  $\bar{k}(0, t)$  in (A.6). At the time  $t_J = L_i(0)/(0.85Ca)$  the rear droplet interface reaches the junction, and  $L_i(0)$  is such that the necking condition as shown in **Figure 2.3c** is met. The coefficient 0.85 multiplying  $Ca$  arises from the experimental data (shown in **Figure 2.3b**). The rear cap volume and curvature need also to be treated differently depending on whether  $t$  is smaller or larger than  $t_J$ ; let  $V_{cap}[h, w_i]$  designate the equilibrium volume of the rear cap, whose value is

taken from Musterd *et al.*[123] for  $H/W \leq 1$

$$\begin{aligned}
 A_{bd}[H, W] &= HW - 4 \cdot F[W, H]^2(1 - \pi/4) = HW + F[W, H]^2(\pi - 4) \\
 L_{cap}[H, W] &= \frac{W}{2} \\
 V_{cap}[H, W] &= \int_0^{L_{cap}} A_{bd}[H, W] \left(1 - \frac{y^2}{L_{cap}[H, W]^2}\right) dy = \frac{2}{3} L_{cap}[H, W] A_{bd}[H, W]
 \end{aligned}$$

Thereby the rear cap volume  $V_i^{cap}(t)$  is implemented as

$$V_i^{cap}(t) = \begin{cases} V_{cap}[h, w_i] = cst & \text{if } 0 \leq t \leq t_J \\ V_{cap}[h, w_i] \frac{\mathcal{C}_i(t)}{\kappa_i} & \text{if } t \geq t_J \end{cases} \quad (\text{A.9})$$

, where  $\mathcal{C}_i(t)$  is the rear cap curvature with  $\mathcal{C}_i(t \leq t_J) = \kappa_i$ . Above  $t = t_J$ , the rear droplet interface must undergo the incoming flow rate  $hw_iCa$  and the following equation for the cap volume is activated

$$\frac{dV_i^{cap}}{dt} = q_i(t) - Ca h w_i \quad (\text{A.10})$$

Injecting (A.9) in (A.10) leads to an evolution equation for  $\mathcal{C}_i(t)$  for  $t \geq t_J$ , and the boundary condition for the curvature at the opening of the pocket is accordingly replaced by  $k(0, t) = \mathcal{C}_i(t) - 2/w_o$  for these times.

### A.1.1 Numerical simulations

The numerical simulations are conducted by the collaborators from Laboratory of Fluid Mechanics and Instabilities (LFMI) at EPFL. Here is some of the information given by the collaborators: The closed system for the three unknowns  $\bar{z}(\eta, t)$ ,  $\bar{k}(\eta, t)$  and  $L_p(t)$  from equations (A.5) and (A.7) was solved numerically using the COMSOL Multiphysics software, based on the finite element method. More precisely, the system (A.5) is implemented directly in the "General form PDE" component of the software, and its weak form has been spatially discretized over the interval  $\xi \in [0, 1]$  using first-order polynomials (corresponding to a linear interpolation of the solution). The convergence of the numerical results with respect to the spatial discretization has been verified. Equation (A.7), enforcing the volume conservation thus depending only on time, is implemented in the "Global Equations" component. The system is marched in time using the backward differentiation formula ("BDF"), and the results are sought for 4000 discrete times uniformly distributed between 0 and  $10/Ca$ . A stopping condition has been added, such that the simulation stops running if  $\min(\bar{z}) < 1/2$ . Concerning the nonlinear, fully coupled solver, the default choices of COMSOL parameters have been found sufficient for convergence, excepted the "Jacobian update" that is set to "updated on every iteration" and the "Maximum number of iterations" that is set to 500.

### A.1.2 A scaling argument for onset of central breakup

In the spirit of reference[77], we try to obtain a scaling of the critical capillary number for central breakup to happen. Neglecting the presence of a lateral inflating pocket, the inversely proportional relationship between  $C_a^*$  and  $L_o/w_o$  might be understood as follows: after the body of the droplet has fully entered the outlet channels, we consider a threshold situation where the rear cap is flat for the observer, such that the rear cap curvature is assumed  $1/F_i = 2/h$ , although the precise value of the latter has little influence on the scaling law derived hereafter. The threshold capillary number above which a central breakup (CB) is expected is obtained by balancing the continuous flow rate arriving in the junction ( $C_a w_i h$ ), with the capillary flow rate in the four gutters located in the outlet channel ( $4(1/F_o - 2/h)/(r_o L_o)$ ), the quantity  $r_o$  being the hydraulic resistance per unit length of a gutter in the outlet channel. This leads to :

$$\frac{w_o}{w_i} C_a^* \sim \frac{4w_o}{w_i^2 h r_o L_o} \left( \frac{1}{F_o} - \frac{2}{h} \right) \propto \left( \frac{L_o}{w_o} \right)^{-1} \quad (\text{A.11})$$

For,  $w_o = 14/62$ ,  $w_i = 30/62$ ,  $h = 1$  and using eq.(2.1) for  $F_o$  and eq.(2.3) with  $R_g = w_o/2$  for  $r_o$ , we obtain  $4 \left( \frac{1}{F_o} - \frac{2}{h} \right) / (w_i^2 h r_o) \approx 5 \cdot 10^{-5}$ . However, this corresponds to a  $w_o/w_i C_a^*$  approximately four orders of magnitude smaller than experimental values.

### A.2 Nanoscribe 2.5D device Process flow

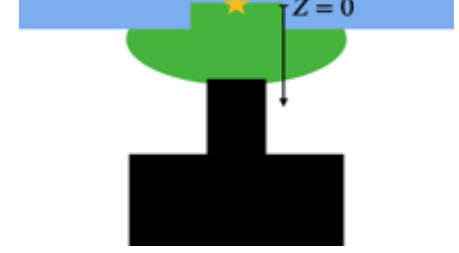
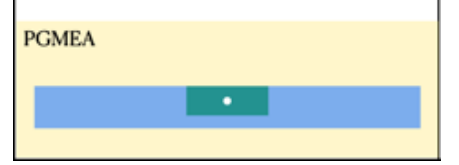
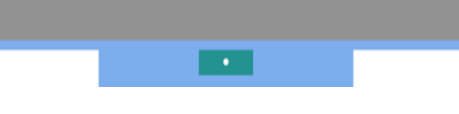
1	Si mold	
2	PDMS dispensing	
3	- Peeling PDMS. - PDMS activation for resin adhesion	
4	IP-dip resin droplet deposition	
5	3D printing with oil immersion mode	
6	Development with PGMEA and IPA	
7	Bonding for channel sealing	

Figure A.1 – Process flow for Nanoscribe 2.5D fabrication

### A.3 Theoretical development of the bead releasing condition

With the droplet moving downstream in the main channel, its rear interface will eventually touch the immobilized particle (Fig.A.2a). At this moment, two scenarios can happen:

- a. The drag force exerted on the particle through the droplet rear interface is strong enough to overcome the pinning force exerted on the particle. In this case, the droplet and the particle will together be released from the junction, and the K-blocking mechanism can function

### A.3. Theoretical development of the bead releasing condition

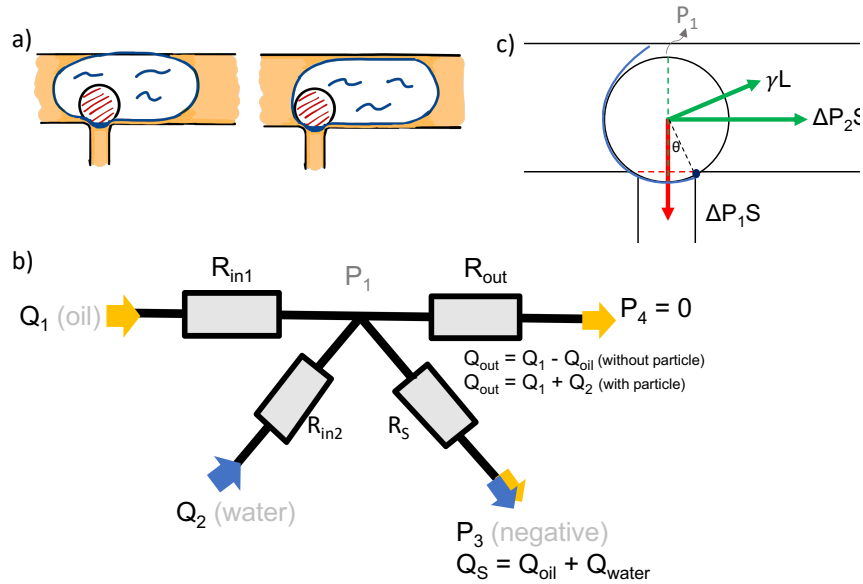


Figure A.2 – **Schematic for the design rule modeling.** a. The cross-section schematic of a free-moving droplet and droplet pinned by the trapped particle; b. The different forces exerted on the particle that is above the evacuation gate. The channel wall is shown with black lines, blue line indicates the droplet interface, a red arrow for the pressing force, and green arrows for the pushing forces; c. Modeling of the fluid circuit and the parameters used.

automatically as expected.

**b.** The drag force cannot overcome the pinning force of the particle. In this case, if the oil flow in the main channel pushes the droplet beyond its deformation limit, the droplet will detach from the particle and moves downstream without the particle (Fig.A.3); Therefore, it is necessary to understand in what condition a particle can be released with the droplet. In the following, we aim to discuss a scaling law for predicting the particle-releasing problem for a given flow condition and a given geometry.

#### The pressing force

Let's first estimate how much negative pressure is required to achieve the "water-all-in" condition. As shown in Fig.A.2b, we assume that the system is given a known oil flow rate ( $Q_1$ ) and water sample flow rate ( $Q_2$ ) from two inlets. An "water-all-in" condition is achieved by imposing a constant  $P_3$  (negative), which results in, at this stage, a total flow rate in the suction channel ( $Q_s$ ) that is consisted of some oil flow rate ( $Q_{oil}$ ) and some water flow rate representing all incoming water flow rate ( $Q_{water} = Q_2$ ). The rest of the oil flow ( $Q_{out} = Q_1 - Q_{oil}$ ) leaves the system from the main channel outlet ( $P_4 = 0$ ). Defining a constant  $c$  for the ratio of  $Q_{oil}$  and  $Q_{water}$  inside the suction channel, we then obtain the following equations for a

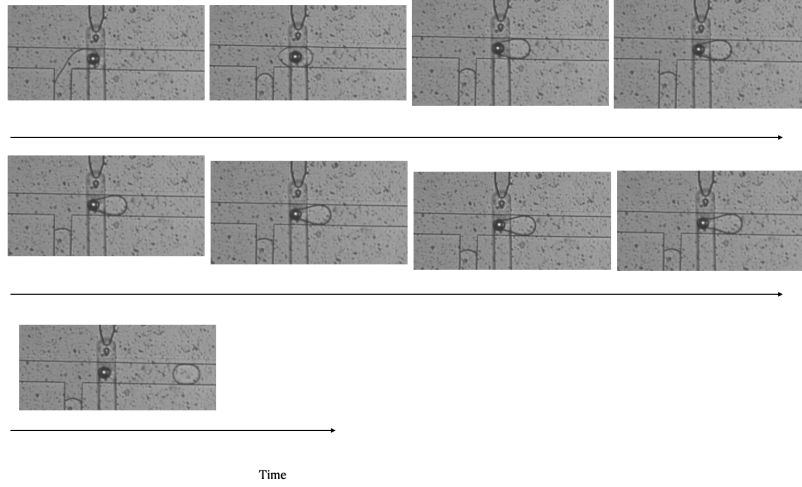


Figure A.3 – Motivation of the modeling of the particle releasing condition. Excessive suction pressure ( $P_3$ ) is applied in this case to confine the particle.

“water-all-in” system before a particle arrives:

$$\frac{Q_{oil}}{Q_{water}} = c \quad (A.12)$$

$$Q_{water} = Q_2 \quad (A.13)$$

$$\begin{aligned} P_1 - P_3 &= (P_4 + R_{out}Q_{out}) - P_3 \\ &= [R_{out}(Q_1 - Q_{oil})] - P_3 \end{aligned} \quad (A.14)$$

$$P_1 - P_3 = Q_S R_S \quad (A.15)$$

where  $P_1$  is the pressure in the main channel right above the junction. We obtain the magnitude of the negative  $P_3$  as:  $-P_3 = Q_2 [cR_{out} + (1 + c)R_S] - Q_1 R_{out}$ . For a given system (i.e.,  $R_{out}$ ,  $R_S$  is determined), if we know the minimally required value  $c_{min}$  (for preparing a “water-all-in” condition), which seems can be experimentally characterized (Appendix), we can estimate the minimally required  $(-P_3)_{min}$  at different flow conditions. If more suction pressure ( $> (-P_3)_{min}$ ) is applied, it will only cause more oil to enter the suction channel thus an increased  $c$ . We expect that  $c_{min}$  is related to the wetting property and shape of the suction channel. A more hydrophobic channel wall and a smaller gate would result in a larger  $c_{min}$ . Assuming now  $P_3$  is imposed, waiting for a particle to arrive and block the suction channel. When this happens, due to the blocking there is no pressure drop within the suction channel ( $Q_S = 0$ ); thus the pressure below the particle is immediate  $P_3$ . As now all  $Q_1$  and  $Q_2$  will flow through the main channel, the value of  $P_1$  changes to  $P'_1 = (Q_1 + Q_2)R_{out}$ . Here we omitted the influence of the particle size on  $P'_1$  for simplicity. The pressure difference across the

### A.3. Theoretical development of the bead releasing condition

particle ( $\Delta P_1 = P_1' - P_3$ ) exerts a pressing force  $\Delta P_1 S'$  that stabilizes the particle during the droplet formation process, where  $S' = \pi(\frac{l}{2})^2$  is the gate area of the suction channel ( $l$  is the gate diameter).

$$\begin{aligned}\Delta P_1 &= (Q_1 + Q_2)R_{out} - P_3 \\ &= [(1 + c)(R_{out} + R_S)]Q_2\end{aligned}\tag{A.16}$$

When  $P_3$  is determined experimentally, we use the upper expression to calculate  $\Delta P_1$ . The lower expression, on the other hand, is used for design rule consideration when  $P_3$  needs to be estimated (see below).

#### The pushing force

Before the droplet touches the particle, itself is a free-moving object experiencing a drag force that is well depicted in the literature. This drag force is relatively small. Once it is “pinned” by the fixed particle, it starts to feel an enhanced “drag force” due to the resistance to flow of the continuous phase ([95]). This resistance to flow exerts a pressure drop across the droplet ( $\Delta P_2$ ), which is exerted on the particle through their joint interface. Take the cross-section of the main channel as  $A$ , the projection of the particle’s cross session in the main channel as  $S$ , a force of magnitude  $\Delta P_2 S$  is pushing directly (an enhanced drag force) on the particle through the joint interface (for simplicity, here we use  $S$  as an approximation for the projection of the joint interface), and  $\Delta P_2 (A - S)$  is responsible for the droplet deformation. Due to the droplet deformation caused by the force of  $\Delta P_2 (A - S)$ , surface tension also acts on the particle through the contact area, scaled as  $\gamma L$ , where  $L$  is the circumference of the joint interface. In total, it is  $\Delta P_2 S + \gamma L$  that gives the particle an enhanced pushing force which might help it escape from the trapping zone. All the rest of the pushing force is responsible for the continuous deformation of the droplet.

Now, let’s estimate  $\Delta P_2$ . In their pioneer work [95], Garstecki et al. used the Hagen–Poiseuille equation to estimate the pressure drop over the tip of a forming droplet at the T junction, assuming the resistance to pass of the continuous phase is a result of its need to pass through a thin cube (gap) between the tip and the channel wall. In our case, the initial state is a droplet at a quasi-static condition in the channel when it is flowing. The moment it is pinned, the gutter areas become the only path for the continuous phase to pass, as the particle cross-section  $S$  is close to the channel cross-section  $A$ , and as the deformation takes time. With more time, the gutter area will increase with more droplet deformation, or even a tunnel will be opened, decreasing the pushing force. Therefore, we consider comparing the maximum pushing force, reached with a gutter area from the droplet quasi-static condition (time zero), with the pressing force. If at this moment the balance can not be turned over, i.e., the releasing process is not initiated, there will be no more chance afterward. This corresponds to the fact that we never observed the particles being released after the droplet had observable deformation—they are always released promptly from the start. From equation 2.1 we have the gutter radius

of a droplet in the rectangular shape channel as [79]:

$$r_g = \frac{h}{1 + \frac{h}{w} + \sqrt{\left(1 - \frac{h}{w}\right)^2 + \pi \frac{h}{w}}} \quad (\text{A.17})$$

where  $h$  and  $w$  are the height and width of the main channel when  $h$  is smaller than  $w$ . The total gutter area of the four gutters is thus  $(2r_g)^2 - \pi r_g^2$ . According to Hagen–Poiseuille equation,

$$\Delta P_2 = \frac{8\pi\mu LQ}{A^2} = \frac{8\pi\mu Q_1 L}{(4 - \pi)^2 r_g^4} \quad (\text{A.18})$$

, where  $Q_1$  is the oil flow rate injected from the inlet.

### A simple Torque balance

The different forces acting on the particle are shown in Fig.A.2c. As part of the particle is inside the suction channel, we assume the release of it into the main channel is through rotation around the right corner of the channel (assume non-slipping condition). The enhanced drag forces and the pressing force create torques of different directions: the former help the particle rotate into the main channel ( $T_2$ ); the latter pulls the particle back to the trapping area ( $T_1$ ).

Set the particle radius as  $r$ , and we have:

$$T_1 = \Delta P_1 S' r \sin \theta \quad (\text{A.19})$$

$$T_2 = \Delta P_2 S(r \cos \theta) + \gamma Lr \quad (\text{A.20})$$

If  $T_2 > T_1$ , the particle can be removed from the trap.

The above model assumes a perfect blocking condition. Now we verify this model with the only experiment that can achieve this condition so far (i.e., the proof-of-concept experiment). We know the following parameters: Oil flow rate  $Q_1 = 0.16\mu\text{L}/\text{min}$ , water flow rate  $Q_2 = 0.08\mu\text{L}/\text{min}$ , the applied suction pressure  $P_3 = -63\text{mbar} = -6300\text{Pa}$ . From the channel dimensions and using the hydraulic resistance formula for rectangular channels ([124]) , we obtain  $R_{out} = 3.5e14 \frac{\text{Pa}\cdot\text{S}}{\text{m}^3}$ . We thus obtained  $\Delta P_1 = (Q_1 + Q_2)R_{out} - P_3 = 7700\text{Pa}$ . The main channel width \* height is  $30\mu\text{m} * 20\mu\text{m}$ , which leads to a gutter radius of  $r_g = 6.3\mu\text{m}$ . From the video we estimate the droplet length  $L_D = 60\mu\text{m}$ ,  $\mu = 0.0023\text{Pa}\cdot\text{S}$ , then we obtain  $\Delta P_2 = 7968\text{Pa}$ . With the particle radius of  $r = 7.5\mu\text{m}$ , the suction channel gate diameter  $l = 7\mu\text{m}$ , we further obtain  $T_1 = 1\mu\text{N}\cdot\mu\text{m}$ ,  $T_2 = 9.9\mu\text{N}\cdot\mu\text{m}$ . It shows that the torque to rotate the particle from its location is almost 10 times larger than the torque to trap it. It predicts the release of the particle, as also observed in the experiment.

The model shows several interesting results. First, by comparing the magnitude of the different

### A.3. Theoretical development of the bead releasing condition

forces we obtain the pressing force as  $\Delta P_1 S' = 0.30\mu N$  and the pushing forces which include  $\Delta P_2 S = 1.41\mu N$  and  $\gamma L = 0.08\mu N$ . We can see that the surface tension is more than one order of magnitude smaller than the enhanced drag force, signifying that the main reason for removing the particle from the suction area is through the pushing from the oil. Second, to ensure particle releasing,  $\frac{T_2}{T_1} > 1$  is required. Ignoring the surface tension term (justified by the above), we obtain an expression:

$$\frac{T_2}{T_1} = \frac{aL_D \cdot \left(\frac{b}{h}\right)^4 \cdot \left(\frac{r}{l}\right)^3 \cdot \sqrt{1 - \frac{l}{2r}} \cdot \left(\frac{Q_1}{Q_2}\right)}{(1+c)(R_{out} + R_S)} \quad (\text{A.21})$$

where  $a = \frac{64\pi\mu}{(4-\pi)^2}$  is a constant, and  $b = 1 + \frac{h}{w} + \sqrt{\left(1 - \frac{h}{w}\right)^2 + \pi \frac{h}{w}}$  (from eq.A.17) is a correction factor for the aspect ratio of the rectangular channel with maximal value obtained with a square shape cross section (aspect ratio = 1). If we take into account the influence of  $h$  on  $R_{out}$  and  $R_S$  assuming a single height device with rectangular channels, we obtain

$$\frac{T_2}{T_1} \propto \frac{L_D \left(\frac{b^4}{h}\right) \cdot \left(\frac{r}{l}\right)^3 \cdot \sqrt{1 - \frac{l}{2r}} \cdot \left(\frac{Q_1}{Q_2}\right)}{(1+c)\left(\frac{L_{out}}{w_{out}} + \frac{L_S}{w_S}\right)} \quad (\text{A.22})$$

where  $L_{out}$ ,  $L_S$  and  $w_{out}$  and  $w_S$  are the length and width of the outlet main channel and the suction channel respectively. The design rule shows that the probability of a particle being released dramatically increases if the particle-to-gate size ratio ( $r/l$ ) is large. Generally, it is better to have a smaller dimension channel with a square cross-section. In such a case, a smaller gutter radius will be created to form a large pushing force for a given flow rate of the oil. It is also recommended to minimize the  $\frac{L}{w}$  ratio for both the outlet and the suction channel to minimize their resistance. During the operation, a large  $\frac{Q_1}{Q_2}$  ratio is favored. It is also beneficial to lower the  $c$  through wetting property control and by avoiding excessive suction pressure.

## A.4 Design optimization for In-flow

### A.4.1 Optimization of the fluidic elements

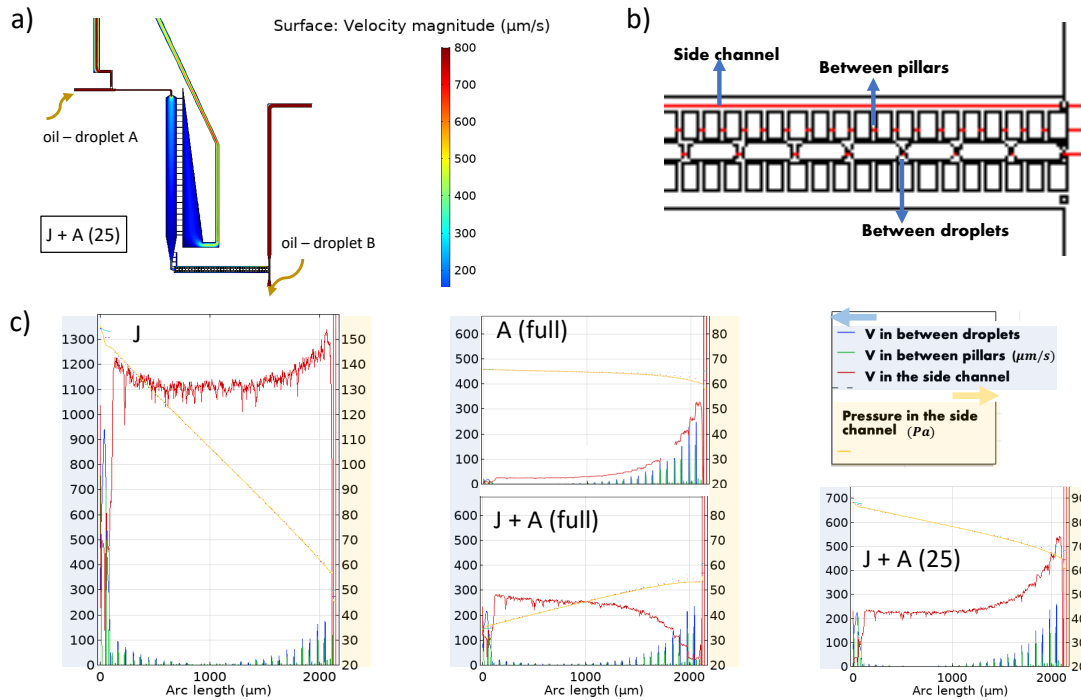


Figure A.4 – **Simulation of the oil extraction performance.** a) An example of the COMSOL simulation with the geometry of J + A (25). The color map represents the velocity magnitude. Brown arrows: inlets where the oil flow rates are specified for the model. Here, droplets in the waiting line are simulated as solid obstacles with certain spacing to account for the 3D effect. b) Definition of three data extraction lines, for results presented in c). The lines start from the entrance of the waiting line (not shown) until the end of the waiting line crossing the main channel. They extend across the side channel, between the pillars, and between the droplets. c) Results extracted from the measuring lines defined in b). The geometry is indicated on the top left of the figures, the left y-axis is for velocity magnitude (in  $\mu\text{m/s}$ ) and the right y-axis is for the pressure magnitude (in  $\text{Pa}$ ). The Arc length (x-axis) is the length of the waiting line section in real scale, where 0 represents the entrance. The yellow line shows the pressure drop across the waiting line in the side channel (right y-axis). The blue, green, and red lines show the velocity between droplets, pillars, and inside the side channel, respectively.

Optimizing fluidic elements particularly concerns the modulation of the degree of passive oil extraction via the design of J & A elements. We simulated different devices with a fully loaded WL structure for varying J & A configurations, imposed with experimental oil flow rates of both droplets A and B ( $0.4$  and  $0.3 \mu\text{L}/\text{min}$  respectively). Fig. A.4a shows one example with device “J + A (25)”. A (25) is the oil extraction array with a sparse array of 25 channels of  $4 \mu\text{m}$  width. We also have an “A (full)” element with a dense array of more than 300 tiny channels of  $3 \mu\text{m}$

width. The pressure and velocity distribution within the waiting line at different locations, i.e, between the droplets, between the pillars, and within the side channels (Fig. A.4b) are shown in Fig. A.4c. In all cases, the speed in-between pillars is slightly lower than the speed in-between droplets, and these speed profiles do not vary too much among different devices. On the other hand, the speed profile in the side channel does vary a lot with different oil extraction components, showing its important modulation function when the waiting line is full. Here, the profile in the side channel is used as an indicator of how much oil remains in the waiting line after the two times oil reduction. With J +A (full), the pressure head is negative thus backflow happens, and with A (full) the pressure head is close to zero thus the oil extraction does not leave much excessive oil flow, shown by the small gap between the red line and the blue/green lines. In J-only device, there is a huge pressure head accumulated and a high flow speed in the WL side channel. We can deduce that having both elements is more efficient in oil extraction than having a single element, and A (full) is more efficient than J.

Our experiments qualitatively support these findings. With J + A (full) device we observed too much oil extraction where the droplets are reluctant to enter the waiting line and are retained at the neck. With the J-only device, the oil extraction is not enough, evidenced by the fact that the post cannot stop some droplets A, which leave the waiting line, and droplets in waiting line tends to merge with themselves. As a rule of thumb for design, we seek for a moderate and positive pressure gradient in the WL for automatic droplet loading and refilling of the WL while keeping droplets away from breaking. With the aid of the simulation, we find that J + A (25) is the best combination for our purpose.

#### A.4.2 Optimization of electrocoalescence configuration

From Eq.6.1 and Eq.6.2, the two electric forces are dependent on the polarization degree of the droplets and the oil medium, and so will the electrocoalescence efficiency. We investigated which electrode configuration gives the most favorable polarization via simulation ( Fig. A.5). Three electrodes are configured around the merging point by filling the corresponding PDMS channels. The goal is to maximize the main merging event efficiency (i.e., first droplet A merged with the incoming droplet B) while minimizing the secondary merging event efficiency (i.e., the second droplet A merged with the first droplet A). We thus define a ratio of polarization magnitude between the primary merging point (green arrow) and the secondary merging point (yellow arrow), shown as the red numbers in FigA.5. a-c) shows the importance of the external E field orientation (E lines shown with black solid lines) on the specificity of the electrocoalescence effect. In addition, if two out of the three electrodes have the same potential, the E field will be drawn over a large area over the waiting line and induce more prominent polarization over the secondary merging point thus lowering the specificity. We have chose FigA.5d (4.) as our configuration.

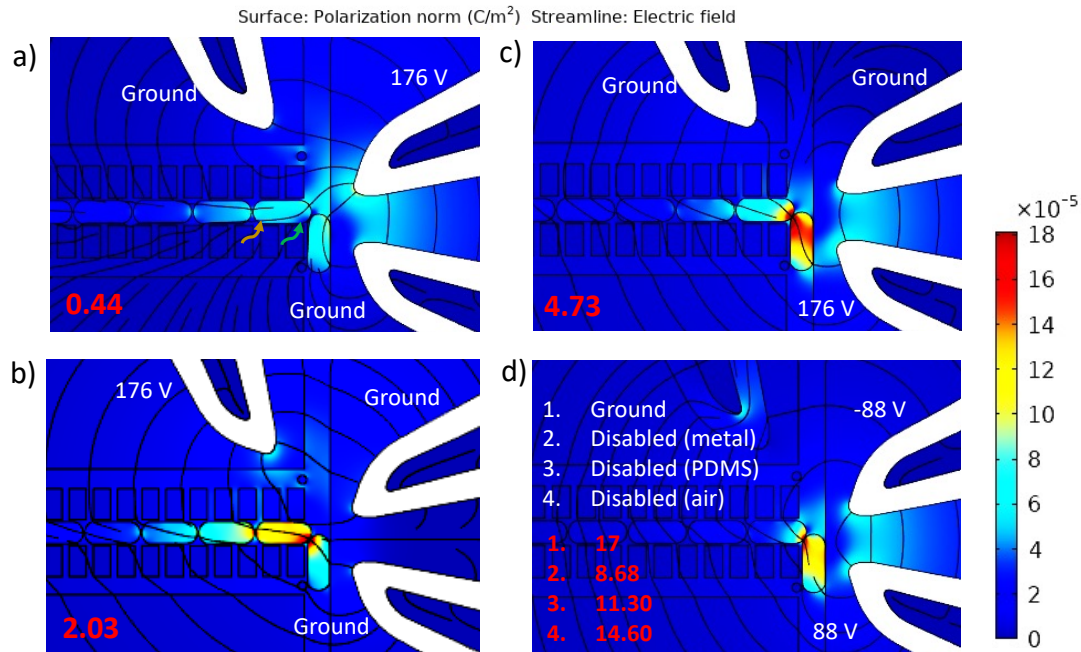


Figure A.5 – **Surface plot of polarization norm ( $C/m^2$ )**. We input channel and electrode geometry and the parameters of the materials to simulate the electric field as well as polarization magnitude under different electrode deployments. The simulation is conducted under a DC field, where droplets are represented as liquid ellipses, separated by a thin film (smallest dimension of  $3 \mu m$ ) of oil medium. The input voltage is shown by the side of the corresponding electrodes, the external electric field line is shown as black lines, the polarization norm ratio of the primary spot (pointed by green arrow) over the secondary spot (pointed by yellow arrow) is shown as the red number for each configuration. a) Electric field is drawn from the positive electrode towards the two ground electrodes, the created E field vector cause stronger polarization at the secondary spot than the primary one; b) Electric field is drawn from the positive electrode to the two ground electrodes, a different E lines orientation results in stronger polarization at the primary spot, but also at the secondary spot; c) Electric field is drawn from the positive electrode to the two ground electrodes, the selectivity is improved; d) Compared to the previous configurations, the left side electrode is not connected, but is still filled with different materials (metal). The shown surface plot is for the metal condition. The best configuration is to use air (with the lowest dielectric constant) for the “shielding” electrode.

**The merging point design** From above we have seen the importance of the relative orientation between the droplet contact interface and the applied E field. Experimentally we also observed that electrocoalescence almost only happen at the droplet head-to-head or head-to-tail contact moment (Fig.A.6a). This is because in a head-to-body configuration the droplet interface to be merged is parallel to the E lines, which does not induce electrocoalescence. Luckily, this is the case for all other droplets A interfaces inside the waiting line. On the other hand, if we allow droplet A and B contact with the right angle with a sufficient contact area, we might

#### A.4. Design optimization for In-flow

improve the electrocoalescence efficiency as well as selectivity. To this end, we designed three post structures (P1, P2, and P3, Fig.A.6B, in red rectangular) with the aim to reach a good compromise between a good stopping effect and a large droplet A -droplet B contact angle and area.

Experiments reveal that P3 is a bad design idea which causes severe pinning of droplet B at the junction, and re-breaking of the merged droplet during the releasing step (droplet is split by the P3 pillar once again). P2 design holds the droplets A very well but the two extended pillars create a barrier between the frontier droplet A and the flowing droplet B, which can only be overcome by pushing strongly in the WL with a higher oil flowrate. P1 on the other hand has allowed a large droplet surface in the main channel while the droplets rarely escape. We have kept P1 for the following experiments.

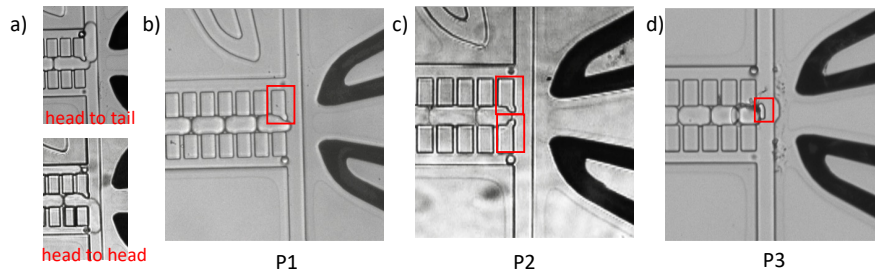


Figure A.6 – **Optimization of the merging point design**(a) bright field image showing the merging event between the head of a droplet A and the tail of a droplet B (upper) and between the head of a droplet A and the head of a droplet B (lower) ; (b-d) the three merging point design with its corresponding droplet waiting lines.



# Bibliography

- [1] Marius Lange, Volker Bergen, Michal Klein, Manu Setty, Bernhard Reuter, Mostafa Bakhti, Heiko Lickert, Meshal Ansari, Janine Schniering, Herbert B Schiller, et al. Cellrank for directed single-cell fate mapping. *Nature methods*, 19(2):159–170, 2022.
- [2] Kinga Matuła, Francesca Rivello, and Wilhelm TS Huck. Single-cell analysis using droplet microfluidics. *Advanced Biosystems*, 4(1):1900188, 2020.
- [3] Tim Stuart and Rahul Satija. Integrative single-cell analysis. *Nature reviews genetics*, 20(5):257–272, 2019.
- [4] Xiannian Zhang, Tianqi Li, Feng Liu, Yaqi Chen, Jiacheng Yao, Zeyao Li, Yanyi Huang, and Jianbin Wang. Comparative analysis of droplet-based ultra-high-throughput single-cell rna-seq systems. *Molecular cell*, 73(1):130–142, 2019.
- [5] Fredrik Salmen, Joachim De Jonghe, Tomasz S Kaminski, Anna Alemany, Guillermo E Parada, Joe Verity-Legg, Ayaka Yanagida, Timo N Kohler, Nicholas Battich, Floris van den Brekel, et al. High-throughput total rna sequencing in single cells using vasa-seq. *Nature Biotechnology*, pages 1–14, 2022.
- [6] Julia Källberg, Wenjin Xiao, David Van Assche, Jean-Christophe Baret, and Valérie Taly. Frontiers in single cell analysis: multimodal technologies and their clinical perspectives. *Lab on a Chip*, 22(13):2403–2422, 2022.
- [7] Wanze Chen, Orane Guillaume-Gentil, Pernille Yde Rainer, Christoph G Gäbelein, Wouter Saelens, Vincent Gardeux, Amanda Klaeger, Riccardo Dainese, Magda Zachara, Tomaso Zambelli, et al. Live-seq enables temporal transcriptomic recording of single cells. *Nature*, 608(7924):733–740, 2022.
- [8] Eleni P Mimitou, Anthony Cheng, Antonino Montalbano, Stephanie Hao, Marlon Stoekius, Mateusz Legut, Timothy Roush, Alberto Herrera, Efthymia Papalexi, Zhengqing Ouyang, et al. Multiplexed detection of proteins, transcriptomes, clonotypes and crispr perturbations in single cells. *Nature methods*, 16(5):409–412, 2019.
- [9] Florent Ginhoux, Adam Yalin, Charles Antoine Dutertre, and Ido Amit. Single-cell immunology: Past, present, and future. *Immunity*, 55(3):393–404, 2022.

## Bibliography

---

- [10] Sanjay M Prakadan, Alex K Shalek, and David A Weitz. Scaling by shrinking: empowering single-cell 'omics' with microfluidic devices. *Nature Reviews Genetics*, 18(6):345–361, 2017.
- [11] Xuhao Luo, Jui-Yi Chen, Marzieh Ataei, and Abraham Lee. Microfluidic compartmentalization platforms for single cell analysis. *Biosensors*, 12(2):58, 2022.
- [12] Marc A Unger, Hou-Pu Chou, Todd Thorsen, Axel Scherer, and Stephen R Quake. Monolithic microfabricated valves and pumps by multilayer soft lithography. *science*, 288(5463):113–116, 2000.
- [13] Jianbin Wang, H Christina Fan, Barry Behr, and Stephen R Quake. Genome-wide single-cell analysis of recombination activity and de novo mutation rates in human sperm. *Cell*, 150(2):402–412, 2012.
- [14] Naveen Ramalingam, Brian Fowler, Lukasz Szpankowski, Anne A Leyrat, Kyle Hukari, Myo Thu Maung, Wiganda Yorza, Michael Norris, Chris Cesar, Joe Shuga, et al. Fluidic logic used in a systems approach to enable integrated single-cell functional analysis. *Frontiers in bioengineering and biotechnology*, 4:70, 2016.
- [15] Alex K Shalek, Rahul Satija, Joe Shuga, John J Trombetta, Dave Gennert, Diana Lu, Peilin Chen, Rona S Gertner, Jellert T Gaublomme, Nir Yosef, et al. Single-cell rna-seq reveals dynamic paracrine control of cellular variation. *Nature*, 510(7505):363–369, 2014.
- [16] Ren Li, Fei Jia, Weikai Zhang, Fanghao Shi, Zhiguo Fang, Hong Zhao, Zhiyuan Hu, and Zewen Wei. Device for whole genome sequencing single circulating tumor cells from whole blood. *Lab on a Chip*, 19(19):3168–3178, 2019.
- [17] Adam K White, Michael VanInsberghe, Oleh I Petriv, Mani Hamidi, Darek Sikorski, Marco A Marra, James Piret, Samuel Aparicio, and Carl L Hansen. High-throughput microfluidic single-cell rt-qpcr. *Proceedings of the National Academy of Sciences*, 108(34):13999–14004, 2011.
- [18] Hao Sun, Tim Olsen, Jing Zhu, Jianguo Tao, Brian Ponnaiya, Sally A Amundson, David J Brenner, and Qiao Lin. A bead-based microfluidic approach to integrated single-cell gene expression analysis by quantitative rt-pcr. *RSC advances*, 5(7):4886–4893, 2015.
- [19] Qihui Shi, Lidong Qin, Wei Wei, Feng Geng, Rong Fan, Young Shik Shin, Deliang Guo, Leroy Hood, Paul S Mischel, and James R Heath. Single-cell proteomic chip for profiling intracellular signaling pathways in single tumor cells. *Proceedings of the National Academy of Sciences*, 109(2):419–424, 2012.
- [20] Johannes Bues, Marjan Biočanin, Joern Pezoldt, Riccardo Dainese, Antonius Chrisnandy, Saba Rezakhani, Wouter Saelens, Vincent Gardeux, Revant Gupta, Rita Sarkis, et al. Deterministic scrna-seq captures variation in intestinal crypt and organoid composition. *Nature Methods*, 19(3):323–330, 2022.

- [21] Jinzhou Yuan and Peter A Sims. An automated microwell platform for large-scale single cell rna-seq. *Scientific reports*, 6(1):1–10, 2016.
- [22] Sayantan Bose, Zhenmao Wan, Ambrose Carr, Abbas H Rizvi, Gregory Vieira, Dana Pe’er, and Peter A Sims. Scalable microfluidics for single-cell rna printing and sequencing. *Genome biology*, 16(1):1–16, 2015.
- [23] Yin Tang, Zhuo Wang, Ziming Li, Jungwoo Kim, Yuliang Deng, Yan Li, James R Heath, Wei Wei, Shun Lu, and Qihui Shi. High-throughput screening of rare metabolically active tumor cells in pleural effusion and peripheral blood of lung cancer patients. *Proceedings of the National Academy of Sciences*, 114(10):2544–2549, 2017.
- [24] Yunpeng Bai, Ximin He, Dingsheng Liu, Santoshkumar N Patil, Dan Bratton, Ansgar Huebner, Florian Hollfelder, Chris Abell, and Wilhelm TS Huck. A double droplet trap system for studying mass transport across a droplet-droplet interface. *Lab on a Chip*, 10(10):1281–1285, 2010.
- [25] Jean G Riess and Marie Pierre Krafft. Fluorinated materials for in vivo oxygen transport (blood substitutes), diagnosis and drug delivery. *Biomaterials*, 19(16):1529–1539, 1998.
- [26] Luoran Shang, Yao Cheng, and Yuanjin Zhao. Emerging droplet microfluidics. *Chemical reviews*, 117(12):7964–8040, 2017.
- [27] Burak Dura, Stephanie K Dougan, Marta Barisa, Melanie M Hoehl, Catherine T Lo, Hidde L Ploegh, and Joel Voldman. Profiling lymphocyte interactions at the single-cell level by microfluidic cell pairing. *Nature communications*, 6(1):1–13, 2015.
- [28] Faruk Azam Shaik, Clara Lewuillon, Aurélie Guillemette, Bahram Ahmadian, Carine Brinster, Bruno Quesnel, Dominique Collard, Yasmine Touil, Loïc Lemonnier, and Mehmet Cagatay Tarhan. Pairing cells of different sizes in a microfluidic device for immunological synapse monitoring. *Lab on a Chip*, 22(5):908–920, 2022.
- [29] Alison M Skelley, Oktay Kirak, Heikyung Suh, Rudolf Jaenisch, and Joel Voldman. Microfluidic control of cell pairing and fusion. *Nature methods*, 6(2):147–152, 2009.
- [30] Sanchari Bhattacharya, Tzu-Chiao Chao, Nethmi Ariyasinghe, Yvette Ruiz, Douglas Lake, Robert Ros, and Alexandra Ros. Selective trapping of single mammalian breast cancer cells by insulator-based dielectrophoresis. *Analytical and bioanalytical chemistry*, 406(7):1855–1865, 2014.
- [31] David J Collins, Belinda Morahan, Jose Garcia-Bustos, Christian Doerig, Magdalena Plebanski, and Adrian Neild. Two-dimensional single-cell patterning with one cell per well driven by surface acoustic waves. *Nature communications*, 6(1):1–11, 2015.
- [32] Meng Ting Chung, Daniel Núñez, Dawen Cai, and Katsuo Kurabayashi. Deterministic droplet-based co-encapsulation and pairing of microparticles via active sorting and downstream merging. *Lab on a Chip*, 17(21):3664–3671, 2017.

## Bibliography

---

- [33] M Sauzade and E Brouzes. Deterministic trapping, encapsulation and retrieval of single-cells. *Lab on a Chip*, 17(13):2186–2192, 2017.
- [34] Jeonghun Nam, Hyunjung Lim, Choong Kim, Ji Yoon Kang, and Sehyun Shin. Density-dependent separation of encapsulated cells in a microfluidic channel by using a standing surface acoustic wave. *Biomicrofluidics*, 6(2):024120, 2012.
- [35] Alexandra C Sun, Daniel J Steyer, Anthony R Allen, Emory M Payne, Robert T Kennedy, and Corey RJ Stephenson. A droplet microfluidic platform for high-throughput photochemical reaction discovery. *Nature communications*, 11(1):1–6, 2020.
- [36] Zoe Swank, Grégoire Michielin, Hon Ming Yip, Patrick Cohen, Diego O Andrey, Nicolas Vuilleumier, Laurent Kaiser, Isabella Eckerle, Benjamin Meyer, and Sebastian J Maerkl. A high-throughput microfluidic nanoimmunoassay for detecting anti-sars-cov-2 antibodies in serum or ultralow-volume blood samples. *Proceedings of the National Academy of Sciences*, 118(18), 2021.
- [37] Naside Gozde Durmus, Savas Tasoglu, and Utkan Demirci. Functional droplet networks. *Nature materials*, 12(6):478–479, 2013.
- [38] Yu Zhang, Zhichao Dong, Chuxin Li, Huifeng Du, Nicholas X Fang, Lei Wu, and Yanlin Song. Continuous 3d printing from one single droplet. *Nature communications*, 11(1):1–10, 2020.
- [39] Ravinash Krishna Kumar, Thomas A Meiller-Legrand, Alessandro Alcinesio, Diego Gonzalez, Despoina AI Mavridou, Oliver J Meacock, William PJ Smith, Linna Zhou, Wook Kim, Gökçe Su Pulcu, et al. Droplet printing reveals the importance of micron-scale structure for bacterial ecology. *Nature communications*, 12(1):1–12, 2021.
- [40] Christopher M Hindson, John R Chevillet, Hilary A Briggs, Emily N Gallichotte, Ingrid K Ruf, Benjamin J Hindson, Robert L Vessella, and Muneesh Tewari. Absolute quantification by droplet digital pcr versus analog real-time pcr. *Nature methods*, 10(10):1003–1005, 2013.
- [41] Yi Zhang, Yoshihiro Minagawa, Hiroto Kizoe, Kentaro Miyazaki, Ryota Iino, Hiroshi Ueno, Kazuhito V Tabata, Yasuhiro Shimane, and Hiroyuki Noji. Accurate high-throughput screening based on digital protein synthesis in a massively parallel femtoliter droplet array. *Science advances*, 5(8):eaav8185, 2019.
- [42] Damian Zaremba, Sławomir Błoński, and Piotr M Korczyk. Integration of capillary-hydrodynamic logic circuitries for built-in control over multiple droplets in microfluidic networks. *Lab on a Chip*, 21(9):1771–1778, 2021.
- [43] Heng-Dong Xi, Hao Zheng, Wei Guo, Alfonso M Gañán-Calvo, Ye Ai, Chia-Wen Tsao, Jun Zhou, Weihua Li, Yanyi Huang, Nam-Trung Nguyen, et al. Active droplet sorting in microfluidics: a review. *Lab on a Chip*, 17(5):751–771, 2017.

- 
- [44] Shih-Kang Fan, Po-Wen Huang, Tsu-Te Wang, and Yu-Hao Peng. Cross-scale electric manipulations of cells and droplets by frequency-modulated dielectrophoresis and electrowetting. *Lab on a Chip*, 8(8):1325–1331, 2008.
- [45] Peixian Li, Zhichao Ma, Yinning Zhou, David J Collins, Zhenfeng Wang, and Ye Ai. Detachable acoustophoretic system for fluorescence-activated sorting at the single-droplet level. *Analytical chemistry*, 91(15):9970–9977, 2019.
- [46] Yueyue Zhang, Tingting Zheng, Li Wang, Liang Feng, Min Wang, Zhenchao Zhang, and Huanhuan Feng. From passive to active sorting in microfluidics: A review. *Reviews on Advanced Materials Science*, 60(1):313–324, 2021.
- [47] Tengyang Jing, Ramesh Ramji, Majid Ebrahimi Warkiani, Jongyoon Han, Chwee Teck Lim, and Chia-Hung Chen. Jetting microfluidics with size-sorting capability for single-cell protease detection. *Biosensors and Bioelectronics*, 66:19–23, 2015.
- [48] Max Chabert and Jean-Louis Viovy. Microfluidic high-throughput encapsulation and hydrodynamic self-sorting of single cells. *Proceedings of the National Academy of Sciences*, 105(9):3191–3196, 2008.
- [49] Eujin Um, Seung-Goo Lee, and Je-Kyun Park. Random breakup of microdroplets for single-cell encapsulation. *Applied Physics Letters*, 97(15):153703, 2010.
- [50] Shamik Hazra, Sushanta K Mitra, and Ashis Kumar Sen. Lateral migration of viscoelastic droplets in a viscoelastic confined flow: role of discrete phase viscoelasticity. *Soft matter*, 15(44):9003–9010, 2019.
- [51] Andrew C Hatch, Apurva Patel, N Reginald Beer, and Abraham P Lee. Passive droplet sorting using viscoelastic flow focusing. *Lab on a Chip*, 13(7):1308–1315, 2013.
- [52] Edgar Häner, Matthias Heil, and Anne Juel. Deformation and sorting of capsules in a t-junction. *Journal of Fluid Mechanics*, 885, 2020.
- [53] Ching W Pan, Daniel G Horvath, Samuel Braza, Trevor Moore, Annabella Lynch, Cameron Feit, and Paul Abbyad. Sorting by interfacial tension (sift): label-free selection of live cells based on single-cell metabolism. *Lab on a Chip*, 19(8):1344–1351, 2019.
- [54] Grace CE Porter, Sebastien NF Sikora, Jung-uk Shim, Benjamin J Murray, and Mark D Tarn. On-chip density-based sorting of supercooled droplets and frozen droplets in continuous flow. *Lab on a Chip*, 20(21):3876–3887, 2020.
- [55] David J Collins, Adrian Neild, Andrew DeMello, Ai-Qun Liu, and Ye Ai. The poisson distribution and beyond: methods for microfluidic droplet production and single cell encapsulation. *Lab on a Chip*, 15(17):3439–3459, 2015.

## Bibliography

---

- [56] Jon F Edd, Dino Di Carlo, Katherine J Humphry, Sarah Köster, Daniel Irimia, David A Weitz, and Mehmet Toner. Controlled encapsulation of single-cells into monodisperse picolitre drops. *Lab on a Chip*, 8(8):1262–1264, 2008.
- [57] Evelien WM Kemna, Rogier M Schoeman, Floor Wolbers, Istvan Vermes, David A Weitz, and Albert Van Den Berg. High-yield cell ordering and deterministic cell-in-droplet encapsulation using dean flow in a curved microchannel. *Lab on a Chip*, 12(16):2881–2887, 2012.
- [58] Adam R Abate, Chia-Hung Chen, Jeremy J Agresti, and David A Weitz. Beating poisson encapsulation statistics using close-packed ordering. *Lab on a Chip*, 9(18):2628–2631, 2009.
- [59] Kenza Samlali, Fatemeh Ahmadi, Angela BV Quach, Guy Soffer, and Steve CC Shih. One cell, one drop, one click: hybrid microfluidics for mammalian single cell isolation. *Small*, 16(34):2002400, 2020.
- [60] Mingxia Zhang, Yuan Zou, Xing Xu, Xuebing Zhang, Mingxuan Gao, Jia Song, Peifeng Huang, Qin Chen, Zhi Zhu, Wei Lin, et al. Highly parallel and efficient single cell mrna sequencing with paired picoliter chambers. *Nature communications*, 11(1):1–13, 2020.
- [61] Pingan Zhu and Liqiu Wang. Passive and active droplet generation with microfluidics: a review. *Lab on a Chip*, 17(1):34–75, 2017.
- [62] Mathieu Joanicot and Armand Ajdari. Droplet control for microfluidics. *Science*, 309(5736):887–888, 2005.
- [63] Todd Thorsen, Richard W Roberts, Frances H Arnold, and Stephen R Quake. Dynamic pattern formation in a vesicle-generating microfluidic device. *Physical review letters*, 86(18):4163, 2001.
- [64] Shelley L Anna, Nathalie Bontoux, and Howard A Stone. Formation of dispersions using “flow focusing” in microchannels. *Applied physics letters*, 82(3):364–366, 2003.
- [65] Carsten Cramer, Peter Fischer, and Erich J Windhab. Drop formation in a co-flowing ambient fluid. *Chemical Engineering Science*, 59(15):3045–3058, 2004.
- [66] Jian Hong Xu, SW Li, Jing Tan, and GS Luo. Correlations of droplet formation in t-junction microfluidic devices: from squeezing to dripping. *Microfluidics and Nanofluidics*, 5(6):711–717, 2008.
- [67] Charles N Baroud, Francois Gallaire, and Rémi Danga. Dynamics of microfluidic droplets. *Lab on a Chip*, 10(16):2032–2045, 2010.
- [68] Piotr M Korczyk, Volkert Van Steijn, Slawomir Blonski, Damian Zaremba, David A Beattie, and Piotr Garstecki. Accounting for corner flow unifies the understanding of droplet formation in microfluidic channels. *Nature communications*, 10(1):1–9, 2019.

- [69] Rémi Dangla, Etienne Fradet, Yonatan Lopez, and Charles N Baroud. The physical mechanisms of step emulsification. *Journal of Physics D: Applied Physics*, 46(11):114003, 2013.
- [70] M De Menech, Piotr Garstecki, F Jousse, and Howard A Stone. Transition from squeezing to dripping in a microfluidic t-shaped junction. *journal of fluid mechanics*, 595:141–161, 2008.
- [71] Ming Wang, Mui Hoon Nai, Ruby Yun-Ju Huang, Hwa Liang Leo, Chwee Teck Lim, and Chia-Hung Chen. High-throughput functional profiling of single adherent cells via hydrogel drop-screen. *Lab on a Chip*, 21(4):764–774, 2021.
- [72] Rémi Dangla, S Cagri Kayi, and Charles N Baroud. Droplet microfluidics driven by gradients of confinement. *Proceedings of the National Academy of Sciences*, 110(3):853–858, 2013.
- [73] Z Li, AM Leshansky, LM Pismen, and P Tabeling. Step-emulsification in a microfluidic device. *Lab on a Chip*, 15(4):1023–1031, 2015.
- [74] Maximilian L Eggersdorfer, Hansjörg Seybold, Alessandro Ofner, David A Weitz, and André R Studart. Wetting controls of droplet formation in step emulsification. *Proceedings of the National Academy of Sciences*, 115(38):9479–9484, 2018.
- [75] DR Link, Shelley L Anna, DA Weitz, and HA Stone. Geometrically mediated breakup of drops in microfluidic devices. *Physical review letters*, 92(5):054503, 2004.
- [76] Alexander M Leshansky and Len M Pismen. Breakup of drops in a microfluidic t junction. *Physics of Fluids*, 21(2):023303, 2009.
- [77] Cees Haringa, Conrad De Jong, Duong A Hoang, Luis M Portela, Chris R Kleijn, Michiel T Kreutzer, and Volkert Van Steijn. Breakup of elongated droplets in microfluidic t-junctions. *Physical Review Fluids*, 4(2):024203, 2019.
- [78] Volkert van Steijn, Piotr M Korczyk, Ladislav Derzsi, Adam R Abate, David A Weitz, and Piotr Garstecki. Block-and-break generation of microdroplets with fixed volume. *Biomechanics*, 7(2):024108, 2013.
- [79] Harris Wong, S Morris, and CJ Radke. Three-dimensional menisci in polygonal capillaries. *Journal of Colloid and Interface Science*, 148(2):317–336, 1992.
- [80] T. C. Ransohoff and C. J. Radke. Laminar flow of a wetting liquid along the corners of a predominantly gas-occupied noncircular pore. *J. Colloid Interf. Sci.*, 121, 1988.
- [81] A. de Lózar, A. L. Hazel, and A. Juel. Scaling properties of coating flows in rectangular channels. *Phys. Rev. Lett.*, 99:234501, Dec 2007.

## Bibliography

---

- [82] Rapolas Zilionis, Juozas Nainys, Adrian Veres, Virginia Savova, David Zemmour, Alon M Klein, and Linas Mazutis. Single-cell barcoding and sequencing using droplet microfluidics. *Nature protocols*, 12(1):44–73, 2017.
- [83] Masumi Yamada, Megumi Nakashima, and Minoru Seki. Pinched flow fractionation: continuous size separation of particles utilizing a laminar flow profile in a pinched microchannel. *Analytical chemistry*, 76(18):5465–5471, 2004.
- [84] Xiaoyun Ding, Martin P Stewart, Armon Sharei, James C Weaver, Robert S Langer, and Klavs F Jensen. High-throughput nuclear delivery and rapid expression of dna via mechanical and electrical cell-membrane disruption. *Nature biomedical engineering*, 1(3):1–7, 2017.
- [85] Alina Kollmannsperger, Armon Sharei, Anika Raulf, Mike Heilemann, Robert Langer, Klavs F Jensen, Ralph Wieneke, and Robert Tampé. Live-cell protein labelling with nanometre precision by cell squeezing. *Nature communications*, 7(1):1–7, 2016.
- [86] Itai Cohen, Hui Li, James L Hougland, Milan Mrksich, and Sidney R Nagel. Using selective withdrawal to coat microparticles. *Science*, 292(5515):265–267, 2001.
- [87] Iain C Clark and Adam R Abate. Microfluidic bead encapsulation above 20 khz with triggered drop formation. *Lab on a Chip*, 18(23):3598–3605, 2018.
- [88] Ju Wang, Zhaomiao Liu, Yan Pang, Mengqi Li, and Qiang Zhou. Breakup of compound jets with inner droplets in a capillary flow-focusing device. *Physics of Fluids*, 33(1):013304, 2021.
- [89] Ju Wang, Zhaomiao Liu, Yan Pang, and Mengqi Li. Perturbations of liquid jets with an entering sphere in flow focusing. *International Journal of Multiphase Flow*, 147:103914, 2022.
- [90] KS Jayaprakash and AK Sen. Droplet encapsulation of particles in different regimes and sorting of particle-encapsulating-droplets from empty droplets. *Biomicrofluidics*, 13(3):034108, 2019.
- [91] Young Joon Sung, Jaon Young Hwan Kim, Hong Il Choi, Ho Seok Kwak, and Sang Jun Sim. Magnetophoretic sorting of microdroplets with different microalgal cell densities for rapid isolation of fast growing strains. *Scientific reports*, 7(1):1–11, 2017.
- [92] Yixing Gou, Yixuan Jia, Peng Wang, and Changku Sun. Progress of inertial microfluidics in principle and application. *Sensors*, 18(6):1762, 2018.
- [93] Amit Gupta and Ranganathan Kumar. Flow regime transition at high capillary numbers in a microfluidic t-junction: Viscosity contrast and geometry effect. *Physics of Fluids*, 22(12):122001, 2010.

- [94] Taotao Fu, Yining Wu, Youguang Ma, and Huai Z Li. Droplet formation and breakup dynamics in microfluidic flow-focusing devices: From dripping to jetting. *Chemical engineering science*, 84:207–217, 2012.
- [95] Piotr Garstecki, Michael J Fuerstman, Howard A Stone, and George M Whitesides. Formation of droplets and bubbles in a microfluidic t-junction—scaling and mechanism of break-up. *Lab on a Chip*, 6(3):437–446, 2006.
- [96] Margaux Duchamp, Marion Arnaud, Sara Bobisse, George Coukos, Alexandre Harari, and Philippe Renaud. Microfluidic device for droplet pairing by combining droplet raiting and floating trap arrays. *Micromachines*, 12(9):1076, 2021.
- [97] Clémentine Lipp, Kevin Uning, Jonathan Cottet, Daniel Migliozi, Arnaud Bertsch, and Philippe Renaud. Planar hydrodynamic traps and buried channels for bead and cell trapping and releasing. *Lab on a Chip*, 21(19):3686–3694, 2021.
- [98] Shiyu Wang, Yang Liu, Yijian Li, Menghua Lv, Kai Gao, Ying He, Wenbo Wei, Yonggang Zhu, Xuan Dong, Xun Xu, et al. High-throughput functional screening of antigen-specific t cells based on droplet microfluidics at a single-cell level. *Analytical Chemistry*, 94(2):918–926, 2021.
- [99] Yuan Wang, Ruina Jin, Bingqing Shen, Na Li, He Zhou, Wei Wang, Yingjie Zhao, Mengshi Huang, Pan Fang, Shanshan Wang, et al. High-throughput functional screening for next-generation cancer immunotherapy using droplet-based microfluidics. *Science Advances*, 7(24):eabe3839, 2021.
- [100] Saheli Sarkar, Pooja Sabhachandani, Dashnamoorthy Ravi, Sayalee Potdar, Sneha Purvey, Afshin Beheshti, Andrew M Evens, and Tania Konry. Dynamic analysis of human natural killer cell response at single-cell resolution in b-cell non-hodgkin lymphoma. *Frontiers in immunology*, page 1736, 2017.
- [101] Saheli Sarkar, Wenjing Kang, Songyao Jiang, Kunpeng Li, Somak Ray, Ed Luther, Alexander R Ivanov, Yun Fu, and Tania Konry. Machine learning-aided quantification of antibody-based cancer immunotherapy by natural killer cells in microfluidic droplets. *Lab on a Chip*, 20(13):2317–2327, 2020.
- [102] JR Haliburton, SC Kim, IC Clark, RA Sperling, DA Weitz, and AR Abate. Efficient extraction of oil from droplet microfluidic emulsions. *Biomicrofluidics*, 11(3):034111, 2017.
- [103] Xize Niu, Shelly Gulati, Joshua B Edelman, and Andrew J demello. Pillar-induced droplet merging in microfluidic circuits. *Lab on a Chip*, 8(11):1837–1841, 2008.
- [104] Sameer Mhatre, Shivraj Deshmukh, and Rochish M Thaokar. Electrocoalescence of a droplet pair. *Physics of Fluids*, 27(9):092106, 2015.

## Bibliography

---

- [105] P Atten. Electrocoalescence of water droplets in an insulating liquid. *Journal of Electrostatics*, 30:259–269, 1993.
- [106] Sameer Mhatre and Rochish Thaokar. Electrocoalescence in non-uniform electric fields: An experimental study. *Chemical Engineering and Processing: Process Intensification*, 96:28–38, 2015.
- [107] Shirui Luo, Jarrod Schiffbauer, and Tengfei Luo. Effect of electric field non-uniformity on droplets coalescence. *Physical Chemistry Chemical Physics*, 18(43):29786–29796, 2016.
- [108] Thomas B Jones. Basic theory of dielectrophoresis and electrorotation. *IEEE Engineering in medicine and Biology Magazine*, 22(6):33–42, 2003.
- [109] Adrian JT Teo, Say Hwa Tan, and Nam-Trung Nguyen. On-demand droplet merging with an ac electric field for multiple-volume droplet generation. *Analytical chemistry*, 92(1):1147–1153, 2019.
- [110] Vikky Anand, Vinay A Juvekar, and Rochish M Thaokar. An experimental study on the effect of conductivity, frequency and droplets separation on the coalescence of two aqueous drops under an electric field. *Chemical Engineering Research and Design*, 152:216–225, 2019.
- [111] Craig Priest, Stephan Herminghaus, and Ralf Seemann. Controlled electrocoalescence in microfluidics: Targeting a single lamella. *Applied Physics Letters*, 89(13):134101, 2006.
- [112] Meng Ting Chung, Katsuo Kurabayashi, and Dawen Cai. Single-cell rt-lamp mrna detection by integrated droplet sorting and merging. *Lab on a Chip*, 19(14):2425–2434, 2019.
- [113] Yi Qiao, Jiye Fu, Fang Yang, Mengqin Duan, Mengting Huang, Jing Tu, and Zuhong Lu. An efficient strategy for a controllable droplet merging system for digital analysis. *RSC advances*, 8(60):34343–34349, 2018.
- [114] Eric Brouzes, Martina Medkova, Neal Savenelli, Dave Marran, Mariusz Twardowski, J Brian Hutchison, Jonathan M Rothberg, Darren R Link, Norbert Perrimon, and Michael L Samuels. Droplet microfluidic technology for single-cell high-throughput screening. *Proceedings of the National Academy of Sciences*, 106(34):14195–14200, 2009.
- [115] Jose A Wippold, Han Wang, Joseph Tingling, Julian L Leibowitz, Paul de Figueiredo, and Arum Han. Prescient: platform for the rapid evaluation of antibody success using integrated microfluidics enabled technology. *Lab on a Chip*, 20(9):1628–1638, 2020.
- [116] Todd A Duncombe, Aaron Ponti, Florian P Seebeck, and Petra S Dittrich. Uv–vis spectra-activated droplet sorting for label-free chemical identification and collection of droplets. *Analytical Chemistry*, 93(38):13008–13013, 2021.

- [117] Xixian Wang, Yi Xin, Lihui Ren, Zheng Sun, Pengfei Zhu, Yuetong Ji, Chunyu Li, Jian Xu, and Bo Ma. Positive dielectrophoresis-based raman-activated droplet sorting for culture-free and label-free screening of enzyme function in vivo. *Science advances*, 6(32):eabb3521, 2020.
- [118] Sadat Hasan, Maximilian E Blaha, Sebastian K Piendl, Anish Das, David Geissler, and Detlev Belder. Two-photon fluorescence lifetime for label-free microfluidic droplet sorting. *Analytical and bioanalytical chemistry*, 414(1):721–730, 2022.
- [119] Xixian Wang, Lihui Ren, Yetian Su, Yuetong Ji, Yaoping Liu, Chunyu Li, Xunrong Li, Yi Zhang, Wei Wang, Qiang Hu, et al. Raman-activated droplet sorting (rads) for label-free high-throughput screening of microalgal single-cells. *Analytical chemistry*, 89(22):12569–12577, 2017.
- [120] Muhsincan Sesen and Graeme Whyte. Image-based single cell sorting automation in droplet microfluidics. *Scientific reports*, 10(1):1–14, 2020.
- [121] Jack Harrington, Luis Blay Esteban, Jonathan Butement, Andres F Vallejo, Simon IR Lane, Bhavwanti Sheth, Maaikje SA Jongen, Rachel Parker, Patrick S Stumpf, Rosanna CG Smith, et al. Dual dean entrainment with volume ratio modulation for efficient droplet co-encapsulation: extreme single-cell indexing. *Lab on a Chip*, 21(17):3378–3386, 2021.
- [122] Hui-Sung Moon, Kwanghwi Je, Jae-Woong Min, Donghyun Park, Kyung-Yeon Han, Seung-Ho Shin, Woong-Yang Park, Chang Eun Yoo, and Shin-Hyun Kim. Inertial-ordering-assisted droplet microfluidics for high-throughput single-cell rna-sequencing. *Lab on a Chip*, 18(5):775–784, 2018.
- [123] M. Musterd, V. van Steijn, C. Kleijn, and M. Kreutzer. Calculating the volume of elongated bubbles and droplets in microchannels from a top view image. *RSC Adv.*, 5:16042–16049, 2015.
- [124] Henrik Bruus. *Theoretical microfluidics*, volume 18. Oxford university press, 2007.

# Jiande ZHOU

Expertise: Bioengineering, (Droplet) Microfluidics, Single-cell, BioMEMS

Email: jiande.zhou@epfl.ch

Mobile: +41 78 696 11 92

Location: 1006 Lausanne, CH

## Education

---

- **École polytechnique fédérale de Lausanne** Lausanne, Switzerland  
*PhD in Microsystems and Microelectronics* Aug 2018 - Nov 2022
- **École polytechnique fédérale de Lausanne** Lausanne, Switzerland  
*M.S in Environmental Engineering* Sep 2015 - Feb 2018  
*Specialization: Biological and chemical processes;*
- **Wuhan University** Wuhan, China  
*B.S in Environmental Science* Sep 2011 - June 2015  
*Second degree: Law*

## Experience

---

- **Parithera SA, Agora (CHUV)** Lausanne, Switzerland  
*Research collaborator* Dec 2020 - current
  - **Microfluidics library preparation for single cell analysis:**  
Development of a novel RNA-seq library preparation method that allows transcriptional profiling of low-input (rare) single cells, e.g., circulating tumor cells isolated from patients' liquid biopsy
- **Microsystems Laboratory 4 (LMIS4), EPFL** Lausanne, Switzerland  
*PhD Student (4 years)* Aug 2018 - Nov 2022
  - **Droplet-based microfluidics for biomedical applications:**
    - \* Dissect the underlying physical principle and derive the corresponding analytical and numerical models for a newly discovered fluid phenomenon, which enable novel microfluidics functionalities and accurate controls.
    - \* Invent several deterministic single-cell encapsulation microfluidic platforms for separating, manipulating, and analyzing single cells in droplets, which greatly enhance the single-cell analysis efficiency while solving a long-existing problem in the field of droplet microfluidics.
    - \* Develop an automatic video processing and droplet recognition and analysis pipeline for data extraction, analysis, and visualization.
    - \* Invent a novel and versatile microfluidics sorting method which can sort the single-cell-containing droplets based on the number/size/rigidity of the encapsulated single cells with high sensitivity and accuracy - a low-cost and efficient solution to various microfluidics applications (unpublished).
    - \* Characterize and establish a novel micro-fabrication strategy for the construction of high-precision *multilayer* and/or *3D* microfluidics channels at the microscale.
    - \* Develop an automatic and deterministic droplet electrocoalescence platform for the accurate assembly of two-cell-in-one-droplet biological assays for advanced cell-cell interaction screening aiming for personalized cancer cell therapy.
    - \* (Collaboration) Establish an alginate-based 3D cell model to faithfully recapitulate patient-derived breast cancer; And translate this ex-vivo model into a microfluidics system for enhancing the throughput and reducing tumor consumption during personalized drug/hormone testing.
- **Center of MicroNanoTechnology (CMI), CSEM, LMIS4 etc.** Lausanne/Neuchâtel, Switzerland  
*Teaching assistants* Sep 2018 - Feb 2022
  - **MEMS practicals I: Microactuator technology:** theory and microfabrication, 2020-2022
  - **MEMS practicals II:** Lead teaching assistant for *Ion-Sensitive Field-Effect Transistor (ISFET)*, 2019-2022
  - **Structural Mechanics:** For bachelor students from Microengineering at EPFL, 2018-2020
- **EPFL-ETH summer school** (Virtual)  
*Summer School Committee* July 2021
  - **Summer school 2021: Microsystems for Diagnostics and Health Applications:**
    - \* Organization of a three-day summer school featuring technical workshops, lectures, keynote presentations, career advice, and collaborative projects for 20 doctoral students from ETH, EPFL, and oversea universities.
    - \* Bring together leading experts in the fields of microfluidics and life sciences from both academia and industry.
- **Microsystems Laboratory 4 (LMIS4), EPFL** Lausanne, Switzerland  
*Student supervisors* Feb 2019 - Sep 2022
  - **Student semester projects, master thesis projects, and Lab immersion projects:**  
Supervision of over ten student projects on various topics.
- **Environmental microfluidics Lab (Stockerlab), ETH** Zurich, Switzerland  
*Master thesis* Sep 2017 - Feb 2018
  - **Soil-on-a-chip:** Development of a multimodal 3D microporous microfluidics device to recapitulate the physical and chemical conditions of groundwater for transportation study.
- **Swiss Federal Institute of Aquatic Science and Technology (Eawag)** Dubendorf, Switzerland  
*Internship* Mar 2017 - Sep 2017
  - **Research assistance:** Image analysis and physical modeling of solid disintegration in turbulent flow; Practice of particle image velocimetry (PIV), trajectory vector analysis, and programming with R

## Competencies

---

- **Knowledge:** Microfluidics, Data analysis, Microfabrication, Fluid Science, Microscopy, Microelectronics, Biochemistry
- **Fabrication:** (Two-photon) 3D printing, Photolithography, Laser cutting, Dry etching, Wet etching, Ion beam etching
- **Software:** MS Office, MS Teams, Illustrator, AutoCAD, Solidworks, Klayout, ImageJ, COMSOL, SPSS, Prism
- **Programming:** Python, R, Matlab, C, ImageJ (macro), SQL, LabVIEW, Latex
- **Soft Skills:** Scientific communication, Multi-cultural collaboration, Innovation, Writing, Presentation, Time Management

## Languages

---

- **English:** C1-C2      **French:** A2-B1      **Mandarin (Chinese):** native      **Cantonese (Chinese):** native

## Honors and Awards

---

- **Nomination of EPFL doctoral thesis award (Thesis 2023 Distinctions)** : EPFL, Nov, 2022
- **EPFL Excellence fellowship** (Master): EPFL, 2015-2018
- Award for Outstanding Graduate: WHU, June, 2015
- Excellent Bachelor Thesis: WHU, 2015
- **National Merit Scholarship**: Chinese Ministry of Education, 2014
- Second class in National English Contest for College Students (NECCS): 2014

## Patents and Publications

---

- **Patent:** **Zhou, J.**, Renaud, P. MICROFLUIDIC DEVICE FOR SAMPLE ENCAPSULATION AND METHOD FOR OPERATION THEREOF (EP21208067)
- **Journal:** **Zhou, J.**, Wei, A., Bertsch, A., P. Renaud., High precision, high throughput generation of single-cells containing droplets, *Lab on a chip*, 2022, DOI: 10.1039/D2LC00841F (Cover page featured)
- **Journal:** Penn, R., Maurer, M., Michalec, F. G., Scheidegger, A., **Zhou, J.**, Holzner, M. (2019). Quantifying physical disintegration of faeces in sewers: Stochastic model and flow reactor experiments. *Water research*, 152, 159-170.
- **Journal:** Zhao, J., **Zhou, J.**, Yuan, M., You, Z. (2017). Controllable synthesis of Ru nanocrystallites on graphene substrate as a catalyst for ammonia synthesis. *Catalysis Letters*, 147(6), 1363-1370
- **Under revision:** **Zhou, J.**, Ducimetière, Y.M., Migliozi, D., Keiser, L., Bertsch, A., Gallaire, F., Renaud, P., Break one into three: surface energy driven droplet breakup in microfluidic T junction, "minor revision" at *Physical Review Fluids*. Preprint available at <https://doi.org/10.48550/arXiv.2207.00077>(2022)
- **Under revision:** Salek, M., Jimenez.-M.J., Carrara, F., **Zhou, J.**, Stocker, R. Multiscale Porosity Microfluidics to Study Bacterial Transport in Heterogeneous Chemical Landscapes, under revision
- **Written manuscript:** Zhou, J., Mahtani, N., A., Bertsch, A., P. Renaud., Cell triggered splitting with tunable droplet size for single cell encapsulation, to be submitted (2022)
- **Manuscript in preparation:** **Zhou, J.**, Wei, A., Bertsch, A., P. Renaud., Content-based droplet sorting, manuscript in preparation
- **Conference proceeding and invited speech:** **Zhou, J.**, Bertsch, A., P. Renaud., Passive and Deterministic single cell encapsulation with droplet-based microfluidics, *MicroTas*, Oct 2022, online, selected oral presentation
- **Conference proceeding and invited speech:** **Zhou, J.**, Bertsch, A., P. Renaud., A new mechanism for Cell triggered splitting (CTS) for deterministic single cell encapsulation, *NanoBioTech*, Nov 2022, Montreux, selected oral presentation
- **Conference proceeding:** **Zhou, J.**, Wei, A., Bertsch, A., P. Renaud., Geometry-enabled lateral droplet breakup at T junction, *NanoBioTech*, 2021
- **Conference presentation:** **Zhou, J.**, Wei, A., Piotet, L., Bertsch, A., P. Renaud., Deterministic single cell encapsulation and pairing in droplet microfluidics, EPFL Initiative for Cancer Science and Engineering (EICSE) retreat held by Institut Suisse de Recherche Expérimentale sur le Cancer (ISREC) 2022, poster and selected poster presentation

## Extracurricular activities

---

Badminton (competition)    Road cycling    Swimming    Hiking    Skiing

## Photo

---

